Lancaster University

Optical Characterization of InAsSb Based Quantum Structures for Novel Mid-Infrared Light Emitting Diodes

Abdullah Riyad Altayar

MPhys

Supervisors: Dr Andrew Marshall & Prof Anthony Krier

This thesis is submitted in fulfilment of the requirements for the degree of

Doctor of Philosophy

In physics

Department of Physics

Lancaster University

United Kingdom

January 2023

Declaration

I declare that the contents of this thesis, titled **'Optical Characterization of InAsSb based quantum structures for Novel Mid-Infrared Light Emitting Diodes'**, are the result of my independent work. Where I have consulted the published work of others this is acknowledged by explicit references. This thesis document work carried out between January 2018 and August 2022 at Lancaster University, under the supervision of Prof. Anthony Krier and Dr Andrew Marshall. I confirm that this work has not been submitted in whole or in any part for any other degree or qualification at this university or at any other academic institution.

Abdullah R. Altayar

January 2023

Optical Characterization of InAsSb Based Quantum Structures for Novel Mid-Infrared Light Emitting Diodes

By

Abdullah R. Altayar

January 2023

Abstract

The demand for efficient and cost-effective mid-infrared light-emitting diodes operating in the (3-6 μm) is increasing for various applications such as monitoring the environment and controlling industrial processing. Nevertheless, there is a lack of efficient mid-infrared LEDs operating in this spectral range to facilitate direct low-cost integration into economic systems. In this work possible solutions have been investigated by utilizing different III-V semiconductor materials; compressively strained $Al_xIn_{1-x}As/InAs_{1-y}Sb_y$ (MQWs) and strained-layer superlattices (SLS) of InAs/ $InAs_{1-x}Sb_x$ as active regions incorporated into LEDs structure.

The type-I $Al_{0.12}In_{0.88}As/InAs_{0.915}Sb_{0.085}$ MQWs were grown on GaAs and Si substrates and successfully integrated into the LEDs structure. The structural properties were investigated using high-resolution x-ray diffraction (HRXRD) and atomic force microscopy (AFM); the Si-based MQWs sample exhibited large dislocation density,

less intense satellite peaks, and a rougher surface than the GaAs-based MQWs sample. Simulation of AlInAs/InAsSb band structure revealed a prominent band offset, substantial electron-hole overlap, and e-hh_1 transition energy in agreement with 4 K PL spectra. The I-V characteristics of GaAs and Si-based LEDs show a comparable resistance of ~ 7Ω indicating the possibility of optimisation of these diodes. Bright electroluminescence spectra from both diodes exhibiting emission of ~ 3.4 μm at room temperature. EL emission spectra were interpreted as recombination between the first confined electron and heavy hole states in the InAsSb QW. The EL temperature dependence analysis suggested that thermally activated electron leakage is currently the major factor limiting room temperature emission intensity in these devices. Even though the Si-based LED exhibits a higher defect density, the output power measured at room temperature is significantly higher than that obtained for the GaAs-based LED when the injected current is higher than 1A, due to the improved thermal conductivity of Si substrate. These results suggest that further reduction of the defect density present in the InAsSb/InAlAs MQWs LED integrated onto Si, could enable the development of next-generation light sources, for cost-effective sensing and monitoring systems.

The MBE growth of type-II InAs/ $InAs_{1-x}Sb_x$ SLS on GaAs substrate was systematically studied to overcome some of the problems associated with type-I band alignment, aiming to reduce the Auger recombination rate, enable operation at high temperature and extend the emission wavelength. Theoretical modelling of the band structure revealed the influence of increasing the antimony alloy fraction in the InAsSb and changing the period thickness, on the optical properties of these SLSs. Two series of PL samples exhibit excellent crystalline quality and bright luminescence up to 220 K. The excitation power-dependent PL spectra at 4 K shows; a blue shift trend in the peak

position ~ 7 meV attributed to the bandgap filling effect, and a reduction in the PL intensity by a factor of six as antimony content increased in the InAsSb layers due to reducing wavefunction overlap and increasing non-radiative recombination rate. Temperature-dependence of the PL spectra of the varying antimony and increasing period thickness sample sets show carrier localization behaviour below 80 K associated with the blue shift in the peak position of 10 meV attributed to compositional inhomogeneous or layer thickness fluctuation.

Based on the PL study of InAs/ $InAs_{1-x}Sb_x$ SLS, two prototype diodes containing fifty periods of InAs/ $InAs_{1-x}Sb_x$ SLS active region were grown by MBE on either a conventional lattice matched GaSb substrate or a cost-effective GaAs substrate and fabricated into LEDs. The principle of these diodes is to enable room temperature operation for purpose of ammonia applications. Mid-infrared electroluminescence was obtained from both LEDs over the 4 – 300 K temperature range, exhibiting an emission above 5.6 μm at room temperature. Simulation results indicate the PL peak is due to the e-hh_1 transition at 267 meV, which agrees with the experimental value of 266 meV. A significant thermal quenching of EL spectra is attributed to competition between radiative and non-radiative mechanisms. The GaSb-based LED outperformed the GaAs-based LED showing maximum output power of 175 μW corresponding to an external quantum efficiency of 0.08% at room temperature. Despite this, the integrated intensity of GaAs-based LED was only 1.5 less intense than that on the GaSb substrate.

The type-II InAs/ $InAs_{1-x}Sb_x$ SLS structure shows improvements in the device performance at high temperatures. The integrated EL intensity of SLS LEDs quenches with temperature by a factor of three less than that of MQW LEDs, due to efficiency

in suppression of non-radiative loss. Future work is to design a study that directly compares type-I and type-II systems emitting at the same wavelength using III-V materials such as ternary or quaternary semiconductor alloy. There are a lot of complications with designing these materials such as strain which affect how type-I works and inherent quality material.

Acknowledgement

First, I would like to express my deepest gratitude and thanks to my supervisors Professor Anthony Krier and Dr Andrew Marshall who guided me during my PhD journey. They provided me with invaluable advice, motivate me, and helped me realize my potential during difficult periods of my PhD. Thanks for allowing me to be part of your research group. Thanks for being a kind, wise and encouraging supervisor.

Special thanks go to Dr Peter Carrington for helping me interpretation the EL results and guiding me in each step of writing the first publication. I learned a lot from your valuable knowledge. Your motivation and help contributed tremendously to the successful completion of my PhD work.

Besides, I would like to thank Dr Adam Craig for helping me fabricate my devices and for the good humour and friendship. Thanks for being a kind friend.

Also, I would like to appreciate my colleagues and postdocs with whom I have shared offices, laboratories, and lunchtime – particularly Drs Veronica Letka, Xiao Collins, Laura Hanks, and Eva Repiso.

Also, I would like to thank special people within the physics department for providing technical assistance whenever I need it. These are the safety officer Shaonah Ion, the cryogenics technician Alan Stokes, the cleanroom manager Dr Kunal Lull, Steve Holt and his teams at the mechanical workshops, and the IT supporter Rob Lewsy.

I would like to acknowledge the financial support that I received from Al-Imam University and the Ministry of Higher Education in Saudi Arabia for giving me a once-in-a-lifetime opportunity to undertake PhD in the UK.

Ultimately, I would like to express my appreciation and thanks to my parents who suffer a lot for being thousands of miles away and inspire me to bring my dream to reality, especially during the unavoidable pandemic. A special thanks to my wife for the unlimited support and encouragement throughout all my academic studies. I cannot thank you enough.

List of publications

[1] **Altayar A R**, Al-Saymari F A, Repiso E, Hanks L, Craig A P, Bentley M, Delli E, Carrington P J, Krier A and Marshall A R J 2022 Electroluminescence characterization of mid-infrared InAsSb/AlInAs multi-quantum well light emitting diodes heteroepitaxially integrated on GaAs and silicon wafers *J. Cryst. Growth* **586** 126627

[2] **Altayar A R**, Al-Saymari F A, Letka V, Craig A P, Bentley M, Carrington P J, Krier A and Marshall A R J 2022 Mid-infrared Electroluminescence from Type-II InAs/InAsSb Strained Layer Superlattice Light Emitting Diodes on GaAs and GaSb. In preparation for submission to apply physics letters.

Conferences

[1] **Altayar A R**, Al-Saymari F A, Repiso E, Hanks L, Craig A P, Bentley M, Delli E, Carrington P J, Krier A and Marshall A R J. Electroluminescence characterization of mid-infrared InAsSb/AlInAs multi-quantum well light emitting diodes heteroepitaxially integrated on GaAs and silicon wafers, Mid-Infrared Optoelectronic Materials and Devices (MIOMD) Conference 2021, Talk

Contents

List of Figures

List of Tables

Chapter 1: Introduction

1.1 Motivation

In the past few years, global warming has become a worldwide issue; therefore, mid-infrared light-emitting sources and detectors operating in the 3 – 12 µm spectral region have received a great deal of interest for gas sensing and monitoring applications using the fundamental absorptions fingerprint in this spectral region. This includes monitoring greenhouse gases such as methane CH_4 (3.3 µm), carbon dioxide CO_2 (4.25 µm), nitrous oxide N_2O (4.5 µm), carbon monoxide CO (4.7 µm), nitric oxide NO (5.3 µm), and ammonia NH_3 (5.7 µm) as indicated in figure 1.1.

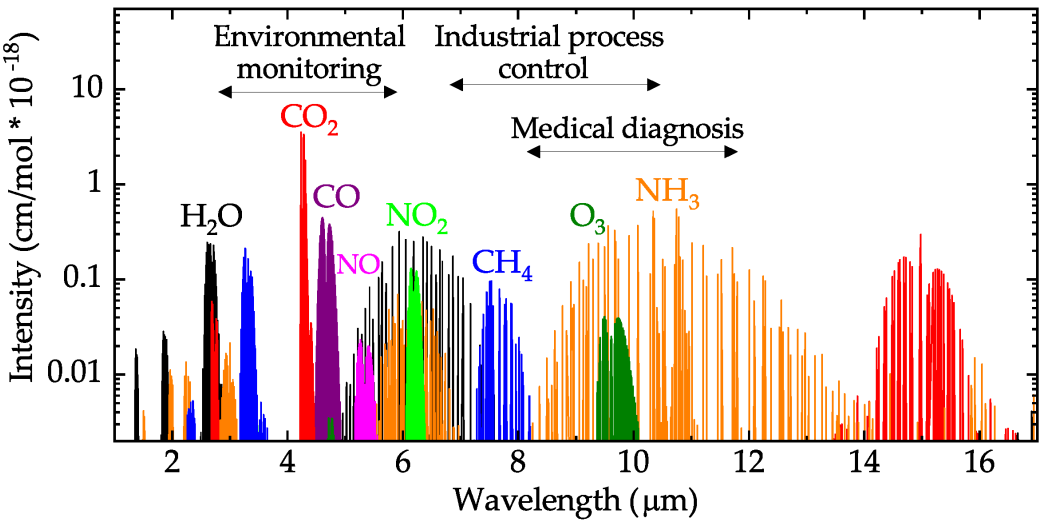

Figure 1.1: Mid-infrared atmospheric absorption spectra of selected molecules with their relative intensity. Figure adapted from reference[1] based on HITRAN database[2].

Photonic components operating in the mid-infrared (MIR) spectral region from 2 to 6 µm are of increasing technological interest due to the potential applications at these wavelengths. In many applications, MIR-LEDs are a far more attractive and cost-

effective alternative to lasers, especially for widespread distributed sensing applications which require many point sensors, portable instruments and low power consumption. Notably, much effort has been focused towards the development of LED devices operating at several particular MIR wavelength regions depending on the specific detection applications [3,4]. This is due to the fact that several atmospheric gases, such as CH_4, NO, NH_3, and biomolecules have their fundamental absorption bands in this spectral range. Various light emitting source structures have been developed including bulk InAs[5], binary InAs/GaSb SLS[6], ternary GaInAs/GaAsSb MQWs[7], and quaternary GaInAsSb/GaSb WQW[8] active regions, and some of these have been successfully commercialized[9,10].

Methane gas contributes significantly to global warming and the destruction of the Earth's ecosystem. Statics shows that Methane contributes to at least 25% of today's gross warming[11]. CH_4 gas originates from several sources, including landfills, oil and natural gas systems, automobile combustion, and specific industrial processes[12]. Therefore, it is important that methane concentration can be effectively monitored and this has been attempted using various material systems, which all have their own compromises. Initial attempts used LPE grown bulk LED devices[3,5], while more recently Liang et al achieved the required emission wavelength by utilizing the quaternary alloy GaInAsSb with an antimony composition > 50 % in a laser structure [13]. However, the miscibility gap in InGaAsSb is a concern at the compositions required and a major limitation of their device was the loss of hole confinement. Although some success in commercialization there is still good scope for exploring new and improved material systems or emitter structures.

Nitrous oxide is produced from coal burning power plants and chemical fertilizers in soil[14]. The impact of ammonia emission on the atmosphere has been well documented for its acidification and eutrophication effects on ecosystems[15]. The main source of NH_3 emission is agriculture-related processes such as manure and fertilizer applications[16]. They are estimated to contribute around 85% of the total NH_3 emission in the UK[17]. To date, a wide range of homoepitaxial Sb-based III-V semiconductor devices have been developed [18–21] based on several quantum systems such as GaInAsSb/AlGaAsSb quantum wells (QWs) [21], InSb/InAs quantum dots (QDs) [22] and type-II InAs/GaSb superlattices (SLs) [23] demonstrating promising performance. More recently, significant progress has been made in developing Interband cascade LEDs (ICLEDs) exhibiting strong output power up to 1.4 mW and 0.5 mW at 4.2 and 4.7 μm, respectively [24,25].

Development of mid-infrared III-V semiconductors LEDs on more mature substrates such as GaAs and silicon (Si) is increasingly being demonstrated, benefiting from the mature manufacturing technology, the availability of large size wafers and lower fabrication costs. Most importantly, direct growth on Si also provides the possibility of developing a complete MIR Si photonics platform for future integrated sensor circuits[26]. In this avenue of work, our research group at Lancaster recently reported on the optical properties of $InAs_{1-x}Sb_x/Al_yIn_{1-y}As$ QWs grown on GaAs via a relaxed AlInAs metamorphic buffer layer [27].

Several reports have investigated the optical properties of InAs/InAsSb Single Quantum Well (SQW) or MQWs active regions grown on GaSb substrates[4,20,28,29]. This includes the study of InAs/InAsSb superlattice (SLS) active regions [20,30–33], where the composition of Sb was > 20% which corresponds to wavelengths λ >5.6 μm as required for the development of MIR photodetectors[34,35]. Several authors used these

superlattice structures into an active region for emitters such as lasers[36–38]. But there have been fewer reports of MIR LEDs using InAs/InAsSb strained layer superlattice structure on lattice-mismatched GaAs substrate for wavelength beyond 5 μm[39].

Despite the advantages of MIR-LEDs, these devices' efficiency is strongly reduced by several factors, including significant temperature dependence (reduction in emission intensity as temperature increases) due to the increased rate of non-radiative Auger recombination. Auger recombination rates increase significantly when carrier concentration increases, either through increases in intrinsic carrier concentration or due to current injection, especially at longer wavelength[40,41]. Given the limitations associated with these MIR-LEDs, the importance of developing LEDs structures that can overcome these challenges has become evident.

The goal of this thesis is to lay the foundations for developing next-generation, cost-effective light-emitting diodes using III-V semiconductor quantum structures.

1.2 Thesis outline

The first chapter explains the motivation of this work and summarises its focus. The second chapter discusses the fundamentals and theoretical background of semiconductor LEDs in more detail. In the third chapter, a comprehensive literature review on mid-infrared LEDs, Interband cascade ICLEDs, and resonance cavity RCLEDs is presented, followed by an outline of the experimental work carried out in this thesis, in chapter four. The results chapters detail the design, growth, fabrication, and optical and electrical characterisation of AlInAs/InAsSb MQW and InAs/InAsSb SLS PL structures and LEDs; in chapters five and six respectively. Finally, a summary of the results and suggestions for future work are combined in chapter seven

Chapter 2: Background Theory

This chapter presents the theory and fundamental concepts of III-V semiconductor material-based light-emitting diodes (LEDs). The concept of a material band structure, including the temperature dependence of the bandgap, the band alignment, and the strain, is highlighted. Then, quantum confinement and its effect on energy levels is described, followed by an explanation of the recombination mechanisms by radiative and non-radiative processes. The principle of experimental techniques used to analyse samples and devices, including photoluminescence and electroluminescence, are explored. Additionally, the concept of a light-emitting diode and the methodology for evaluating its performance is reviewed.

2.1 Band Structure of Semiconductor(Band Theory)

According to band theory, when atoms and molecules combine to form a solid material, their discrete energy levels condense to form energy bands. The outer band known as the conduction band is the highest filled energy, while the next highest band (empty or party filled) name the valence band. The energy difference between these bands is the bandgap. Based on the band structure, the classification of materials can be conductor, semiconductor, or Insulator. In insulator materials, the bandgap is large, so electrons cannot move to the conduction band. In conductor materials, the conduction band and valence band are overlapped, and thus any electron in the valence band is spontaneously in the conduction band. In semiconductor materials, there is a small gap in which

electrons can be promoted via excitation sources (such as optical or electrical sources) to the conduction band which is subject to an increased temperature above 0 K. This transition dictates the optical and electrical properties of semiconductors. A schematic of energy band structures for different types of materials is shown in Figure 2.1

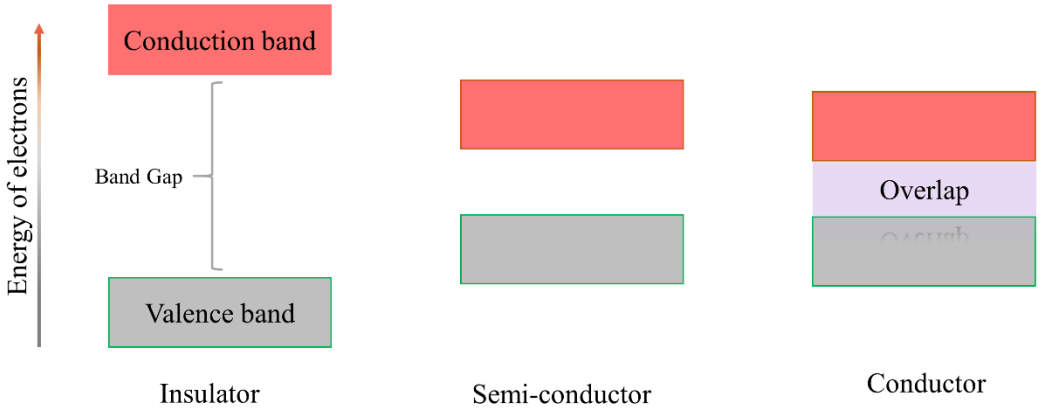

Figure 2.1: Schematic diagram of the band structure of insulator, semiconductor, and a conductor and their respective bandgaps.

2.1.1 Temperature dependence of band structure

When the temperature increases, the lattice spacing of semiconductor materials expands, reducing the binding energy of electrons. As a result, the energy required to excite the electron from the valence band to the condition band decreased, and the bandgap was reduced. This behaviour can be described using the empirical Varshni equation[42]:

$$E_g(T) = E_g(0) - \alpha T^2/\beta + T \qquad (2.1)$$

Where $E_g(0)$ is the energy gap at zero kelvin, and the coefficients α and β are fitting parameters related to the thermal expansion of lattice and Debye temperature correspondingly.

2.1.2 Band structure alignments

The heterointerface is formed by joining two different semiconductor materials with different electron affinities (χ) and or bandgaps, causing a discontinuity in the valence and/or conduction bands. The electron affinity (χ) is defined as the separation between the conduction band and the vacuum level. Offsets in the valence band ΔE_{VB} and conduction band ΔE_{CB} lead to three types of band alignment (type-I, type-II, and type-III) which can be calculated according to the following[43]:

$$\Delta E_{VB} = (\chi_1 + E_{g1}) - (\chi_2 + E_{g2}) \quad (2.2)$$

$$\Delta E_{CB} = (\chi_2 - \chi_1) \quad (2.3)$$

Where Eg is the energy bandgap of semiconductor material.

2.1.2.1 Type-I band alignment

Type-I band alignment occurs when material B valence and conduction band edges fall within the bandgap of material A, as illustrated in figure 2.2. Consequently, the electrons and holes are confined in material A conduction and valence band, and their recombination occurs via direct transition. Nanostructures based on type-I are favoured in optical emitting devices such as lasers and LEDs due to the large overlap integral of

electrons and holes. An example of this structure is InAsSb/AlInAs interface which is discussed in this work.

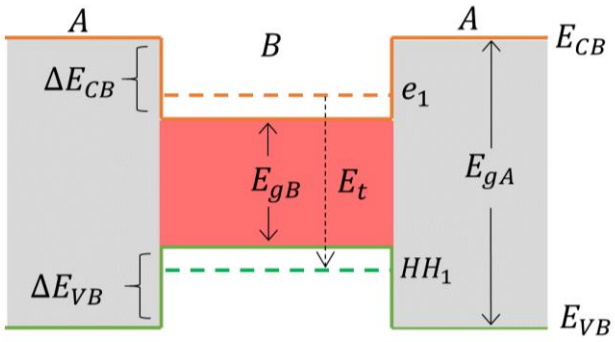

Figure 2.2: Schematic diagram of type-I band alignment and corresponding electron and heavy hole energy level.

2.1.2.2 Type-II band

Type-II band alignment occurs when both bands offset the conduction band ΔE_{CB} and valence band ΔE_{CV} positive (type-IIa) or negative (type-IIb), as shown in figure 2.3. If the electrons are located within the small bandgap material (A) and the holes in the larger bandgap material (B), a type-IIa band structure is formed (e.g. InAs/AlSb). In contrast, if electrons are located within the large bandgap material (B) and the holes in the small bandgap material (A), type-IIb band structure occur. Therefore, recombination occurs via indirect transition due to spatial separation for the carriers, but the transition is still direct in k-space. Such structures are often utilised in devices where longer carrier lifetimes and reduction of non-radiative centres are needed. An example of type-IIb structure is InAs/InAsSb interface presented in this work.

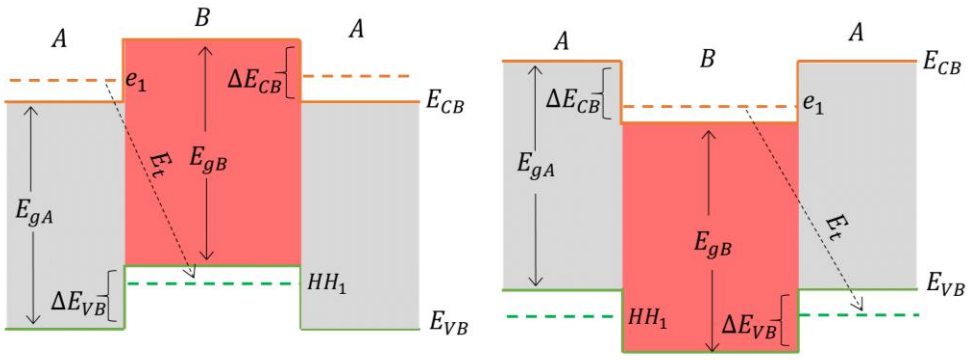

Figure 2.3: Schematic diagram of type-II band alignment, corresponding electron and heavy hole energy level, and transition energy.

2.1.2.3 Type-III band

Type-III band alignment or broken type-II occur if the conduction band of the second semiconductor material overlaps with the valence band of the first semiconductor (e.g. InSb/InAs) as indicated in figure 2.4.

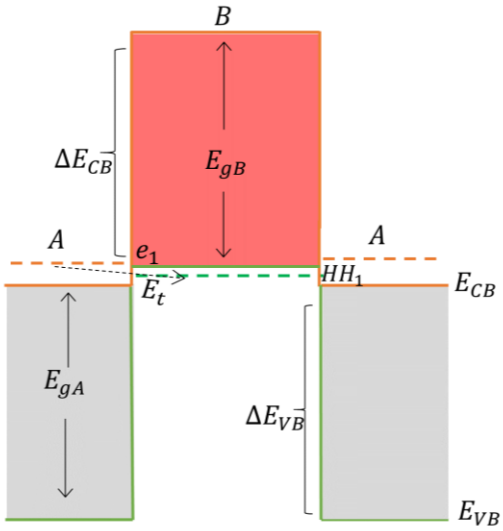

Figure 2.4: Schematic diagram of type-III band alignment (broken gap) structure.

2.1.3 Bandgap engineering with semiconductor alloys

Most of the III and V compounds featuring zinc blend crystal structures. The room-temperature bandgap energy of binary III-V semiconductors is illustrated in figure 2.5[44]. Alloys are combinations of multiple elements in a solid solution. Semiconductor alloy materials consist of binary III-V materials where adjusting the bandgap is possible by controlling the alloy ratio. According to Vegard's law, the composition-dependent bandgap energy E_g of the ternary alloy can be determined as[45]:

$$E_g(A_{1-x}B_x) = (1-x)E_g(A) + xE_g(B) - x(1-x)C_{bowing} \qquad (2.4)$$

Where $E_g(A)$ and $E_g(B)$ are the bandgap energies of the binary materials, x is the composition of the element, and C_{bowing} is the bowing parameter.

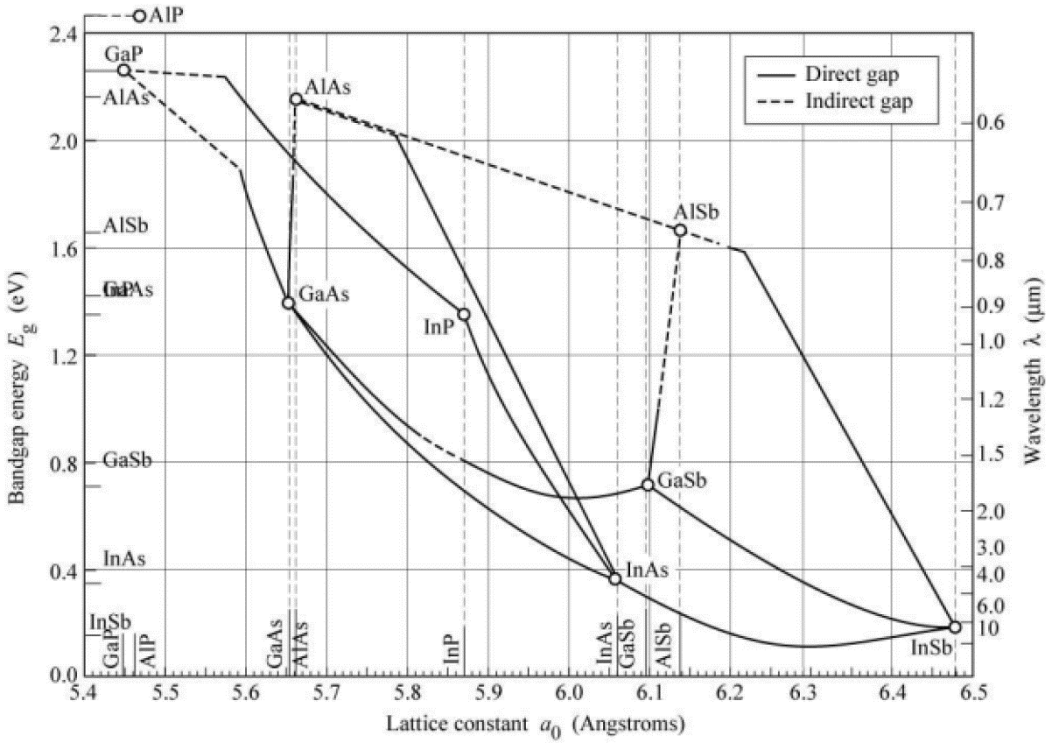

Figure 2.5: Band gap energy of III-V semiconductor materials as a function of lattice constant indicating the possible wavelengths of emission from the various materials at zero temperature[44].

It can be seen from figure 2.6, different bandgap alignments occur with various semiconductor materials. For example, type-I band alignment form when AlSb and GaSb are joined together. Similarly, type-III band alignment is formed between GaSb and InAs.

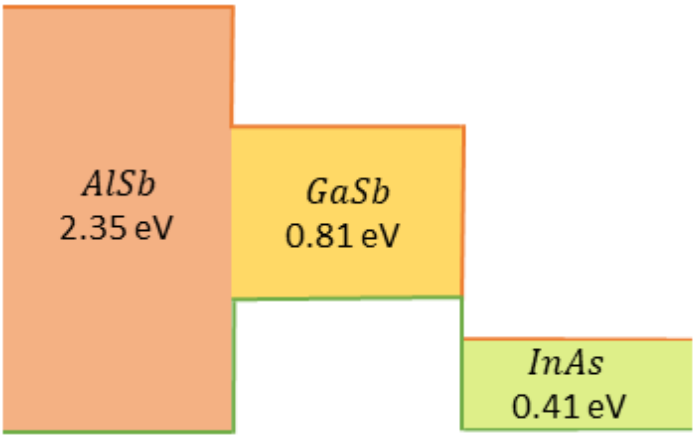

Figure 2.6: Band diagram of AlSb/GaSb/InAs showing possible band alignment.

2.1.4 Strained layers

When growing a layer with a lattice constant of a_L on top of the substrate with different lattice constant a_{sub}, this generates stress in the structure leading to deformation of the crystal. As a result, the new layer a_L will reshape to bond to the bottom material and eventually, dislocations are formed. Strain can be compressive or tensile strains as shown in figure 2.7. The compressive strain occurs if the lattice constant of the top layer is greater than the substrate ($a_L > a_{sub}$), then the layer compresses perpendicular to the growth direction and increases in the direction of growth. If ($a_L < a_{sub}$), the tensile strain is resulting in the converse occurrence.

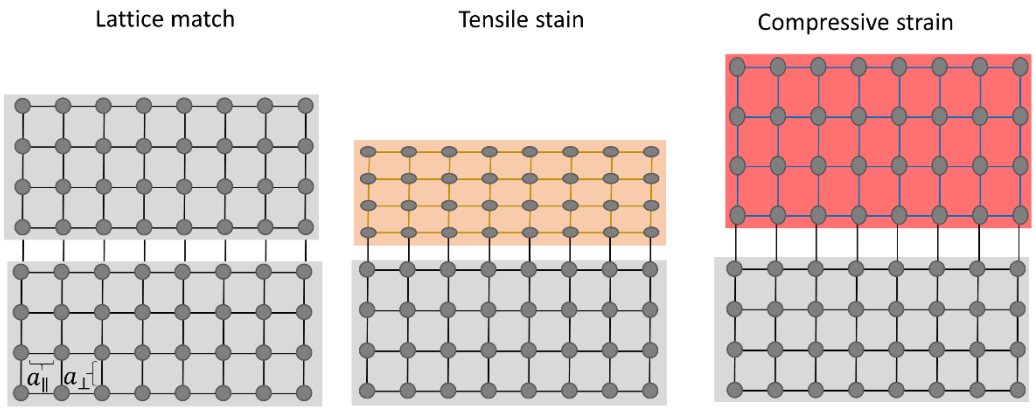

Figure 2.7: Schematic diagram showing the effect of lattice match, tensile and compressive strain on the epilayer constant due to growth on a substrate.

2.1.5 Strain effects on the band structure

The effect of the strain on the energy levels of the epilayer depends on the type of strain involved. A comparison of strained (compressive or tensile) and unstrained energy levels are shown in figure 2.8[46]. Under compressive strain, the conduction band (CB) shifts down while the valence band heavy hole (HH) shifts up, and the light hole (LH) moves down. The tensile strain has the opposite effect on the conduction and valance bands.

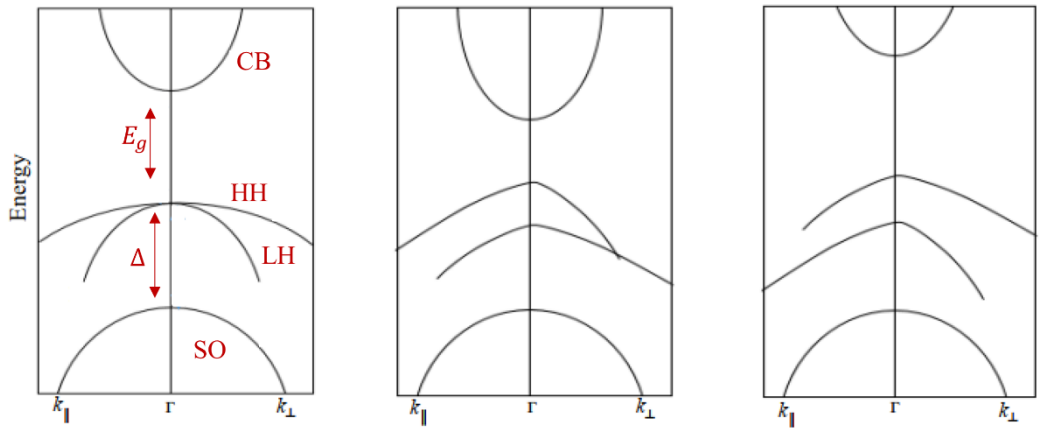

Figure 2.8: The effect of strain on the energy levels of semiconductor for (a) unstrained, (b) compressive, and (c) tensile strain[46].

Van der Waller[47] and Krijn [45] proposed strain dependence of the valence and conduction band edge in the III-V semiconductor materials. The Pseudomorophic (lattice mismatch) growth of strained layers on a substrate is subject to a biaxial strain $\varepsilon_{\parallel}$ parallel to the plane of the interface/growth surface ($a_{\parallel} = a_{Lx} = a_{Ly} = a_{sub}$) and a uniaxial strain $\varepsilon_{\perp}$ perpendicular to growth surface ($a_{\perp} = a_{LZ}$). The values of $\varepsilon_{\parallel}$ and $\varepsilon_{\perp}$ are related to lattice mismatch $\Delta a_{\parallel}$, and $\Delta a_{\perp}$ which expressed as [45,48]

$$\varepsilon_{\parallel} = \frac{\Delta a_{\parallel}}{a_l} = \frac{(a_{\parallel} - a_1)}{a_l} = -\frac{(a_1 - a_{sub})}{a_l} \qquad (2.5)$$

$$\varepsilon_{\perp} = \frac{\Delta a_{\perp}}{a_l} = \frac{(a_{\perp} - a_l)}{a_l} \quad \text{and} \quad a_{\perp} = a_l(1 - D)\varepsilon_{\parallel} \qquad (2.6)$$

The constant a_l represent the lattice constant of the layer material, D depends on the elastic constants of the layer material and the interface ordination:

$$D^{001} = 2\frac{c_{12}}{c_{11}} \qquad (2.7)$$

$$D^{111} = 2\frac{c_{12}+2c_{12}-2c_{44}}{c_{11}+2c_{12}+4c_{44}} \qquad (2.8)$$

There are two aspects to strain's effect on energy levels: hydrostatic and shear components. Considering the conduction (E_C) and valence band (E_V) at Γ-point, the hydrostatic strain component shift the average valence band energy :

$$E_{v,av} = \frac{(E_{hh}+E_{lh}+E_{so})}{3} \qquad (2.9)$$

Where E_{so} is the spin-orbit splitting off energy. The shift in the conduction ΔE_c^{hydro} and valence band $\Delta E_{v,av}^{hydro}$ are given by :

$$\Delta E_c^{hydro} = a_c(2\varepsilon_{\parallel} + \varepsilon_{\perp}) \qquad (2.10)$$

$$\Delta E_{v,av}^{hydro} = a_v(2\varepsilon_{\parallel} + \varepsilon_{\perp}) \qquad (2.11)$$

Where a_c and a_v are the conduction and valence band hydrostatic deformation potential, respectively. The shear component splits the valence band energies as :

$$\Delta E_{hh}^{sheer} = -\frac{1}{2}\delta E^{sheer} \quad (2.12)$$

$$\Delta E_{lh}^{sheer} = -\frac{1}{2}\Delta_o + \frac{1}{4}\delta E^{sheer} + \frac{1}{2}\left[{\Delta_o}^2 + \Delta_o \delta E^{sheer} + \frac{9}{4}(\delta E^{sheer})^2\right]^{\frac{1}{2}} \quad (2.13)$$

$$\Delta E_{lh}^{sheer} = -\frac{1}{2}\Delta_o + \frac{1}{4}\delta E^{sheer} - \frac{1}{2}\left[{\Delta_o}^2 + \Delta_o \delta E^{sheer} + \frac{9}{4}(\delta E^{sheer})^2\right]^{\frac{1}{2}} \quad (2.14)$$

Where Δ_o is the spin-orbit splitting off energy (without strain), δE^{sheer} is the strain-dependent shift on the interface orientation. For growth on 001 and 111 planes, the δE^{sheer} is given by :

$$\delta E_{001}^{sheer} = 2b(\varepsilon_\perp - \varepsilon_\parallel) \;\&\; \delta E_{111}^{sheer} = \frac{2}{3}\sqrt{3}d(\varepsilon_\perp - \varepsilon_\parallel) \quad (2.15)$$

Where b and d are the tetragonal and rhomboidal shear deformation potential correspondingly. The conduction band at Γ-point are not affected by the shear contribution to the strain. The total shifts in the valence band edge are given by:

$$\Delta E_{v,total}^{sheer}(hh, lh, so) = \Delta E_v^{hydro} + \Delta E_{hh,lh,so}^{sheer} \quad (2.16)$$

Consequently, the energy shift of the SO band induced by the strain can be used to suppress the CHSH Auger process by increasing the activation energy and reducing the rate, as well as reducing inter-valence band absorption[45,49].

2.1.6 Dislocations

When a layer of material with a lattice constant is different from the native lattice constant of the substrate, some of the strains are relieved through a dislocation event.

Defects in crystalline materials may also occur if the thickness is greater than the critical thickness. Such defects modify the periodic order of the crystal structure, which also modifies many of the physical properties of materials by decreasing carrier mobility due to increased scattering and acting as non-radiative centres by forming unwanted energy levels[50,51]. If a row of lattice points is affected, then line defects or dislocation are generated and can be classified as an edge ($\overrightarrow{b_{\perp}}$), screw ($\overrightarrow{b_{\parallel}}$), or mixed dislocations. A plane of atoms is inserted into the crystalline lattice perpendicular to the Burger vector in the edge dislocation. In this manner, the strain is relieved in the system and does not go upward in the sample. In the screw dislocation, the inserted plane of atoms is parallel to the Burger vector (along the growth direction), as indicated in figure 2.9[52]. This type of dislocation is problematic because it formed through the measurement space of the sample[53]. A mix dislocation is the combination of edge and screw dislocations where the dislocation line occurs at an arbitrary angle concerning the Burgers vector. This type of dislocation it's favoured in heterostructures growth.

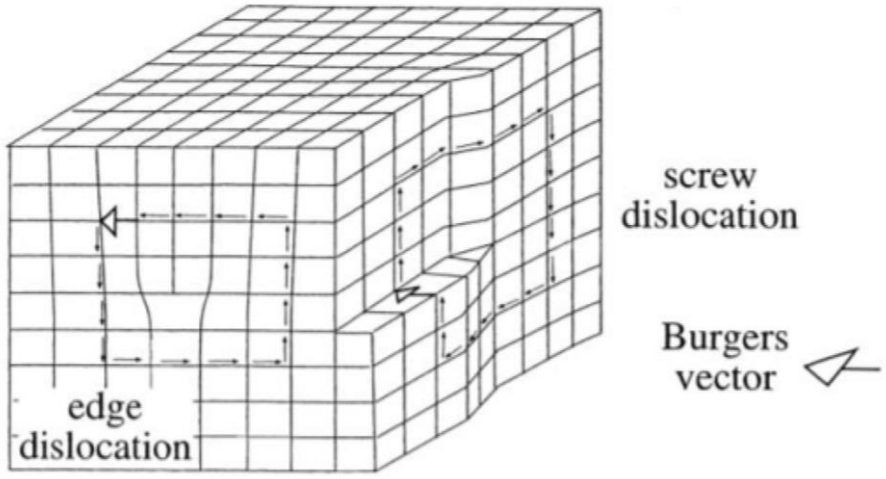

Figure 2.9: Illustration of the possible type of dislocation that can occur in crystal structure due to a large lattice mismatch at the interface between two materials.[52]

2.1.7 Critical thickness

Critical thickness (h_c) is determined by the lattice mismatch between the epitaxial layer and the substrate. Increasing the thickness of the epilayer above the critical thickness leads to increased strain energy density, which generates dislocations. An early attempt to calculate the critical thickness was first reported by Frank and Van der Merwe in 1989[47] which was then developed by Matthews and Blakeslee[54] by considering the mechanical balance between the stress due to strain and tension in dislocation, and the expression is given by:

$$h_c = \left(\frac{b}{4\pi f(1+v)}\right)\left[ln\left(\frac{h_c}{b}\right) + 1\right] \qquad (2.17)$$

$$f = \frac{a_{\text{sub}} - a_{\text{layer}}}{a_{\text{layer}}} \qquad (2.18)$$

$$v = \frac{c_{12}}{c_{11} - c_{12}} \qquad (2.19)$$

Where b is the Burgess Vector, f is the lattice mismatch, v is Poisson's ratio where c_{11} and c_{12} are elastic constant of the epitaxial layer. Another approach to determine the critical thickness (h_c) was suggested by People and Bean[55] :

$$h_c = \left(\frac{1-v}{1+v}\right)\left(\frac{b^2}{16\pi\sqrt{2a(x)}f^2}\right)\left[ln\left(\frac{h_c}{b}\right)\right] \qquad (2.20)$$

In this model, dislocations were not produced at the interface but within the epitaxial layer (screw dislocation). This consideration is due to low formation energy compared to other dislocations.

2.2 Quantum Structures

Whenever different materials are brought together, the carriers become confined within a narrow, low-bandgap region. Furthermore, if the region is comparable in size to the

de Broglie wavelength of an electron, these carriers can have quantised energies. The confinements dimensions are formed by combining semiconductors with different bandgap so that charge carriers are confined in 0-D (quantum dots), 1-D(quantum well), 2-D (quantum wires) or 3-D (bulk), causing differing density of states and, thus quantum mechanical properties (electron-hole interaction, light interaction (photons), and lattice vibration (phonon).

2.2.1 Quantum Confinements

In quantum well structure, the electrons and holes are confined within a well along the growth direction (z-axis). The possible energy levels and wavefunctions of these carries are determined by solving the Schrödinger equation, which states that :

$$E\psi = -\frac{\hbar}{2m}\frac{d^2\psi}{dz^2} + U_0(z)\psi \qquad (2.21a)$$

Where E is the energy, ψ is the wavefunction of a given energy state in the z-direction, $\hbar$ is the plank constant, U_0 is the potential barrier. Due to the finite nature of the potential in quantum well, it is necessary to consider the wavefunction in both the well and barrier.

$$\frac{\hbar}{2m}\frac{d^2\psi}{dz^2} + {K_w}^2\psi(z) \quad for\ |z| < \frac{w}{2}, \quad K_w = \sqrt{\frac{2mE}{\hbar^2}} \qquad (2.21b)$$

$$\frac{\hbar}{2m}\frac{d^2\psi}{dz^2} + {K_b}^2\psi(z) \quad for\ |z| < \frac{w}{2}, \quad K_b = \sqrt{\frac{2m(U_0-E)}{\hbar^2}} \qquad (2.22)$$

Where K_w and K_b are the wavefunction of the well and barrier, respectively. Because a wave function and its derivative must be continuous at the barrier and well boundaries, it follows that:

$$\left(K_w\frac{L}{2}\right)^2 + \frac{m_W}{m_b}\left(K_b\frac{L}{2}\right)^2 = \frac{2m_wV_0}{\hbar}\left(\frac{L}{2}\right)^2 \qquad (2.23)$$

Thus,

$$K_b\sqrt{\frac{m_b}{m_w}}\,\frac{L}{2} = \frac{m_b K_w}{m_w}\tan\left(K_w\,\frac{L}{2}\right) \quad \text{for even solution (cos}(\psi)\text{ wavefunction)} \quad (2.24)$$

$$K_b\sqrt{\frac{m_b}{m_w}}\,\frac{L}{2} = -\frac{m_b K_w}{m_w}\cot\left(K_w\,\frac{L}{2}\right) \quad \text{for odd solution (sin}(\psi)\text{ wavefunction)} \quad (2.25)$$

Where m_W and m_b are the particle masses for the well and barrier, respectively. Equation (2.23) and either equation (2.24) or (2.25) provide insight into the n level of energy within the well :

$$E_n = \frac{\hbar^2}{2m}\left(\frac{\pi}{L}\right)^2 n^2 \quad (2.26)$$

Based on the bandgap of the potential well (quantum well) material and the quantisation energies of the ground levels, the lowest level is defined by its energy :

$$E_1 = E_g^{QW} + E_{e1} + E_{hh1} \quad (2.27)$$

2.2.2 The density of States (DOS)

Since electrons are subject to Pauli's exclusion principle, they cannot all occupy the lowest energy state at the band edge; instead, they are distributed in different states. The density of state $\rho(E)$ is defined as the number of possible quantum states per unit volume per unit energy :

$$N(E) = \rho(E)dE \quad (2.28)$$

Where N(E) is the carrier density, $\rho(E)$ is the density of state. The free m otion of carriers in semiconductor materials is confined to zero dimension (quantum dot), one dimension (quantum wires), two dimensions (quantum well), or three dimensions

(bulk) as shown in table 2.1 are summarised and the details derivative can be found in many textbooks [43]

Table 2.1: The evolution of the density of state DOS

Dimension	$\rho(E)$
0D quantum dots	$2\delta(\mathrm{E}-\mathrm{E_{MIN}})$
1D quantum well	$\sqrt{2\pi \mathrm{m}^*/\hbar^2}\ \ 1/\sqrt{(\mathrm{E}-\mathrm{E_{MIN}})}$
2D quantum wires	$\mathrm{m}^*/\pi\hbar^2 \ \sum_{\mathrm{i}} \mathrm{H}(\mathrm{E}-\mathrm{E_i})$
3D bulk	$\frac{1}{2\pi^2}\ \frac{\left(2\mathrm{m}^*/\hbar^2\right)^3}{2}\ \frac{(\mathrm{E}-\mathrm{E_g})^1}{3}$

Where m^* is the effective mass of the electron, $\hbar^2$ is the reduced Planck constant, H(x) is a Heaviside step function, and E is the energy. A schematic diagram of various quantum confinement and the corresponding density of states with allowed energy levels are shown in figure 2.10[56]. In a bulk semiconductor, $\rho(E)$ is zero at the bottom of the conduction band and increase with energy hence ($\mathrm{E}^{1/2}$) while in quantum well, $\rho(E)$ is a step function due to discrete energy levels along the confinement direction (z-axis). In quantum wires, $\rho(E)$ proportion inversely with energy ~ $1/\mathrm{E}^{1/2}$. In a quantum dot, $\rho(E)$ has only discrete value, and hence DOS is a series of the delta function.

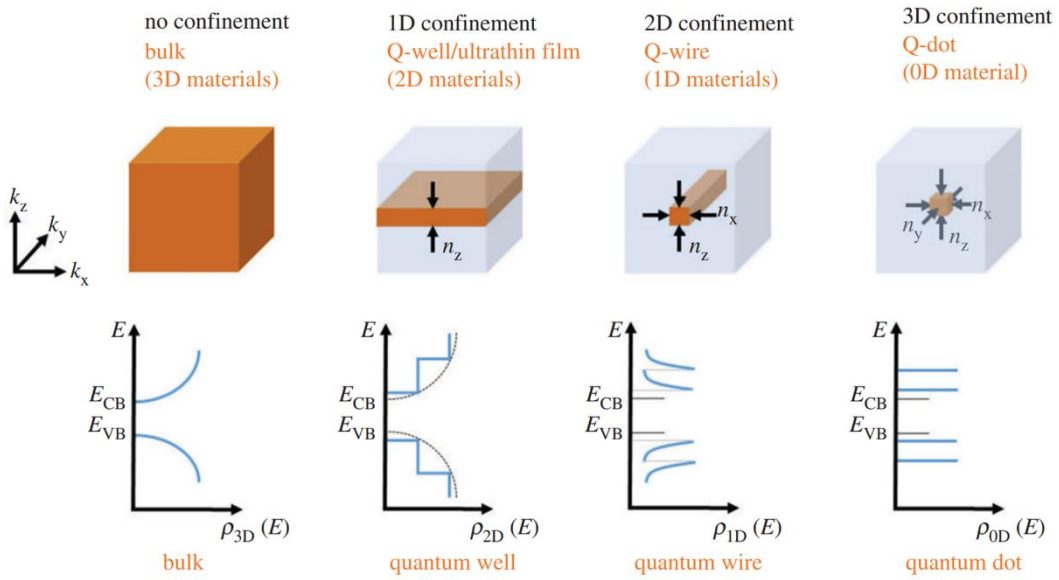

Figure 2.10: Density of states (DOS) for semiconductors showing various confinement structures[56].

2.2.3 Electron and hole wavefunction overlap

The electron wavefunction (Ψ_e) and hole wavefunction (Ψ_h) overlap can be estimated according to:

$$overlap_{e-h} = \frac{|\sigma|^2}{N_{e1}N_{hh1}} \qquad (2.29)$$

Where N_{e1} and N_{hh1} are described by :

$$N_{e1} = \Delta z \sum_n \left(|\Psi_{e1,n}|\right)^2 \qquad (2.30) \qquad N_{hh1} = \Delta z \sum_n \left(|\Psi_{hh1,n}|\right)^2 \qquad (2.31)$$

Where Ψ_{e1} *and* Ψ_{hh1} is the wavefunction amplitude at each point along the growth direction Z.

2.3 Recombination processes

Electron-hole recombination is a fundamental process involved in the operation of many optoelectronic semiconductor devices, i.e., LEDs and laser diodes. Under the non-equilibrium condition, the recombination process is either accompanied by photon emission (radiative recombination) or phonon (non-radiative recombination), as illustrated in figure 2.11. In the following sections, several processes of radiative and non-radiative mechanisms that can occur in semiconductors are discussed.

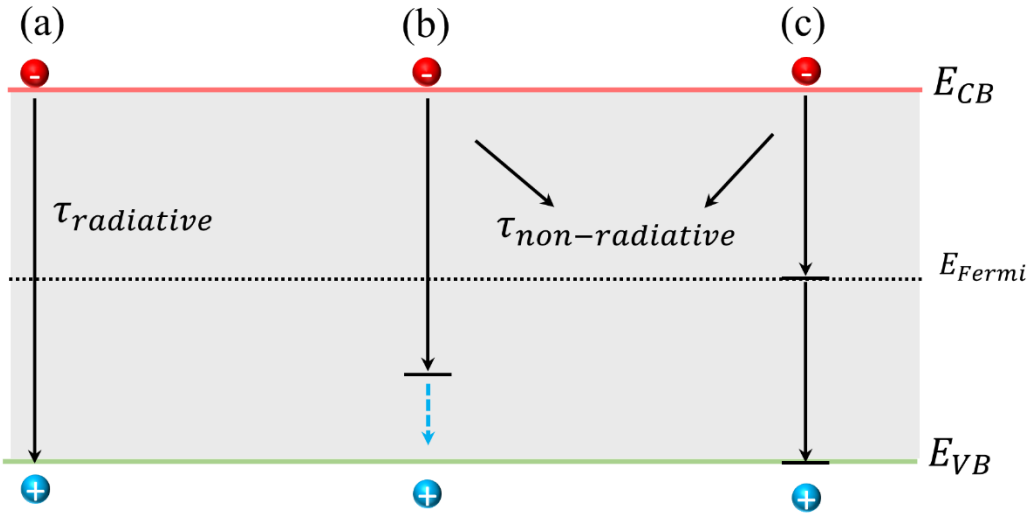

Figure 2.11: Schematic of the recombination process (a) radiative recombination through the band to band and non-radiative through (b) deep level and (c) mid-gap level recombination.

2.3.1 Radiative recombination process

Under equilibrium conditions where there is no external stimulation (optical or electrical) at a given temperature, the intrinsic carrier concentration n_i is the product of the electron (n_o) and hole (p_o) concentrations [57]:

$$n_i^2 = n_o p_o \qquad (2.32)$$

Using external stimulation, the excess carriers can be generated and thus, the total excess carrier concertation is given by:

$$p = p_o + \Delta p \qquad \text{and} \quad n = n_o + \Delta n \qquad (2.33)$$

Where Δp and Δn are the excess hole and electron concentration, respectively. Several different radiative mechanisms may occur, such as band to band, donor to valence/conduction to acceptor, donor to acceptor, and exciton recombination (see figure 2.12).

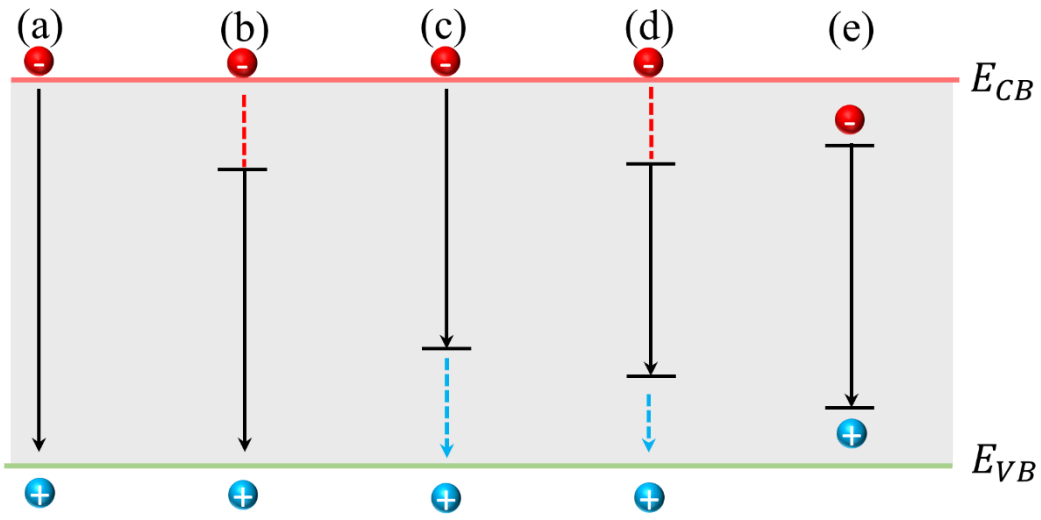

Figure 2.12: Schematic of the different radiative recombination processes (a) band-to-band, (b) donor to valence band, (c) conduction band to acceptor, (d) donor to the acceptor and (e) excitonic. Red circles represent the electrons and blue represent the holes while the solid line represents photon emission and the dashed line represents phonon emission.

In the band-to-band process, an electron from the conduction band recombines with a hole in the valance band where the energy of the emitted photons (hv) is related to the bandgap energy (E_g) :

$$hv = E_G(T) + \frac{k_b T}{2} \qquad (2.34)$$

The recombination rate is related to electron and hole concentrations as $R \propto np$. The recombination rate per unit time can be expressed as :

$$R = -\frac{dn}{dt} = -\frac{dp}{dt} = Bnp \qquad (2.35)$$

Where B is the bimolecular recombination coefficient with a typical value of 10^{-9}- 10^{-11} cm^3/s for direct bandgap III-V semiconductors[57].

In the donor to valence/conduction to acceptor processes, an electron from the donor level recombines with a hole in the valence band. In contrast, conduction to acceptor occurs if the electron recombines with holes in the acceptor level. Let E_i be the donor or acceptor binding energy; then the photon energy is expressed as :

$$hv = E_g(T) - E_i + \frac{k_b T}{2} \qquad (2.36)$$

At low temperatures, this process is most likely to occur.

In the donor to acceptor process, an electron from the donor level joins the hole in the acceptor level. If E_{donor} is the donor binding energy and $E_{acceptor}$ is the acceptor binding energy, then the energy of the emitted photon is defined by :

$$hv = E_G(T) - \left(E_{donor} + E_{acceptor}\right) + \frac{e^2}{4\pi\varepsilon_o\varepsilon_r r} \qquad (2.37)$$

where e is the charge of the electron, ε_o is the static dielectric constants of the free space, $\varepsilon_r$is the relative permeability of the semiconductor material, and r is the separation between the acceptor and donor. The donor-acceptor recombination process can occur if the density of both acceptors and donors is sufficiently high, and it is most likely to take place at a low temperature[58].

In the exciton recombination process, the emitted photon energy is due to Coulomb interaction and can be expressed as:

$$hv = E_G(T) - E_{ex} \quad (2.38)$$

Where E_{ex} is the free binding energy of electron-hole interaction, typically in the range of a few meV in narrow bandgap materials.

2.3.2 Non-radiative recombination process

In a non-radiative recombination event, the electron-hole pairing does not produce a photon; instead, the released energy is converted to the vibration of lattice atoms, i.e. phonons released. Such recombination can be generated due to defects in crystal structure where unwanted energy levels form, i.e. dislocations and impurity. The energy levels are generated within the forbidden gap of the semiconductor (deep levels), which are also referred to as recombination centres or luminescence killers. Therefore, improving the rate of radiative recombination and reducing non-radiative recombination is important in light-emitting devices, where the former is considered a limiting factor in the performance of optoelectronic devices. The two most common non-radiative recombination are Shockley-Read-Hall (SRH) and Auger recombination discussed in the following section.

2.3.2.1 Shockley-Read-Hall (SRH)

Shockley, Read, and Hall were the first to examine deep levels of recombination of free carriers. During this process, electrons are trapped in deep energy levels and then recombine with holes in the valence band (i.e. through thermal activation).

For n-type semiconductors, the electrons are the majority carriers and the minority carrier lifetime (τ_{po}) is defined as :

$$\frac{1}{\tau_{po}} = N_t v_p \sigma_p \qquad (2.39)$$

Where σ_p is capture cross-section of the holes trap, v_p is the thermal velocity of holes, and N_t is the trap concentration. Likewise, for p-type semiconductors, when holes are the majority carriers and the minority carrier lifetime (τ_{no}) is defined as :

$$\frac{1}{\tau_{no}} = N_t v_n \sigma_n \qquad (2.40)$$

Where σ_n is capture cross-section of the electrons trap, v_n is the thermal velocity of electrons. Assuming a near-equilibrium state and holes are the majority, the lifetime of the SRH process (τ_{SRH}) may obtain given that $v_p \sigma_p = v_n \sigma_n$ and $\tau_{po} = \tau_{no}$:

$$\tau_{SRH} = \tau_{no} \left(1 + \frac{p_0 + p_1}{p_0 + n_o}\right) \qquad (2.41)$$

Where p_1 is the hole concentration when the Fermi level is located at the trap level. In the case where electrons are the majority and for a unique case $p_0 = n_o = n_i$ (intrinsic material):

$$\tau_{SRH} = \tau_{no} \left[1 + \cosh\left(\frac{E_t - E_{Fermi}}{K_b T}\right)\right] \qquad (2.42)$$

Where E_t is the energy level of the trap, E_{fermi} is the intrinsic Fermi level, which has a typical value close to the middle of the gap. In the case where trapped energy state E_t is located near the mid-gap, and if the Fermi energy is at the trap level, then the rate of SRH express as :

$$R_{SRH} = A_{SRH} n \qquad (2.43)$$

where n is the concentration of the free carrier, and A is the SRH coefficient which is inversely proportioned to the minority carrier lifetime (τ_o) as ~ ½τ_o and then the SRH lifetime is minimised (SRH recombination is most effective when the energy levels of the traps are near the middle of the bandgap). Inspection of equation (2.42) reveals that the SRH lifetime decreases with increased temperature, and therefore the efficiency of the band-to-band recombination decreases at high temperatures[57].

2.3.2.2 Auger recombination

Auger recombination occurs when an electron in the conduction band recombines with a valence band hole; the energy results from e-h paring transfer to a nearby carrier instead of an emitting photon. The nearby carrier is excited to a higher state and then loses its energy non-radiatively, i.e. through lattice vibration. Auger recombination is considered the main limitation in the III-V semiconductors since it reduces the luminescence efficiency, particularly for high excitation levels and high temperatures.

The Auger mechanism can be categorised based on the type of the bands involved; the four common ones are indicated in figure 2.13[59]. In the CHCC process, two electrons are involved; one electron from the conduction band recombines with the hole in the valence band. The energy released excites a second electron up in the conduction band, losing its energy via rapid phonon emission. This process is subjected to an n-type semiconductor, and the activation energy is defined as

$$E_a^{CHCC} = \left(\frac{m_e^*}{m_e^* + m_{hh}^*}\right) E_g \qquad (2.44)$$

Where m_e^* and m_{hh}^* is the electron and heavy hole effective mass, respectively. The other three Auger processes are CHLH, CHHH, and CHSH, involving one electron and

two holes. These processes are dominated by materials with an excess of holes (p-type semiconductors). In the CHLH transition, the energy released from recombination excites the hole from the light to the heavy hole state. In the CHHH process, the electron and hole recombination produces energy that moves the heavy hole deeper into the valence band.[60]. In the CHSH, the electron and hole pair release energy, which excites a hole from the split off-band to heavy hole and the activation energy is given by :

$$E_a^{CHSC} = \left(\frac{m_e^*}{m_e^*+2m_{hh}^*+m_{so}^*}\right)\left(E_g - \Delta_{so}\right) \quad (2.45)$$

Where m_{so}^* is the effective mass of holes in the split-off band, and Δ_{so} is the spin-orbit splitting energy. If Δ_{so} >> E_g, the CHSH process can be negligibly small compared to the CHLH transition[59]. However, if $\Delta_{so} \approx E_g$, then the CHSH process is significantly increased. It is possible to identify if CHSH is dominated process using the following equation:

$$E_a^{CHSC} = \frac{(E_t-\Delta_{so})/E_t}{\frac{m_e^*}{m_{so}^*}} > 1 \quad (2.46)$$

Where E_t is the electron and hole transition energy. If the condition in equation (2.46) is satisfied, the CHCC process is dominated.

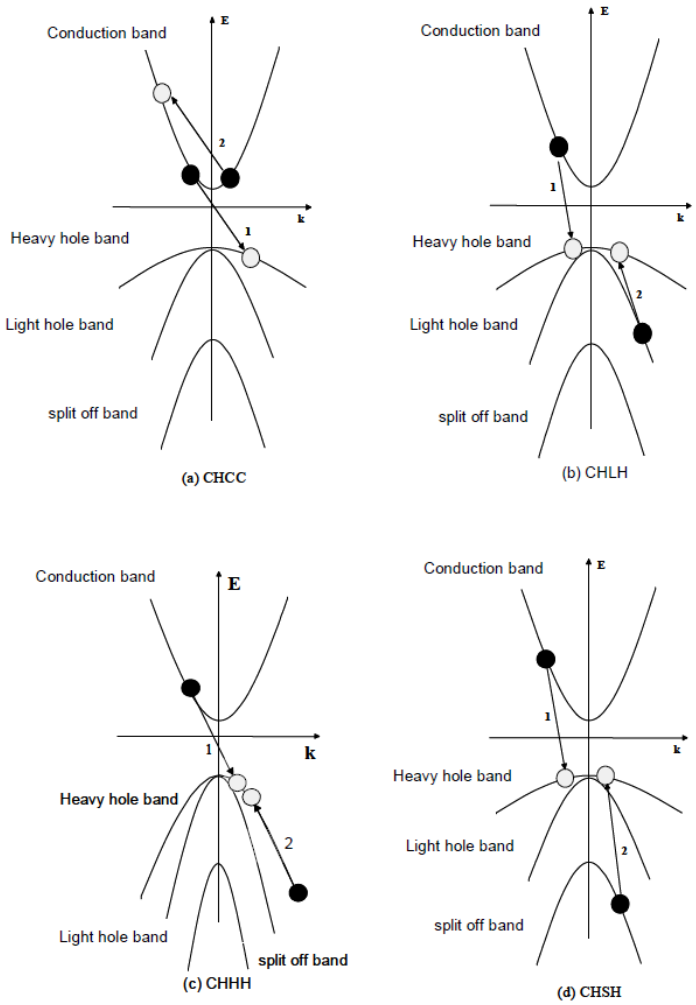

Figure 2.13: Schematic of various non-radiative Auger recombination processes near k = 0 for (a) CHCC, (b) CHLH, (c) CHHH, (d) CHSH processes[59]

2.4 Luminescence

Luminescence can be defined as the process in which light is emitted from semiconductor material due to the application of energy from an external source. In a semiconductor, this process occurs due to the radiative recombination of electrons and holes. This process is generated optically through an optical excitation source, i.e., laser (photoluminescence) or electrical via carrier injection into the PN-junction (electroluminescence); these topics are reviewed in the following section.

2.4.1 Photoluminescence

In photoluminescence (PL) a light source with energy greater than the material bandgap is incident on the sample. The photon energy promotes the electron from the valence band to the conduction band, creating electron-hole pair. The rate of photon absorption is determined by an absorption coefficient. The produced carriers can independently move until they recombine with carriers of the opposite type. Light is emitted if the radiative recombination occurs.

2.4.2 Electroluminescence

In an electroluminescence event, carriers are pumped into the device via metallic contacts. In doing so, electrons are injected from the n-type region while holes are from the p-type region. These carriers travel into the area of opposite conductivity (opposite direction) and then recombine either radiatively or non-radiatively. Several factors influence LED efficiency, such as competing radiative and non–radiative processes, carrier mobility, contact resistance, and current crowding and carrier leakage[61].

2.5 Light Emitting Diodes (LED)

When a voltage is applied across the P-N junction, free carriers diffuse through the depletion zone and recombine radiatively emitting photons. The following section discusses the principle of LED operation and the optical properties.

2.5.1 LED operation

An energy band diagram for separated p- and n-type semiconductors is shown in figure 2.14, where the Fermi energy level is different for each doped material. When joining two semiconductors, the Fermi level must be constant through the solid at thermal equilibrium, and therefore, the conduction and valence bands bend to accommodate a constant Fermi level. Due to the majority carrier electron density resting on the n-side, there will be an electron diffusion current to the p-type region, leaving a surplus of positive ions on the n-type region and excess negative ions on the p-side. Consequently, a region (W_D) near the PN-junction interface is formed known as the depletion region, or space charge region W_D. The dopants, acceptor in the p-type and donor in the n-type, form a built-in electric field. The fixed charges produce the built-in voltage which blocks carrier diffusion. The thickness of the depletion region (W_D) and degree of bending are influenced by many parameters such as the composition of the two materials, the doping, and the intrinsic carrier concentration.

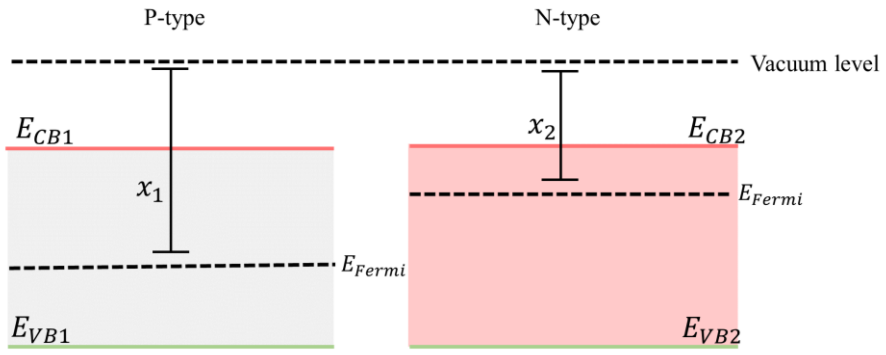

Figure 2.14: Schematic energy band diagram showing separated n - type and p - type layers with different Fermi energy levels.

2.5.2 Current-voltage characteristics

Considering figure 2.15 [57], let N_D be the donor concentration and N_A be the acceptor concentration for an abrupt PN-junction. Assuming all dopants are fully ionised, the free electron concentration is defined as $n = N_D$, and the free hole concentration is $p = N_A$. Additionally, unintentional defects and impurities are assumed to be absent and will not compensate for the dopants.

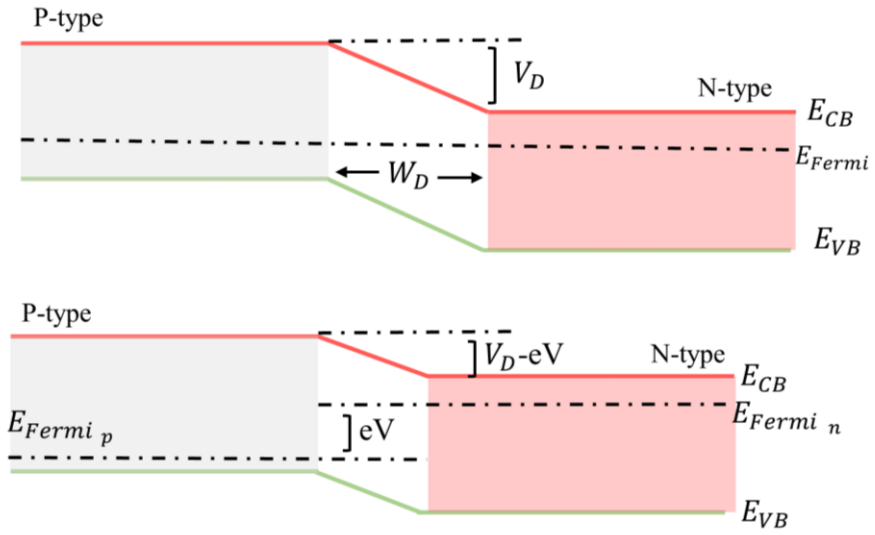

Figure 2.15: Schematic energy band diagram showing joined n-type and p-type semiconductor layers under zero bias / thermal equilibrium (top) and forward

bias(bottom). Under forward bias, minority carriers diffuse into the neutral regions, where they recombine[57].

In case of zero bias, let n_i be the intrinsic carrier concentration of the semiconductor, the built-in voltage V_D is defined by [57]:

$$V_D = \frac{K_B T}{e} \ln\left(\frac{N_A N_D}{n_i^2}\right) \quad (2.47)$$

The built-in voltage opposes free carriers to reach the oppositely charged region on the other side, passing through the depletion region W_D. The width of depletion region W_D is directly related to the Poisson equation and may determine by:

$$W_D = \sqrt{\frac{2\varepsilon}{e}(V_D - V)\left(\frac{1}{N_A} + \frac{1}{N_D}\right)} \quad (2.48)$$

Where ε is the dielectric permittivity of the material, and V is the externally applied voltage.

The Shockley equation describes the behaviour of current-voltage a cross PN-junction and therefore at low-injection level is given by equation (2.49). In forward bias, electrons and holes are injected into the n- and p-type, respectively. The carriers pass across the depletion region into the oppositely charged regions and recombine according to:

$$I = eA\left(\sqrt{\frac{D_p}{\tau_p}}\ \frac{n_i^2}{N_D} + \sqrt{\frac{D_n}{\tau_n}}\ \frac{n_i^2}{N_A}\right)\left(e^{\frac{eV}{K_b T}} - 1\right) = I_S\left(e^{\frac{eV}{K_b T}} - 1\right) \quad (2.49)$$

Where A is the cross-sectional area, D_p and D_n are the hole and diffusion constants, and τ_p and τ_n are the hole and electron minority lifetime, respectively. The term I_S denotes the reverse bias saturation current. In the case of typical forward bias, the voltage across

the diode is much greater $v \gg \frac{k_b T}{e}$ and therefore $\left[e^{\frac{eV}{K_b T}} - 1\right] \approx e^{\frac{eV}{K_b T}}$. Shockley equation may rewrite as:

$$I = I_S \, e^{\frac{eV}{K_b T}} \tag{2.50}$$

Consequently, equations (2.47) and (2.49) can be rearranged, and the Shockley equation is expressed as :

$$I = eA\left(\sqrt{\frac{D_p}{\tau_p}}\ N_A + \sqrt{\frac{D_n}{\tau_n}}\ N_D\right)\left(e^{\frac{e\,(V - V_D)}{K_b T}}\right) \tag{2.51}$$

The exponential term in equation (2.51) means that the current increases rapidly as the diode voltage (V) approaches the built-in voltage (V_D), the voltage at which $V \approx V_D$ is called the turn-on voltage (V_{th}).

Considering the separation of the Fermi level from the conduction band and valence band edge in figure 2.15 the energy difference between the conduction band edge in the n-type zone and Fermi level is described by Boltzmann statics according to the following:

$$E_c - E_{Fermi} = -k_b T \ln\left(\frac{n}{N_D}\right) \tag{2.52}$$

In the same manner, the energy difference between the valence band edge and fermi level in the p-type zone is given by :

$$E_{Fermi} - E_v = -k_b T \ln\left(\frac{p}{N_A}\right) \tag{2.53}$$

The Shockley equation in eq. (2.50) describes the theoretical I-V characteristic of the ideal diode, which can be modified to express the experimentally measured as follows:

$$I = I_S \exp(eV / n_{ideal} k_b T) \tag{2.54}$$

The term n_{ideal} is the diode ideality factor, which has a value of unity if the diode is dominated by current diffusion transport[62]. However, the ideality factor of a real diode is dominated recombination of carriers. In III-V semiconductor LEDs, a typical diode value is in the range of 1.1 ~ 1.7[63]. The divergence from the ideality diode factor is due to unavoidable resistance such as parallel resistance (R_p) and series resistance (R_s). A parallel resistance on the diode occurs when injected current bypasses the PN-junction via defects or surface imperfections. Series resistance is caused by either excessive contact resistance or the neutral region's resistance. Therefore, the I-V characteristic of the ideal diode (2.54) is rewritten considering the effect of resistance on the diode :

$$I - (V - IR_S)/R_p = I_S \exp(e(V - IR_s)/n_{ideal}K_bT) \quad (2.55)$$

2.5.3 LED efficiency

Ideally, electrons injected into the PN junction are converted to photons, giving 100% internal quantum efficiency. This is not the case in real diodes; several factors discussed in section 2.3.2 are responsible for degrading the LED's efficiency. In addition, some photons cannot escape from the LED because of the re-absorption processes within the device or because of the metallic contact surface. Therefore, the internal quantum efficiency (η_{int}) is defined as the number of photons emitted from the active region per number of electrons injected into the device. Mathematically, the expression of is given by[63]:

$$\eta_{int} = \frac{n_{\gamma_{emi}}}{n_e} = \frac{P_{int}/hv}{I/e} \quad (2.56)$$

Where n_γ is the number of photons emitted from the active region per second, n_e is the number of electrons injected into the active region per second, P_{int} is the optical power emitted from the active region, hv is the photon energy, and I is the injected current. Moreover, due to total internal reflection, extraction efficiency is also limited since the generated photons are less likely to escape into free space, where they are emitted at different angles. The light extraction efficiency (η_{ext}) is defined as the number of photons emitted into free space as a proportion of the total photons emitted from the active region, which is expressed as[57]

$$\eta_{ext} = \frac{n_{\gamma_{ext}}}{n_{\gamma_{emi}}} = \frac{P/hv}{P_{int}/hv} \tag{2.57}$$

Alternatively, the light extraction efficiency (η_{ext}) can be estimated from the reflective index of semiconductor material (n) according to[61]

$$\eta_{ext} = \frac{1}{n(n+1)^2} \tag{2.58}$$

The external quantum efficiency ($\eta_{external}$) is defined as the number of electrons injected into LED divided by the number of photons emitted into free space and can be written as[57,61]

$$\eta_{external} = \eta_{int}\eta_{ext} = \frac{P/hv}{I/e} \tag{2.59}$$

The power efficiency (η_{power}) is defined as a ratio of optical power ($P_{optical}$) divided by electrical power supplied into the LED (P_e) which expressed as :

$$\eta_{power} = \frac{P_{optical}}{P_e} = \frac{P_{optical}}{IV} \tag{2.60}$$

Chapter 3: Literature review

This chapter discusses an overview of the structures used to obtain light emission in the mid-infrared range [2 - 5 µm], including various active region designs such as bulk material, multi-quantum wells MQWs, and strained-layer superlattices SLS. The primary focus will be on the structure employing type-I and type-II band alignment MQW and SLS-based structures. In addition, the latest developments in MIR-LEDs, including state-of-the-art Interband Cascade and Resonant Cavity LEDs, are briefly presented.

3.1 Mid-Infrared Bulk Light-Emitting Diodes (MIR-Bulk LEDs)

Melngailis reported early work on InAs MIR LEDs in the late 1960s[64] employing a bulk InAs active region grown on a native InAs substrate exhibiting room temperature emission at λ = 3.7µm. In 1993, Dobbelaere et al. [38] reported the first bulk $InAs_{0.85}Sb_{0.15}$ LEDs showing emission spectra near 4.3µm as indicated in figure 3.1(a). The LED structure was grown on GaAs by MBE. The resulting EL spectra exhibited a dip in the spectrum at 4.3 µm, demonstrating the device's suitability for CO_2 sensing. One year later, Ashley et al. [65], demonstrated early InSb LED structures grown on native InSb substrate to provide strong carrier confinement and enable room-temperature operation with an emission wavelength of 5.5-5.8 µm as indicated in figure 3.1(b). This diode exhibited an output power of 740nW corresponding to the external quantum efficiency of $1.7x10^{-5}$ %.

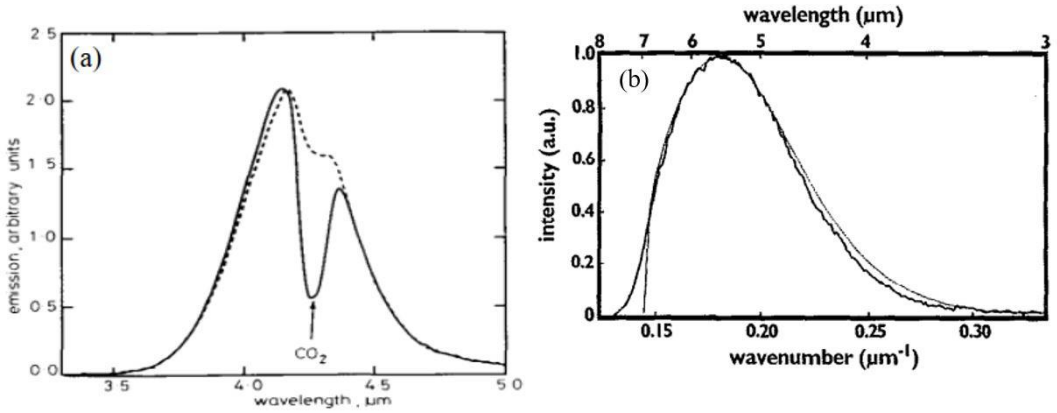

Figure 3.1: Electroluminescence spectra from an early bulk (a) $InAs_{0.85}Sb_{0.15}$ LED showing a CO_2 absorption feature in the spectra[38] and (b) InSb LED showing a peak near 5.8µm (0.21eV) at 294 K[65].

A different approach for bulk MIR-LEDs was introduced by Popov et al. [4] through the realisation of InAsSbP/InAsSb/InAsSbP heterostructure LEDs grown on InAs by liquid phase epitaxy (LPE) The room temperature electroluminescence spectrum exhibited a peak wavelength of 4.3 µm and a broadband linewidth of 800 nm. The optical power of 0.85 mW was measured under pulsed operation (1.2 A, 1 kHz in 5 µs) as shown in figure 3.2(a). One year later, Krier et al. [66] demonstrated a device based on InAsSbP/InAsSb/InAsSbP symmetrical double-heterostructure to achieve an output power >1 mW at 300 K with a peak emission wavelength of 4.6 µm as shown in figure 3.2(b). The active region consists of bulk InAsSb (Sb11%) grown by LPE. At constant 1.0 A pulse current, increasing the pulse width from 2 to 50 µs (5% duty cycle) decreases the measured output power by 30%.

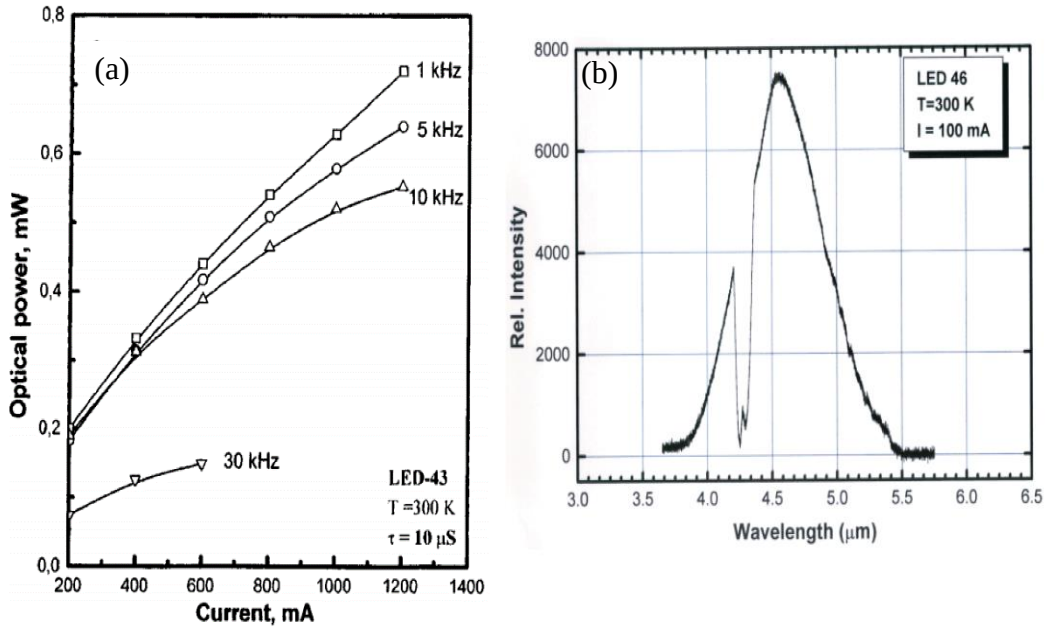

Figure 3.2: (a) Peak power of a 4.3 um LED at room temperature versus current at different repetition rate[4] and (b) Electroluminescence emission spectrum showing a peak at 4.6 μm again at room temperature[66].

Meanwhile, InSb-based LED structures were transferred from InSb to semi insulted GaAs substrates due to low cost and ability to achieve a specific gas absorption line in the 3 –5 μm region. Consequently, the InSb active region was replaced by $Al_{(x)}$ $In_{(1-x)}$ Sb using different alloy compositions to access other wavelengths. Hardaway et al. [67] demonstrated that varying the composition of MBE growth of bulk InAlSb on GaAs enables emission wavelengths up to 6μm. This was achieved by subdividing a single device into smaller series-connected devices, which improved the well-plug efficiency by a factor of 9. High et al., demonstrate that varying the alloy composition in bulk AlInSb could tailor the peak emission wavelength between 3.4 – 5.7μm[68] as shown in figure 3.3(a). Five devices showed room temperature emission spectra centred at 3.4 μm (Al= 0%), 4.2 μm (Al=2.5%), 4.6 μm (Al=5.2%), 5.3 μm (Al = 6.1%), and 5.7 (Al = 8.8%) and corresponding emittance powers of approximately (7.5, 27, 15, 12.5, and 3.4) mW/cm^2, respectively. A follow-up study of the temperature dependence of light-

current characteristics for bulk AlInSb active region devices revealed that increasing the Al content enabled a reduction in the Auger coefficient, but an increase in deep-level non-radiative defects associated with increased oxygen incorporation during growth resulted in a maximum efficiency at the composition of 2.5%[69] as shown in figure 3.3(b).

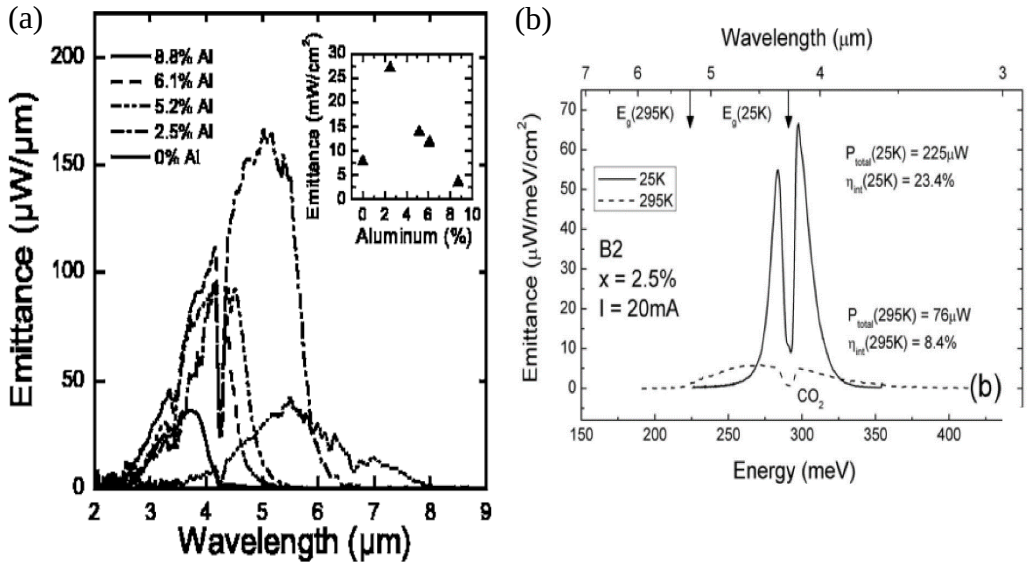

Figure 3.3 (a) The room temperature electroluminescence emission of $Al_xIn_{1-x}Sb$ LEDs shows the effect of varying Al concentration on the emission wavelength while the inset shows corresponding output power[68]. (b) Improvement in the bulk device with lower Al concentration (2.5%) shows maximum output power near room temperature at 76 μW[69].

Meanwhile, Krier et al., reported room temperature electroluminescent emission at 4.2 μm observed for bulk InAsSb (9%)[28]. The homo-junction *p-i-n* LED structure was grown on *p*-GaSb by LPE. Room temperature emission spectra were observed with absorption features at 4.25 μm corresponding to the CO_2 absorption, allowing using this device for CO_2 gas sensing. Two years later, Nash et al. [70,71] demonstrated the

electrical properties of bulk AlInSb grown by MBE on GaAs with an emission near 4.0 µm. The 16-element arrays of series-connected devices with a total emitting area of 1 mm^2 showed an average integrated intensity of 12mW/cm^2, suggesting suitability for use for hydrocarbon sensing. Enhancement of emission of AlInSb LEDs was achieved by using P-type contact grid geometry[72]. It was reported that optimisation of the top (P) contact geometry led to an improvement in the well-plug efficiency of a factor of 3. Using a grid-like top contact improved the performance at high current levels by reducing current crowding. Further development of AlInSb mid-infrared LEDs was reported by Fujita et al[73] in 2018 using a double InSb/AlInSb buffer. Electron/hole double layers were adopted, as shown in figure 3.4(a). The former is believed to increase the efficiency of light extraction in backside emission. Eight series-connected diodes were fabricated using Au/Pt/Ti electrodes. Current density versus voltage characteristics revealed that in the forward bias and with 100 mA drive current, the voltage drop was around 0.175 V for single diodes (100 mA current corresponds to 500 A/cm^2 for these devices) leading to the total voltage drop of 1.4V. However, in reverse bias, the leakage current density was around 6.5 A/cm^2. Room temperature electroluminescence (EL) emission intensity spectra confirm that by increasing the Al concentration from x=3.9 to 7.6%, the emission peak narrows, becoming more intense and shifting to a shorter wavelength, as indicated in figure 3.4(b). Recently, bulk InAsSb LEDs grown on Si by MBE were investigated by Delli et al.[74]. Electroluminescence spectra were measured, showing a broad emission peaking at 4.5 µm at room temperature with an output power of 6 µW (~1.2 mW/cm2) as shown in figure 3.5

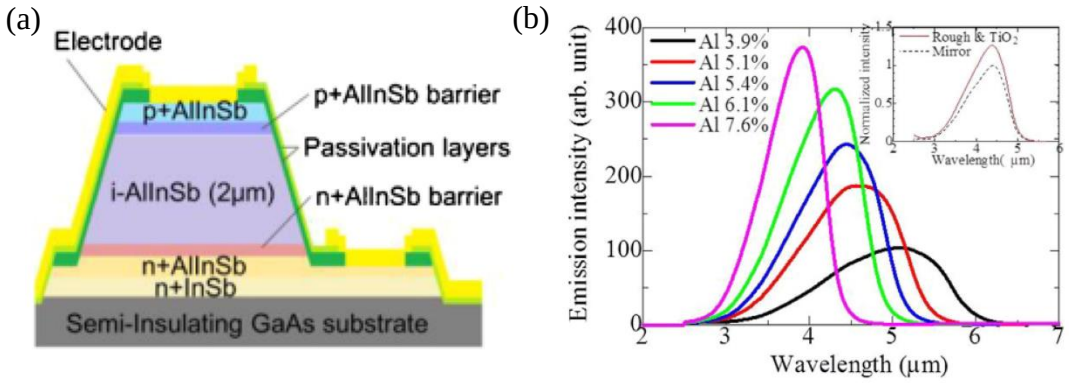

Figure 3.4: (a) Schematic diagram of the bulk $Al_xIn_{1-x}Sb$ LED grown on GaAs and (b) room temperature electroluminescence emission for varying Al concentration from 7.6% to 3.9% to increase emission wavelength to 5.2 μm[73].

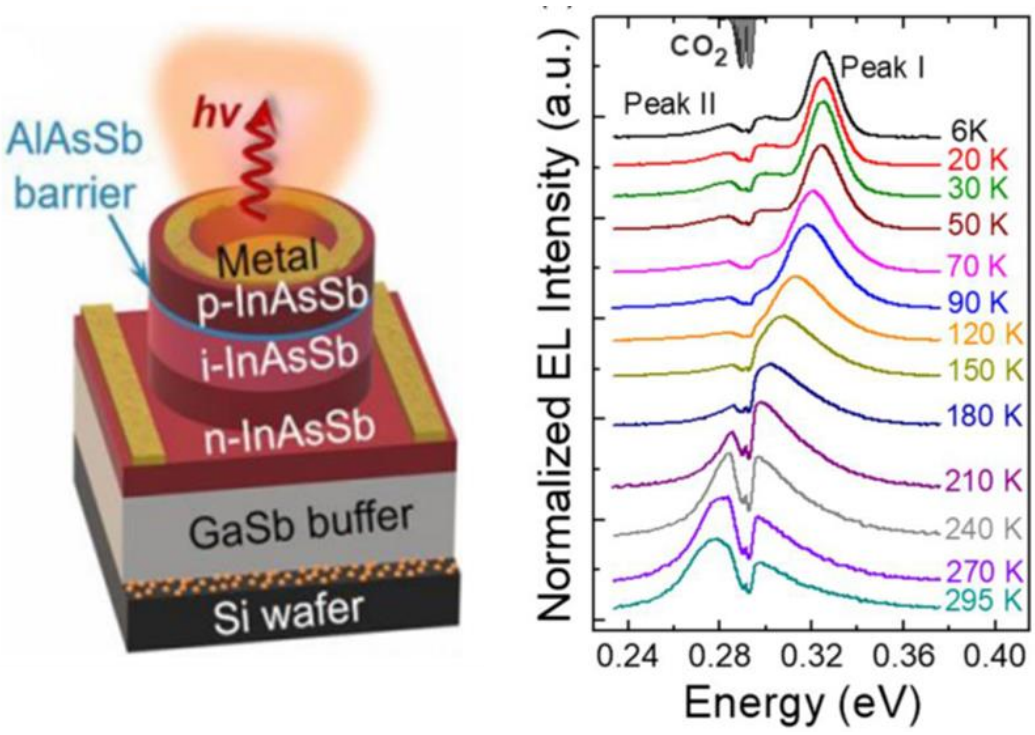

Figure 3.5: Schematic diagram of the bulk $lnAs_{1-x}Sb_x$ LED grown on Si (left) and temperature dependent of normalized electroluminescence spectra showing two peaks (0.325 eV) and (0.29eV) at 6 K (right)[74].

3.2 Mid-Infrared Single Quantum Well (MIR-SQW), Multi-Quantum-Well (MIR-MQW) and Superlattice (MIR-SL) LEDs

3.2.1 SQW based emitters

Heterojunction structures for MIR-LEDs continue to attract attention. Quantum well designs offer the ability to tune the bandgap by varying both the composition and the layer thickness. In 1998 Tang et al[39,75] reported InAs/InAsSb SQW LEDs with different Sb compositions (16 % and 26 %). Both EL structures were grown on native InAs substrate by MBE. The LED device with low Sb content (16 %) shows room temperature operation peaking at $\lambda = 5.29$ µm with a quasi-CW output power of 5 µW. However, the higher Sb content (26 %) LED revealed long-wavelength emission $\lambda = 8.15$ µm corresponding to an output power of 24 µW as shown in figure 3.6. Two years later, Heber et al. [76] reported a 4.2 µm SQW LED with room temperature operation and a broad emission of about 40 meV, an internal quantum efficiency of 2.6 % and a pulsed output power of more than 110 µW/A. The structure consisted of an InAs/InAsSb active region followed by InAlAs (Al = 17 %) EBL. The structure was grown on a native p-InAs substrate by MBE. In comparison with similar LED without EBL, the efficiency was enhanced by a factor of more than 6.

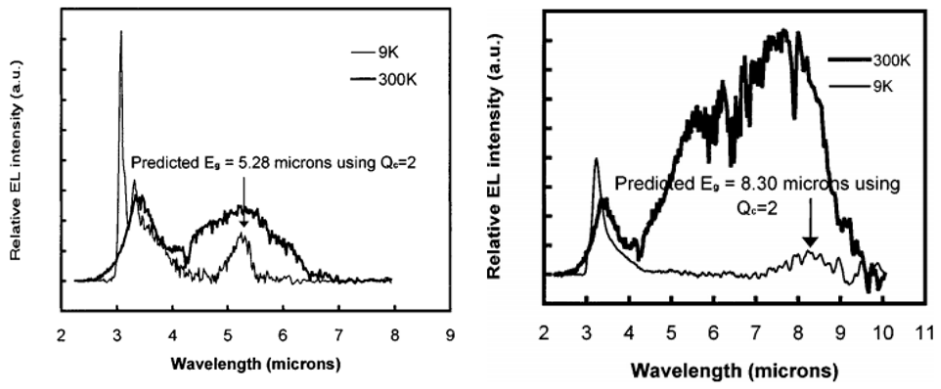

Figure 3.6: Electroluminescence spectra form InAs/InAsSb SQW measured at 9 k and 300 K for lower Sb contents (left) and higher Sb content (right)[39,75].

3.2.2 Type-I based MQWs emitters

GaInAsSb-based material systems

Early work on GaInAsSb type I multi-quantum well (MQW) active regions was published by Choi and Eglash in 1992[77]. The reported structure used a GaInAsSb/AlGaAsSb MQW laser structure on GaSb and exhibited room-temperature operation at λ = 2.1 μm. Many efforts were made to extend the operation wavelength beyond λ = 3 μm by increasing the In content in the well, resulting in room temperature output powers ranging from 0.06 – 1 W for 3.1 and 2.4 μm emission wavelengths respectively [78–81]. The reduction of the output power with increasing wavelength was primarily attributed to the leakage of holes out of QW since the necessary increase of As fraction to limit the strain to 2% also reduces the valence band offset between well and barrier: the depth of the QW for holes decreases from 175 meV for 2.5 μm to 85 meV for 2.8 μm[79]. A different approach again using the GaInAsSb material system was taken by Jung et al., who reported operations between 3.3 – 3.66 μm[82,83]. It was concluded that the GaSb-based structure enables an extended emission wavelength at ~ 3.7 μm by changing the MQW composition, as indicated in figure 3.7.

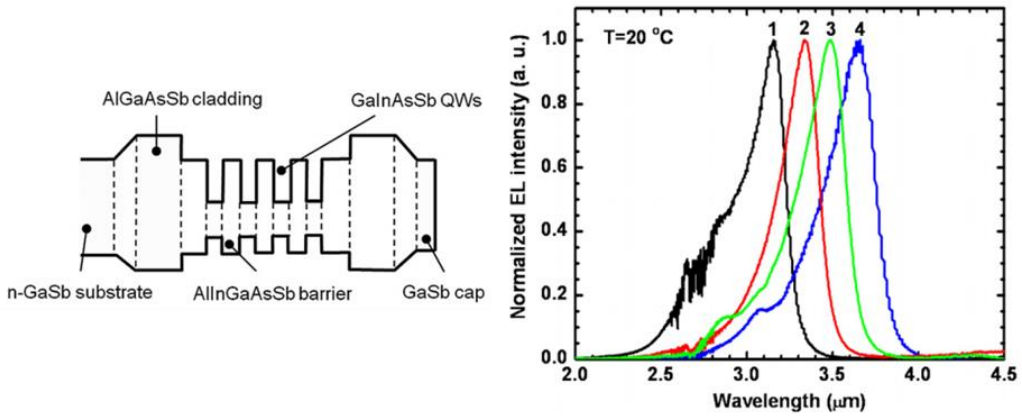

Figure 3.7: Schematic diagram for a GaSb-based GaInAsSb MQW LED (left) and room temperature electroluminescence spectra for different MQW compositions (right)[82,83]

InAs/InAsSb based material systems

Early work on Type-I InAsSb MQW was reported by Grietens et al. [84]. They reported EL emission from a (13nm) InAs/ (7nm) InAsSb (Sb 10%) MQW grown by MBE on a native InAs substrate. The low-temperature dependence of EL spectra shows two emission peaks at $\lambda = 3.4$ and 3.8 μm from radiative recombination related to the InAs and MQW, respectively. However, at room temperature, only InAs emission was observed. This has been attributed to the poor electron trapping in the quantum well structure due to the relatively small InAs/InAsSb(Sb 10%) conduction band offset (see figure 3.8(a). The MQW LEDs produced a maximum output power of 27.5μW (pulsed operation, 740 mA current, 30 kHz, 0.6 % duty cycle). A strained layer superlattice design was first reported by Biefeld[30] The structure featured a Type-I band alignment designed to reduce non-radiative Auger recombination by increasing the valence band offset (light-heavy hole splitting) to 69meV. The structure consisted of 40 periods of (7.5nm)InAsSb(Sb = 13 - 20 %)/(8.4nm)InAsP(P = 24%) grown on InAs by MOCVD. At low temperature ($T < 20$ K) , the PL spectra exhibited a red sift from 3.5 – 4.4μm when Sb content change from $x = 0.13$ to 0.2. This structure was incorporated into LED again with Sb = 12%. The InAsSb/InAsP SLS LED is the brightest 4 μm, room temperature device reported by MOCVD. Operating the device at 1 kHz, 50% duty cycle, 200 mA average current, the average output power of the LED was 80 μW at 300 K (see figure 3.8(b))

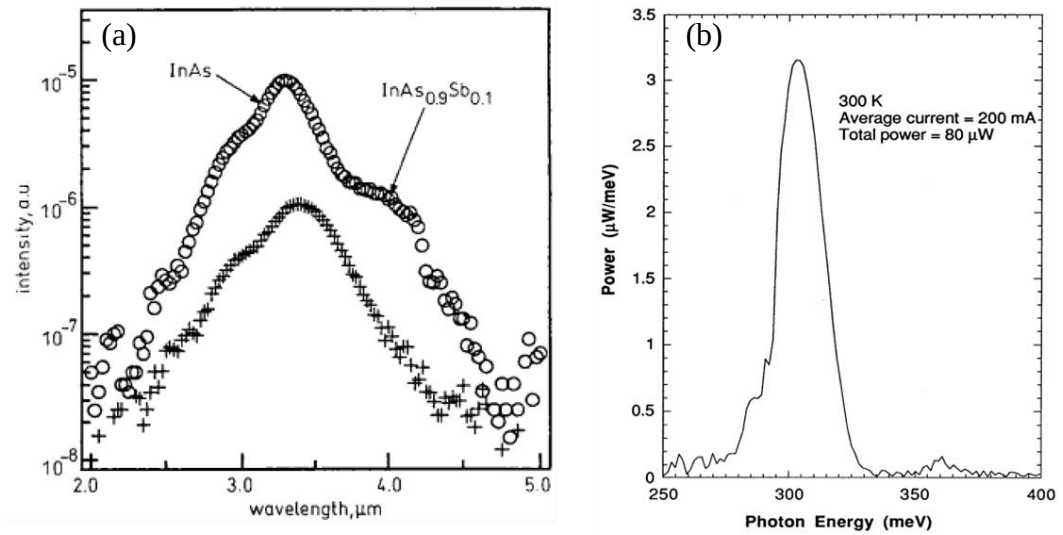

Figure 3.8: Electroluminescence spectra reported for (a) InAs/$InAs_{0.9}Sb_{0.1}$ MQW at 77 K (top) and 300 K (bottom) showing quenching of the InAsSb peak[84] and (b) an early $InAs_{0.88}Sb_{0.12}$ /$InAs_{0.88}P_{0.25}$ SLS LED structure demonstrating 80μW output power for a 4.0μm wavelength[30].

A decade later, Carrington et al[85] report EL emission from $InAs_{0.942}Sb_{0.05}N_{0.008}$/InAs MQW active region grown on InAs by MBE (see figure 3.9 (a)). At room temperature, the mean peak of the LED occurred at ~3.54 μm, with a corresponding output power of 6 μW and internal quantum efficiency of 1% (figure 3.9 (b)). It was concluded that additional nitrogen reduces the bandgap and can change the band alignment from type-II to type-I, increasing the electron confinement and e-h wave function overlap.

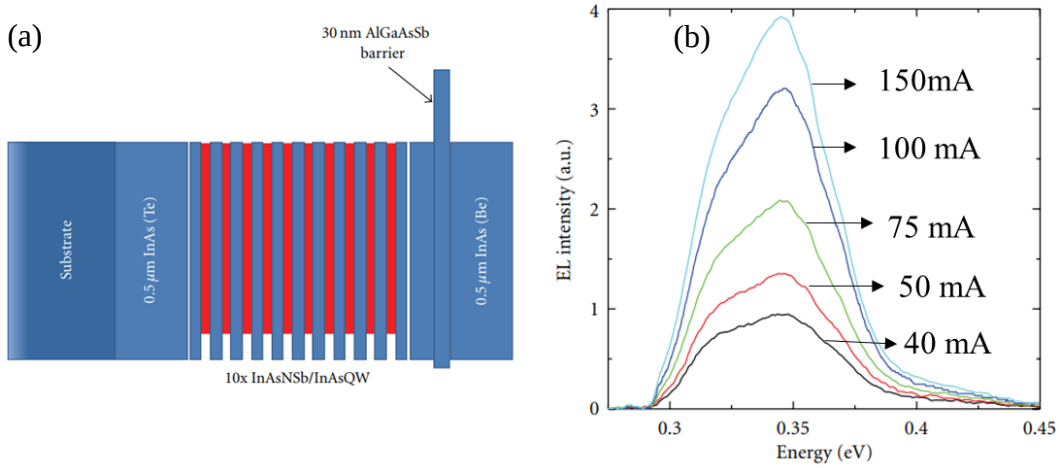

Figure 3.9: (a) Schematic diagram of the InAs/InAs$_{0.942}$Sb$_{0.05}$N MQW LED structure and (b) room temperature electroluminescence spectra measured at different injection currents[85]

AlInSb-based material systems

Meanwhile, an AlInSb MQW-based structure was reported in early 2006 by Nash et al. [71] demonstrating the epitaxial growth of InSb/Al $_{(x)}$ In $_{(1-x)}$ Sb SQW active region on GaAs. The large lattice mismatch between GaAs and InSb (>14%) was accommodated using a 3µm thick Al $_{(0.0875)}$ In $_{(0.9125)}$ Sb buffer layer. Two single quantum well samples QW1 and QW2 consisting of (40nm) InSb/ (20 nm)Al $_{0.077}$In $_{0.923}$Sb and (20nm) InSb/ (20 nm) Al $_{0.143}$In $_{0.857}$Sb receptively were fabricated into an LED structure. As shown in figure 3.10 the room temperature of EL spectra mean peak occurred at λ= 5.43 and 5.25 µm corresponding to emittance of ~ 38 µW/meV/cm^2 and 82 µW/meV/cm^2 for QW1 and QW2 respectively. A different approach to MIR LEDs was adopted by Aziz et al. [86], offering multiple wavelength spectra. The structure consisted of four active regions, including bulk AlInSb and three AlInSb/InSb/AlInSb QWs with different QW thicknesses grown on GaAs (see figure 3.11). Electroluminescence of the LEDs measured at room temperature exhibited four emission peaks corresponding to active region emission at 3.40 µm, 3.50 µm, 3.95 µm, and 4.18 µm.

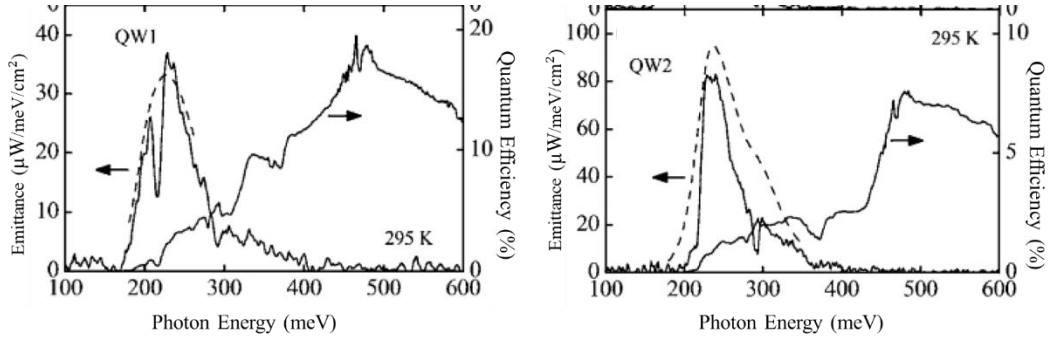

Figure: 3.10 Measured room temperature emittance and spectra response for QW1(left) and QW2 (right), the dashed line represents the predicted emittance[71].

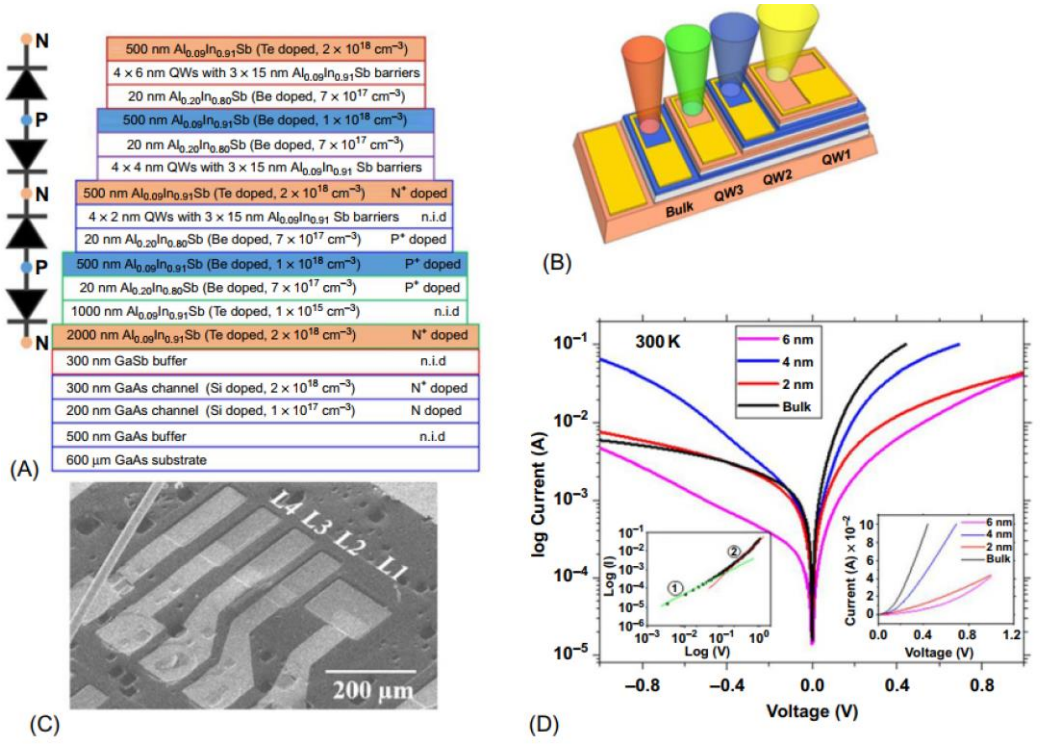

Figure 3.11: (a) Schematic diagram of the multi-spectral LED. (b) A 3D Schematic of fabricated LED where different colours correspond to different emission wavelengths. (c) The SEM of the final fabricated device. (d) Current-Voltage measurements for all LEDs described above at room temperature; the two insets show log-log (I-V) where two regions are apparent (left) and linear forward voltage-current(right)[86].

Gu et al. [87] reported the growth of the (10 nm)InAs/(15 nm)Al $_{0.83}$In $_{0.17}$As type-I MQW material system on InP and GaAs. Adopting a thin (300nm) In $_{0.83}$Al $_{0.17}$As

metamorphic layer (MBL) was reported to reduce the lattice mismatch between InAs and GaAs, showing a promising photoluminescence peak at λ = 2.9 μm at 300K. In addition, the photoluminescence study shows that. as temperature increases, the optical quenching of GaAs -based samples is much quicker than those of InP-based samples. At room temperature, the intensity of the InP-based design was five times higher than that of GaAs-based due to defects originating from the large lattice mismatch between the epi-layer and substrate, as indicated in figure 3.12. The realisation of InAlAs MBL attracted interest for transistor applications due to its good electronic performance[88]. In addition, the use of InAlAs MBL with the InAs/InGaAs MQW active region was necessary to extend emission wavelength beyond λ = 2.9 μm at room temperature [89]. Recently, Repiso et al. [27] reported the growth using a (10 nm) $InAs_{1-x}Sb_x$/ (20 nm) $Al_yIn_{1-y}As$ MQW active region into semi-insulted GaAs substrate by MBE. It was reported that by varying the Sb contents in the well from (Sb = 0 to 10%) corresponding PL peak emission observed red-shifted from λ = 2.83 μm (Sb = 0 %) to λ = 2.99 μm (Sb = 10 %) at 300 K (see figure 3.13)

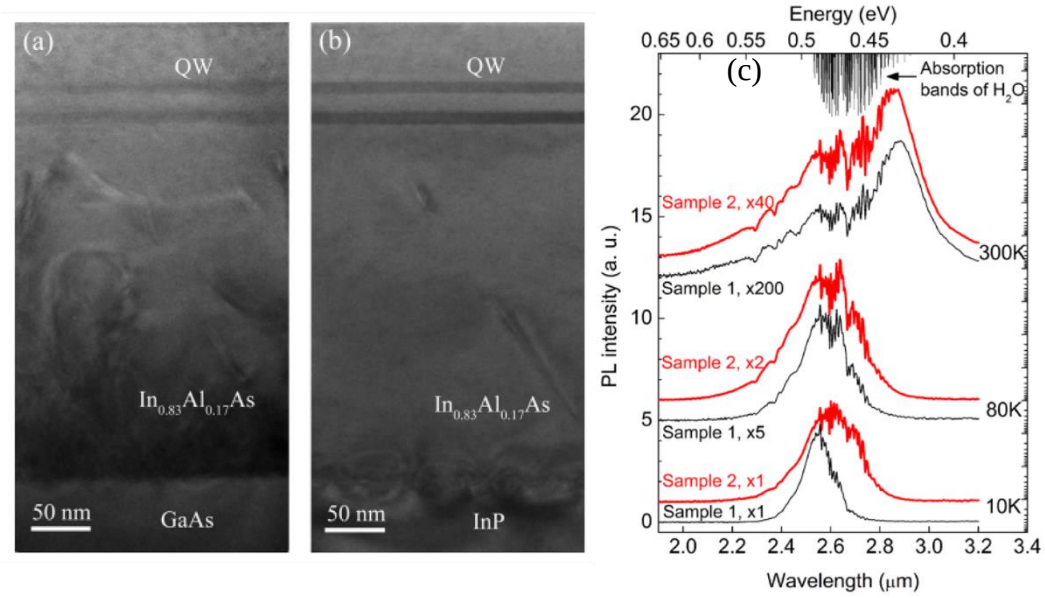

Figure 3.12: TEM images of (a) GaAs-based sample and (b) InP-based sample and (c)temperature dependent of photoluminescent emission spectra showing higher intensity in the InP-based sample (red spectra) when compared to GaAs sample (black spectra)[87].

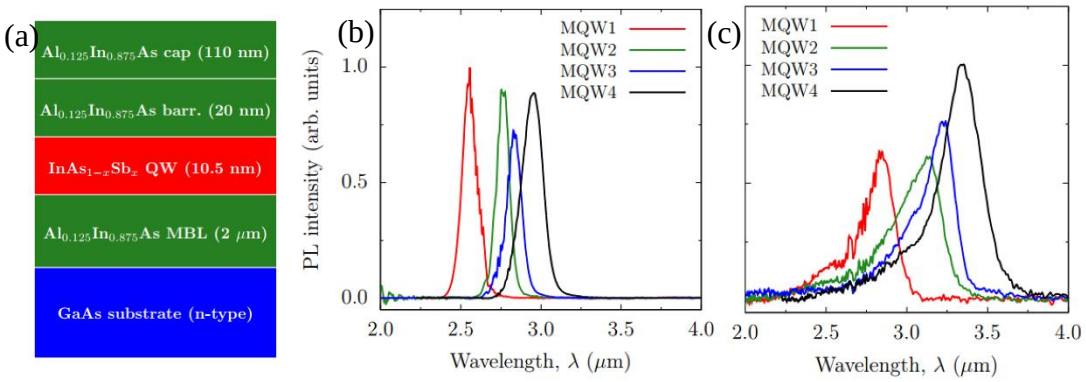

Figure 3.13:Schematic diagram of InAsSd/AlInAs MQW grown on GaAs substrate. (b) Photoluminescent emission spectra for different Sb contents 0 % red line , 3% green line, 6 % blue line and, 10 % black line measured at (b) 4 K and (b) 300 K[27]

3.2.3 Type-II based MQWs emitters

Extending the wavelength range and radiative rate of MID-IR LEDs is challenging at room temperature. A possible solution is introducing an III-V semiconductor materials system that features type-II band alignment. The spatial separation between electron and hole is necessary to reduce non-radiative recombination (such as Auger recombination). Type II systems offer relatively large conduction and valence band offsets for enhanced electrical confinement and weaker temperature dependence of the Auger rate[90,91]. As a result, this topic was attractive to many research groups where some employed different material systems, including InAs/InAsSb and state-of-the-art InAs/GaSb.

InAs/InAsSb based material systems

Several authors have investigated InAs/InAsSb MQW and SLS heterostructures. The first demonstration of a superlattice using this material system was in 1995 by researchers from Imperial College London[39]. The reported structure employed ~2 µm thick InAs/InAsSb (Sb 9.5 – 39 %) strained layer superlattice active region integrated on GaAs substrate. Due to a significant lattice mismatch between GaAs and InAs, a metamorphic buffer layer (MBL) structure containing dislocation-filtering layers of ~ 1 µm thick InAsSb (Sb 4.7-16%) were adopted. At 12 K, PL samples exhibited emission in the wavelength range of 4 - 11 µm. Among considered samples, three LEDs structures were fabricated, and the Sb content in the SLs ranged from 0.095% to 0.274% corresponding to different SLS periods. The temperature dependence of the EL spectrum was observed and was limited to temperatures below 81 K in the highest Sb contents SLS structure. However, the lowest antimony (Sb ~ 9.5%) exhibited room temperature emission at a wavelength of ~5 µm corresponding to an optical power of 200 nW at 100 mA injection current as shown in figure 3.14 The reported internal quantum efficiency was 0.05 % and external quantum efficiency 0.0007%. This structure was transferred to lattice-matched InAs substrates, as reported by Hardaway et al. [92]. Room temperature operation from InAs/InAsSb SLS active region was observed at $\lambda = 4.2$ µm offering 140 µW output power. This achievement was possible by employing a 1 µm period of (20nm) InAs/ (20 nm) $InAs_{0.915}Sb_{0.085}$ on a p-InAs substrate (see figure 3.15). The incorporation of the p-AlSb EBL layer increases the efficiency of SLS LED by a factor of 3.5 when compared to SLS LED without EBL. The following work at Lancaster University has included the fabrication and characterisation of pre-deposition Sb InAs/InAsSb MQW LEDs[93]. The structure consists of 10 periods of (7nm) InAs/ (24nm) InAsSb (Sb 13%) MQW active region

lattice grown on a ~ 300nm thick p-InAs buffer layer on lattice-matched InAs substrate. The 300 K EL spectra show peak emission occurred near 4 µm, as shown in figure 3.16(a). The LED output power under quasi-continuum drive condition CW (1 kHz at 50 % duty cycle) was 1.4 µW corresponding to internal quantum efficacy of 0.2% at room temperature. Three years later, Carrington et al[94] reported the temperature dependence of electroluminescence spectra of InAs/InAsSb (Sb=8%) MQW LEDs. The structure consisted of 10 periods of (8.5nm) InAsSb/ (24.5nm) InAs MQW active region followed by a 30 nm of AlGaAsSb EBL layer and was grown on an *n*-InAs substrate using MBE. It was reported that the inclusion of an AlGaAsSb EBL at the p–layer interface enhanced the room temperature electroluminescence intensity by a factor of 5. The device exhibited room temperature electroluminescence peaking at 3.7 µm (0.33 eV) with an optical output power of 12 µW at 100 mA injection current corresponding to an internal quantum efficiency of 2.2% (see figure 3.16(b)).

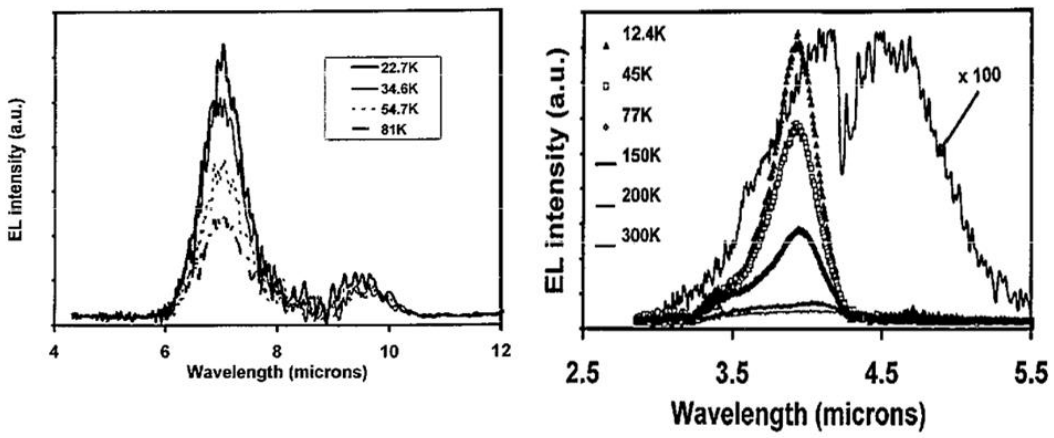

Figure 3.14: Early electroluminescence spectra from type-II InAs/InAs$_{1-x}$Sb$_x$ SLS LEDs on GaAs e showing a maximum operating temperature of 81 K for higher Sb contents (left) and possible 300 K operation for lower Sb content (right)[39].

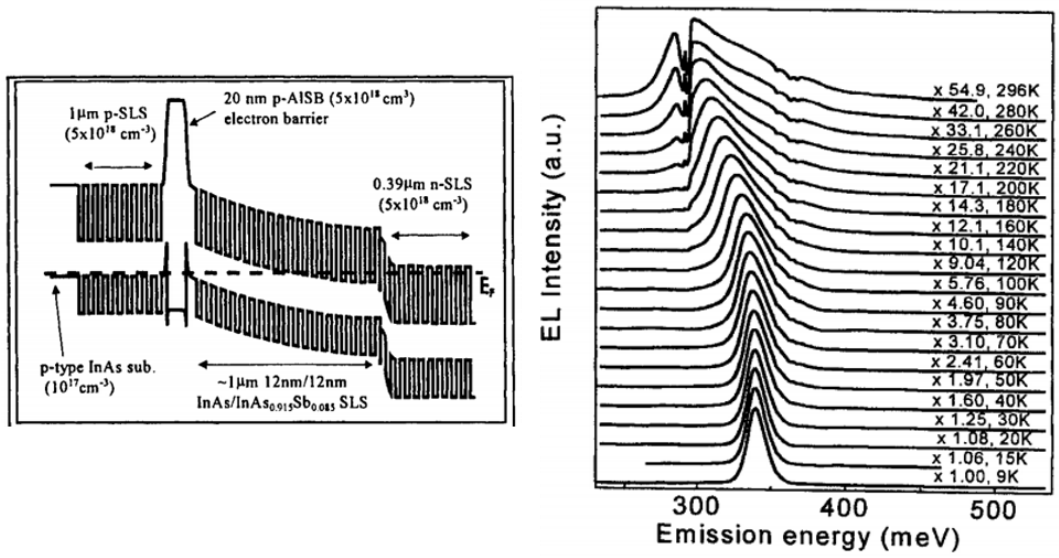

Figure 3.15:Band diagram of InAs/InAsSb SLS LED band structure showing the integration of SLS into InAs substrate and the valence band offset of the AlSb EBL(left).Temperature dependence of electroluminescence showing a 296 K operation at λ ~ 4.2µm(right)[92].

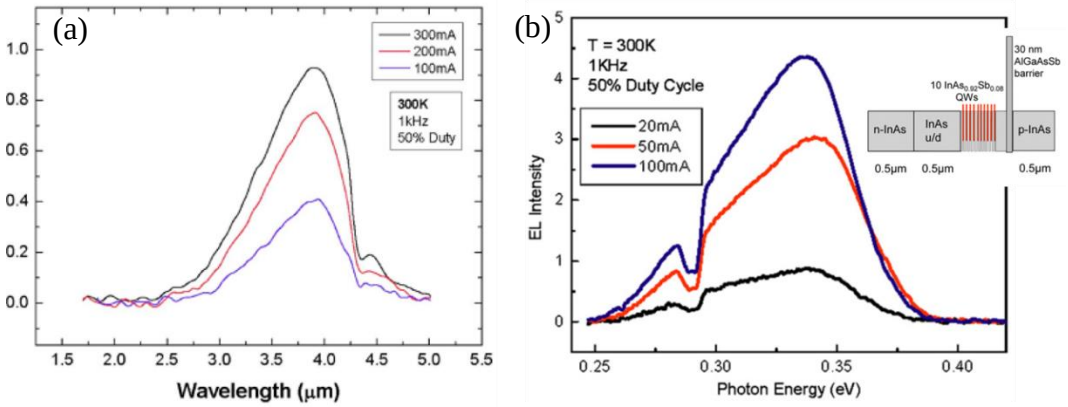

Figure 3.16: Room temperatures electroluminescence spectra peaking at λ ~ 3.7µm for (a) higher Sb content (13%) and (b) lower Sb content (8%) MQWs which achieved a maximum output power of 12µW.The inset shows a schematic diagram of the MQW structure featuring AlGaAsSb EBL[94].

More recent studies focused on structure growth, carrier lifetime, and localisation effects in InAs/InAsSb strained layer superlattice[29,34,35] . For example, Aytac et al. [29] explored the effects of layer thickness and alloy composition on carrier lifetimes in mid-wave infrared InAs/InAsSb superlattices. Despite the SLS thickness and Sb content variation, all samples exhibited a constant 5.2 μm bandgap energy. It was concluded that the minority carrier lifetime monotonically increased from 4.5 μs to 10 μs, with the samples with higher Sb concentration and shorter SL periods having longer lifetimes. In addition, the extracted radiative and Auger coefficients were observed to decrease exponentially with increasing Sb concentration and reducing period thickness, both by approximately a factor of two. These results were encouraging to report enchantment in the InAs/InAsSb SLS structure to achieve room temperature operation[35]. For infrared detector applications, Steenbergen et al. report a photoluminescence study of type-II InAs/InAsSb SLS on GaSb. They were chosen over InAs/GaSb material system due to the long minority carrier lifetime and reduction of Shockley Read-Hall recombination[95–97]. The reported PL structure consists of 6.7 and 8.2 nm thick of the InAs layer and 1.8 and 2.5 nm thick of the InAsSb layers for samples A and D. The number of SLS periods was also 58 for sample A and 47 for sample D. Among the samples considered, two samples (with Sb contents =< 0.35) were reported to peak at 5.90 μm (210 meV) and 8.26 μm(160 meV) (samples A and D, respectively)(see figure 3.17). The results show that carrier localisation below 60 K is evidenced by the PL peak blue shift of ~ 8meV and the non-monotonic behaviour of the FWHM with increasing temperature. Recently, Keen et al[98] reported electroluminescence spectra of InAs/InAsSb SLS LEDs with two different Sb compositions (of 4% and 6%) grown on a lattice-matched n-InAs substrate. The structure used 50 periods of (14 nm) InAs/ (14nm) InAsSb SLS for the active region.

Simulation results indicate that the broad emission spectra at room temperature involve e-h recombination from additional confined hole states (see figure 3.18). At room temperature and under 100 mA quasi-CW injection current, the results show the emission spectra peaked at 4.1 µm with an output power of 8.2 µW for the InAs/InAsSb (Sb = 4%) LED, and at 4.7 µm with an output power of 3.3 µW for the InAs/InAsSb (Sb = 6%) LED.

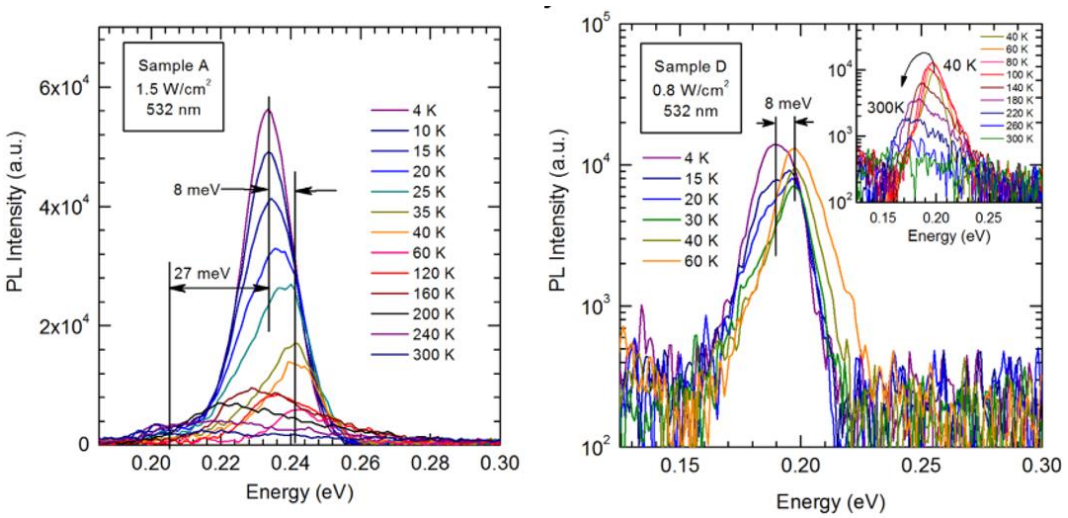

Figure 3.17: Temperature-dependent PL spectra for sample A (left) on a linear scale and sample D (right) on a semi-log scale. The peak blue shifts by 8 meV between 4–60 K and 4–30 K for samples A and D, respectively, before red shifting with increasing temperature[35]

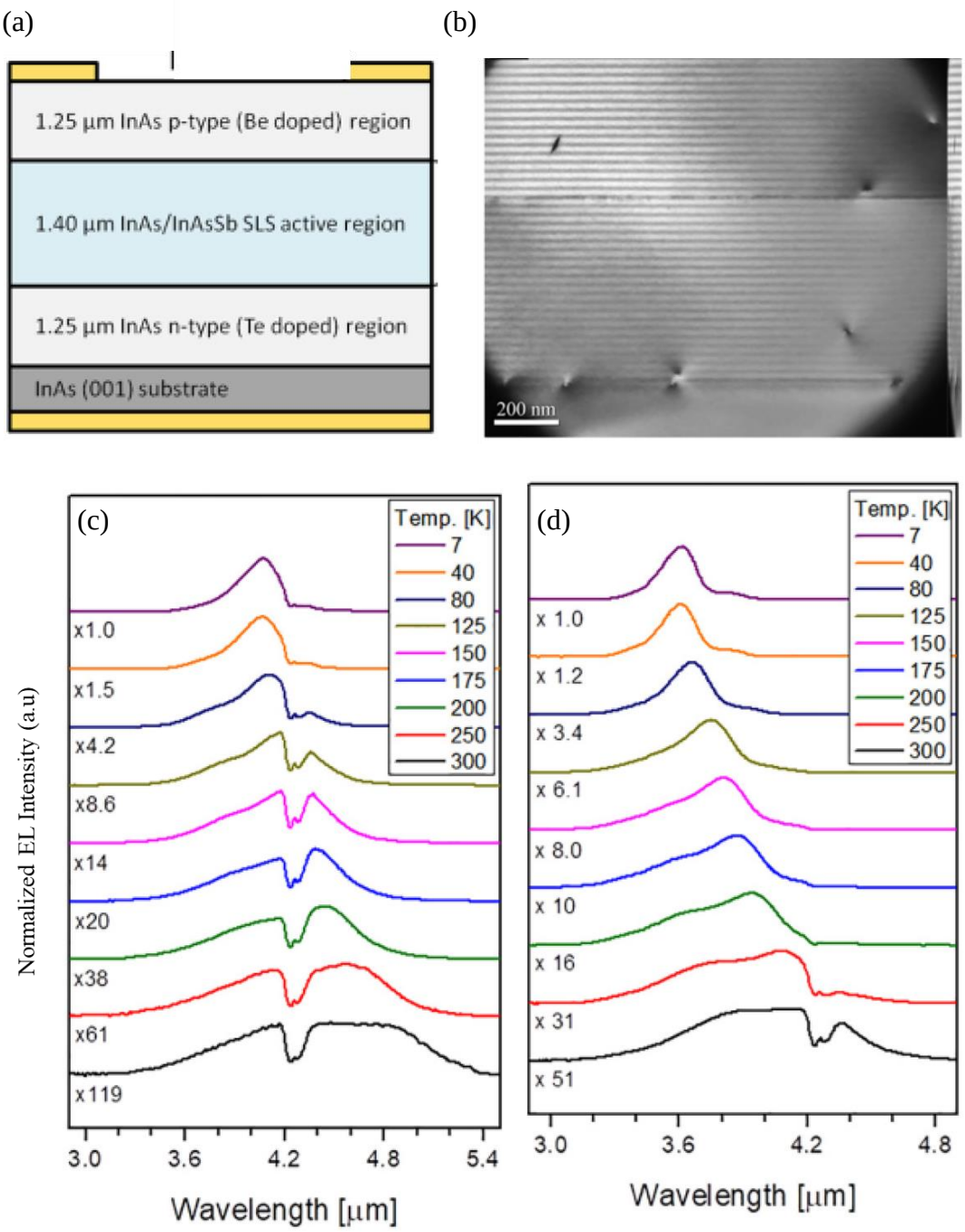

Figure 3.18: (a) Schematic of the LED structure containing the InAs/InAsSb SLS active region. (b) TEM image of SLS (Sb 6 %) showing some threading and misfit dislocations. (c) and (d) Normalized electroluminescence spectra of the InAs/InAsSb SLS LEDs with Sb composition of 4% and 6%, respectively[98].

3.3 Mid-Infrared Interband Cascade Light-Emitting Diodes (MIR-ICLEDs)

The concept of Interband the Interband Cascade light-emitting diode ICLED is that an injected electron can recombine with a hole emitting a photon and then tunnel through to the next emitting region n times. In this case, an electron can emit N photons by travelling through N emitting regions which leads to an increase in the operating voltage by a factor N. In 1997, Yang et al. [99] demonstrated Interband Cascade electroluminescence in the 5 - 8 µm spectrum region by cascading type-II InAs/GaInSb/AlSb active region. The structure was grown on GaSb substrate by MBE comprising 15 periods of the active region separated by an n-type doped InAs/AlInSb injection region. At 77 K, the EL spectra exhibited peak emission near 5.7 µm corresponding to an output power of 700 nW (0.7A), as shown in figure 3.19a. At room temperature, the EL peak was red-shifted to nearly 7.5 µm producing an output power of 300 nW. Das et al reported room-temperature emission from type-II InAs/GaInSb/InAs superlattice employed in an ICLED grown on GaSb [100]. The active region consists of 8 InAs/GaInSb/InAs SLS and 18 periods of the same active region, each separated by graded n- InAs/AlInSb tunnel injector. It was reported that the external quantum efficacy of the 18-period LED is 0.65%, corresponding to an output power of 300 µW peaking at 3.8 µm at 300 K (see figure 3.19(b)). It was concluded that thinning the GaSb substrate from 500 µm to 25 µm improves the intensity of the light by a factor of 6. Rapid improvements in the ICLED field have been made where some groups report a comparison of MBE growth of InAs/GaSb SLS LEDs on GaAs and GaSb substrate[101]. Both devices were identical in structure and differ only by the substrate. Both devices operated at 4.8 µm at room temperature; however, the device grown on mismatched GaAs substrate was reported to record a higher peak radiance of 1.06 W/cm^2-sr than 0.69 W/cm^2-sr obtained from GaSb devices as shown

in figure 3.20. At a low injection current, the device performance on the mismatched substrate was significantly low due to higher SRH recombination. The performance of the ICLED device can be improved by increasing the number of stages[102]. The active region consists of 20 periods of InAs/GaSb SLS LED separated by AlInAsSb/p-GaSb tunnel injection. Peak emission at 3.68 µm exhibited spectra radiance of 0.5 W/cm^2-sr at 77k.

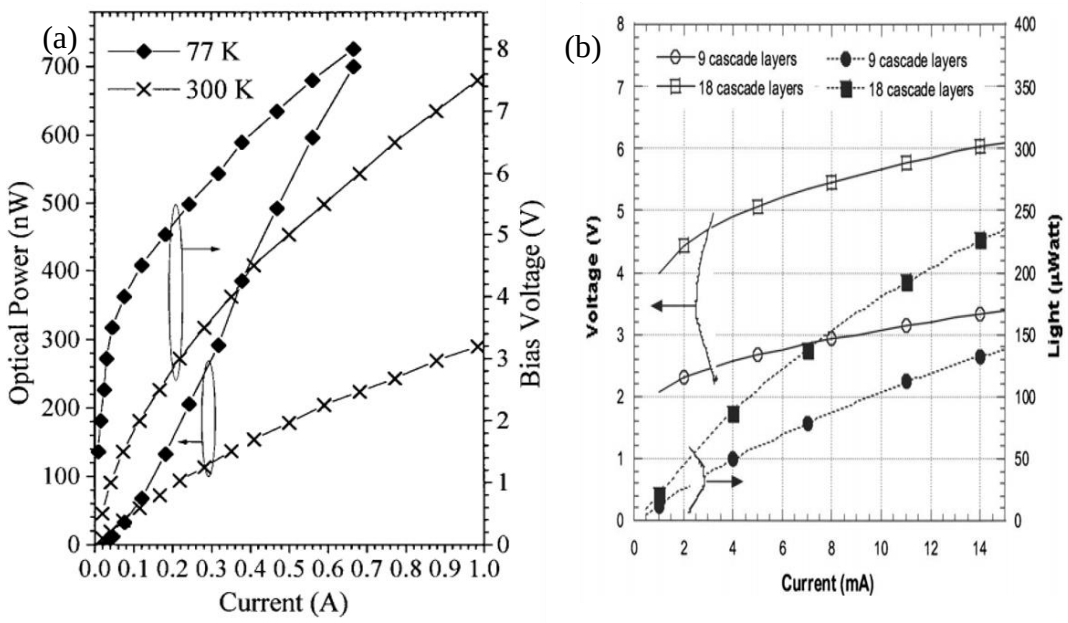

Figure 3.19: (a) An early type-II InAs/GaInSb/AlSb ICLED showing the output optical power as a function of current and the Current-Voltage characteristics where 300nW was reported for λ = 5.7 µm[99] and (b) higher output power for an emission band of 3.7 µm reported with increasing numbers of the active region[100].

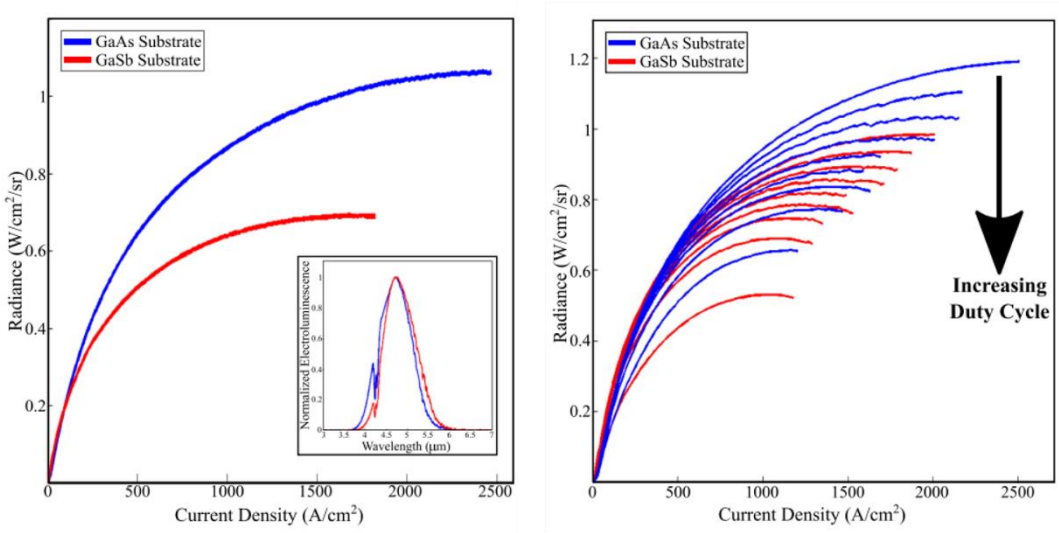

Figure 3.20: Comparison of type-II InAs/GaSb ICLED grown on GaAs(blue colour) and GaSb(red colour). The radiance as current function is presented in the left, where insets show 77 K electroluminescence spectrum of devices driven at 50mA. The radiance as a function of current density is presented in the right measured at 83 K where the duty cycle varied from 10 -90 % in increments of 10%[101].

Murkowski et al. reported an extension of the emission wavelength to 4.6μm at 77 K[103]. The use of variable tunnel junction n-GaInAsSb/p-GaSb achieved room temperature spectra radiance 0.5 W/cm^2-sr under pulse operation (0.1% duty cycle). Meanwhile, inserting a type-I GaInAsSb/AlInAsSb MQW into the ICLED structure allowed a peak emission of 3.1 μm corresponding to an output power of 2 mW near room temperature[104]. This study reveals that increasing the number of quantum wells in each stage from one to three improves the output power by about 25%. An Interband cascade-based LED using a type-I WQW active region was reported[105]. At room temperature, the 22-stage device showed a peak wavelength emitted at 3.1 μm with an output power of 2.9 mW(0.73 W/cm^2 /sr) and maximum well plug efficacy of 0.4%. Researchers from the University of Iowa reported on the improved performance of InAs/GaSb SLS ICLED on Si and compared this with a GaSb-based ICLED[106]. As mentioned in figure 3.21, the Si-based SLS LED outperforms GaSb-based SLS LED in

the high injection regime as the device size increases. It was concluded that the difference in the thermal expansion coefficients of the silicon and III–V materials improved internal quantum efficiencies.

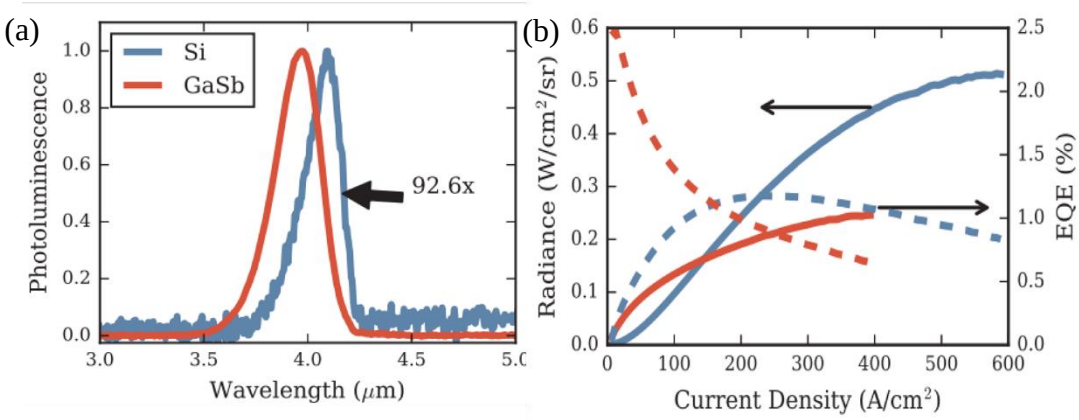

Figure 3.21: (a) A comparison of spectra resolved normalised photoluminescence from InAs/GaSb SLS ICLED grown GaSb(red colour) and Si (blue colour) substrate where the output of the Si-based ICLED increased by a factor of 92.6. (b) Radiance varying current density for 400 x 400 μ m mesa devices showing that Si-based ICLED outperformed the GaSb-based ICLED at high current density[106].

3.4 Mid-Infrared Resonance Cavity Light-Emitting Diodes (MIR-RCLEDs)

In 1994 Hadji et al[107] demonstrated the use of $Cd_{0.51}Hg_{0.49}Te$/HgTe pseudo alloy QWs in an RCLED structure to enable room-temperature operation at $\lambda = 3.2$ μm. The structure consisted of a half-wavelength cavity of $Cd_{0.75}Hg_{0.25}Te$ sandwiched between the CdZnTe substrate and n-doped CdHgTe antinode layer, as shown in figure 3.22. A DBR reflectivity of 86 % was used, while top gold mirror reflectivity was kept at 95 %. The electroluminescence measurements at room temperature showed a peak width of 8 meV while the extremal quantum efficiency of 0.2×10^{-3} %. This study concluded that the FWHM for a structure without a cavity was six times wider than a structure with a cavity. GaAs-based RCLEDs designed to operate near 4.2 at room temperature were

investigated[108]. The structure consisted of a 1xλ thick cavity including (12nm)InAs/(12nm)InAsSb(Sb9%) SLS active region between top CrAu mirror with ¬95 % reflectance and a low reflectance bottom GaAs/AlGaAs DBR. This study concluded that the output power of the RCLED device was enhanced by a factor of 2.2 compared to that of the reference LED, which is lower than the expectations based on theoretical calculations due to the phase change from the CrAu mirror and the uncertainty in the growth rate of InAs/InAsSb SLS.

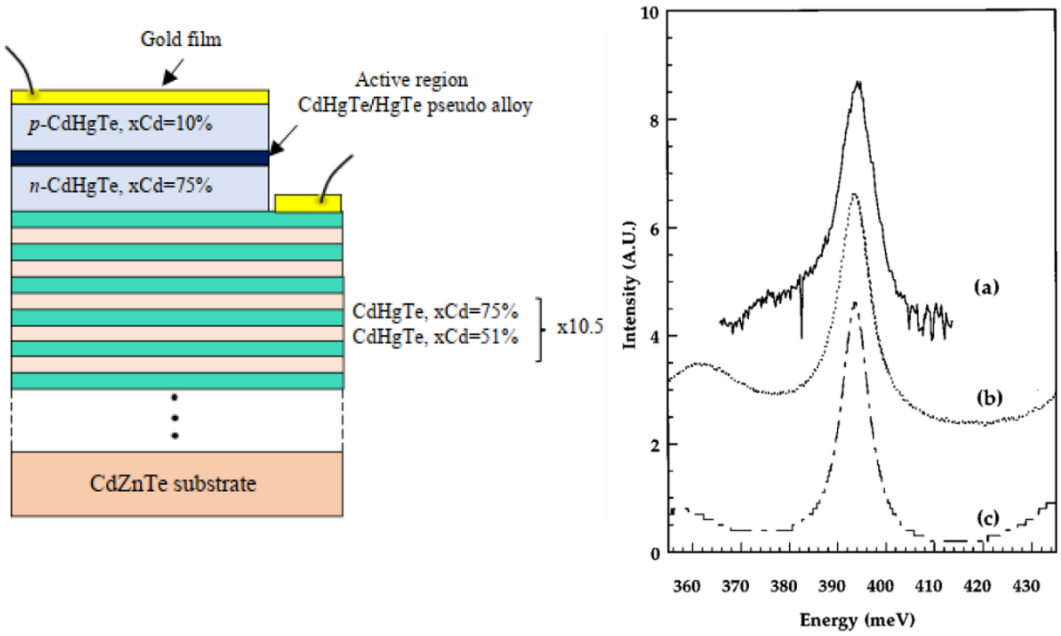

Figure 3.22: Schematic diagram of an $Cd_{0.75}Hg_{0.25}Te$ /HgTe RCLED device (left) and 300 K electroluminescence spectra (right) showing (a) the experimental EL spectra, (b) and (c) measured and theoretical cavity transmission accordingly[107,109].

Ducanchez et al. employed a GaSb substrate in an RCLED [110] and found an improvement in the performance for devices with n++ InAsSb/p++ GaSb tunnel junction TJ. The active region consists of two series of four compressively stained GaInAsSb QWs separated by AlGaAsSb barriers and placed inside the 1.5xλ-thick cavity between two AlAsSb/GaSb DBRs. Electrical characterisation showed that devices with TJ had reduced the electric resistance from 20 Ω to 8 Ω corresponding to

an enhancement of output power by a factor of 2.6 in comparison to devices without TJ, which was limited to 0.15mW. Grasse et al. [7] demonstrated two different designs based on type-II GaInAs/GaAsSb SLS and WQW active regions emitting at 2.8 µm, 3.3 µm, and 3.5 µm, grown by MOVPE on InP. Two GaInAs/GaAsSb SLS structures with thicknesses of 4.5 and 5.5 nm and alloy contents of 25 and 27 % in the GaInAs layer, and two GaInAs/GaAsSb WQW structures, also contained the GaInAs with a wall thickness of 5.5 and 4.6 nm respectively, were fabricated (see figure 3.23). The optical power was measured under CW operation with a current density of 500 A/cm^2 revealing a maximum value of 125 µW for the SLS-based RCLED and 86 µW for WQW RCLED. Among all consider designed, a 4.5nm thin SLS-based LED shows a higher e-h overlap of 47%.

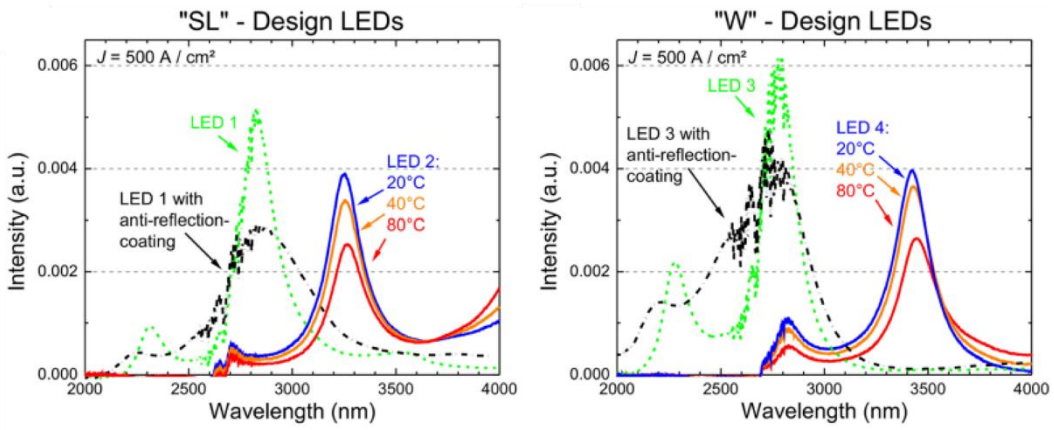

Figure 3.23: Electroluminescence spectra of type-II GaInAs/GaAsSb SLS (left) and WQW measured at a current density of 500 A/cm2 operated beyond room temperature (right) [7].

Recently, a GaSb-based RCLED was reported for emission wavelength λ =4.5 µm at room temperature[111]. The structure was fabricated by MBE on GaSb substrate at Lancaster University. Four periods of (17nm)$InAs_{0.85}Sb_{0.15}$/(6nm)$Al_{0.12}In_{0.88}As$ quantum wells followed by an AlSb EBL were positioned between two AlAsSb/GaSb DBR mirrors. It was reported that structure on RCLED exhibits (85x) higher peak

intensity, (13x) higher integrated output power, (16x) narrower spectral linewidth, and (7x) superior temperature stability compared to a reference LED without a resonant cavity, as indicated in figure 3.24.

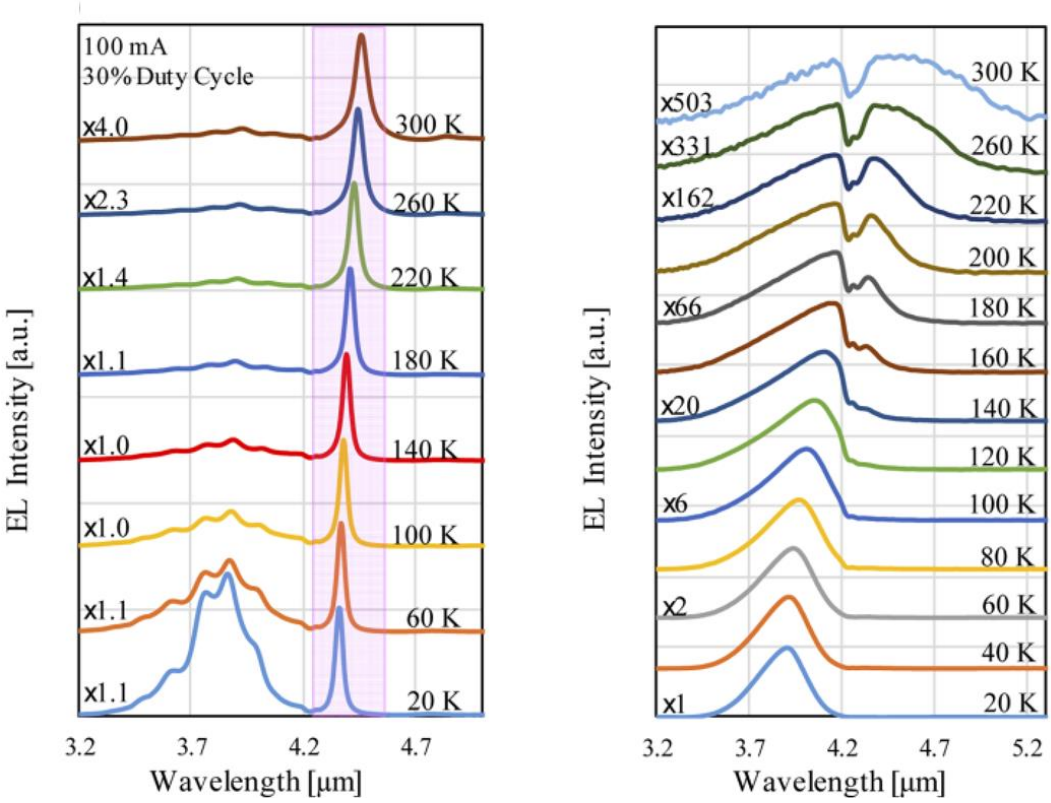

Figure 3.24: Temperature dependence of the electroluminescence emission for RCLED (left) and reference LED measured at 100 mA, 30% duty cycle and 1kHz (right)[111].

3.5 Summary

A range of device structures and concepts for gas sensing in the mid-infrared spectral range have been explored. Conventional bulk structures have advantages in terms of growth and fabrication simplicity. Although the highest output power was reported on the AlInSb-based LED structure, which showed a maximum emittance of 27 mW/cm^2 at 5.7 μm, the lack of devices to access different wavelengths was a limiting factor.

Structures based on a single quantum well benefit from the ability to adjust the alloy composition and layer thickness, enabling access to a wider range of wavelengths. Increasing the number of wells brings the possibility of improving device performance and efficiency. Various growth technology has been discussed, such as adapting the MBL layer allowing the creation of the virtual substrate filtering most of the threading dislocations, and introducing the EBL layer above the active region, which were reported to improve the performance up to a factor of 3. A type-I band alignment MQW-based LED holds benefits in terms of significant wave function overlap and strong electron confinements. Between 3.2-3.4 µm, most of the presented structures were grown on expensive GaSb substrates and their emission is limited by Auger recombination. Reports of InAsSb/AlInAs MQW-based LEDs were either based on complicated RCLED structure and using GaSb Substrates (showing emission at 4.5 µm) or have not been fabricated into LED structure. There has not been any report for this structure on Si until now. Type-II band alignment offers a reduction in the non-radiative Auger recombination process that is detrimental to device performance at high temperatures. Quantum structure engineering such as the strained-layer superlattice structure SLS allows electron tunnelling to occur. Employing type-II-based materials into SLS structures reduces the Auger rate and improves the device performance. Previous reports of LEDs with an InAs/InAsSb SLS-based active region were either made on expansive GaSb or InAs substrates or the room temperature emission was limited to 5 µm. Despite the successful growth of photoluminescence samples reported to operate at $\lambda > 8$ µm; this structure was developed for detector applications. To date, there are no reports of InAs/InAsSb SLS-based LED for an emission wavelength of 5.6 µm on cost-effective GaAs substrates. Table 3.1 show the summary of the literature review on the mid-infrared LEDs

Table 3.1: Summary of the literature reviews on the state of the art light emitting sources operating in the spectra range 2 – 7 µm.

No	Structure	1st Author	Sub.	Wavelength µm	Performance (Power, efficiency)	Comments	Year
1	InSb	Ashley et al	InSb	5.5 - 5.8	740 nW, EQE $1.7x10^{-5}$	Bulk LED AlInSb as EBL (Al = 17 %)	1994
2	GaInAsSb/ InAs	Stony Brook et al	GaSb	(3-3.6) and 2.3	1.3 W/cm^2 (7A) and 1.4W	Type-I WQW laser AlGaInAsSb EBL	2002
3	InAlGaAsSb/ GaSb	Shterengas et al	GaSb	2.5 - 2.82	0.001- 1 W	Type-I MQW laser Thermal leakage of the hole is the response to decreasing the IQE	2004
4	AlInSb/InSb	Nash et al	GaAs	3.81, 6.39 (bulk) 5.25 , 5.43 (SQW)	4, 7 mW/cm^2 (bulk) 3, 5 mW/cm^2 (SQW)	QW1 40 nm (Al = 7.7 %) QW2 20 nm (Al = 14.3 %)	2006
5	AlInSb	Haigh et al	GaAs	3.4 - 5.7	3.4 mW/cm^2 27 mW/cm^2	Bulk LED 5 devices (Al = 0 - 8.8 %)	2007
6	InAs/InAsSb	Aziz et al	GaAs	3.5 – 4.18	-	Multi spectra LEDs	2017
7	GaInAsSb/Al InAsSb	Ermolaev et al	GaSb	3.1 (290 K)	2 mW (290K)	Cascade LED 10 stage	2018
8	AlInAs/ InAsSb	Al-Saymari et al	GaSb	4.5	2.5 mW/cm^2 10 mW/cm^2	Type-I MQW RCLED	2020

Chapter 4: Experimental procedures

In this chapter, the experimental methods that were used to simulate, grow, fabricate, and characterize III-V semiconductor LED devices are discussed.

4.1 Molecular Beam Epitaxy (MBE)

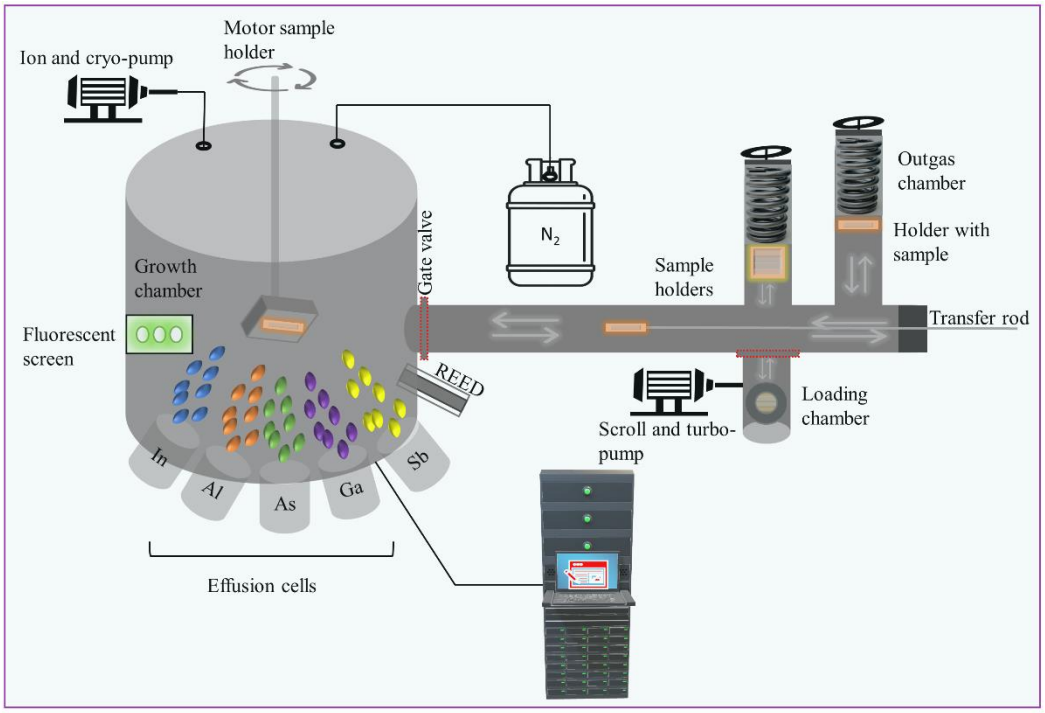

Figure 4.1: Simplified schematic of a typical MBE system used in this work.

Molecular Beam Epitaxy is the state of the art tool used to grow high-quality semiconductor materials under ultra-high vacuum (UHV). The slow growth rate in the order of 1 ML/s offers precise control of layer thickness and abrupt interfaces necessary when growing quantum structures such as quantum well and superlattice. The samples in this work were produced using the Veeco GENxplor MBE system in the Physics department at Lancaster University. Figure 4.1 shows a simplified schematic of the

MBE system with essential components are labelled. The system consists of three chambers, the loading chamber, the prep chamber and the growth chamber. A backing pump and turbopump maintain UHV where the background pressure is reduced to 10^-10 mbar. The wafers were placed into the loading chamber and heated at 200^{o} C to remove water vapour and absorbed gases. Next, the wafer is transferred to outgas chamber for additional thermal degas up to 350 C.. Once the sample is ready for growth, it is mounted securely onto the meniplelats holder and moved using the transfer arm into the UHV growth chamber. The sample is placed at a rotating holder to ensure uniform deposition of desirable materials. Prior to the growth, the deoxidizations process, which involves heating the sample, is carried out to ensure removal of native oxide. Inside the UHV growth chamber, effusion cells are located at the bottom and aligned towards the chamber's centre, where a sample holder is located. The thermal effusion cell k-cells are used to provide the flux of the group III elements indium (In), gallium (Ga), aluminium (Al) and the dopant materials beryllium (p-type) and GaTe (n-type). In addition, the cracker cells are used to provide the flux of the group V elements, arsenic (As) and antimony (Sb). Each Individual k-cell contains a specific element in ultra-pure solid form. The growth process starts by heating the k-cells until the source materials reach a set point. The shutters are opened, and then vapour from each k-cell diffuses through the chamber until it is deposited on the substrate. For uniform growth, the substrate kept rotating at a constant speed of ~ 10 rpm using a stepper motor attached to the top of the growth chamber. During growth, in-situ reflection high energy electron diffraction (RHEED) was used to monitor the crystal layers. In this technique, an electron gun located at the side of the UHV growth chamber produces a beam of high-energy electrons incident at an angle < 2^{o} on the sample surface, then reflected on the fluorescent screen, forming a visible diffraction

pattern. A streaky pattern indicates good crystallinity and smooth layers whilst a spotty pattern indicates 3D or metamorphic growth[112]. The intensity of the observed pattern depends on surface roughness, i.e. the more intense the RHEED pattern is, the smooth surface being grown.

4.2 X-ray diffraction (XRD)

X-ray diffraction is a powerful non-destructive technique used to study the crystal. Helpful information can be extracted, such as the lattice constant, material composition, strain, and SLS layer thickness. These characterizations rely on the effect of X-ray photons being coherently scattered off the crystal via Bragg diffraction (the scattered photon has the same energy as the incident photon):

$$n\lambda = 2d \sin(\theta_b) \qquad (4.1)$$

The term n is an integer (order of reflection), λ is the emission wavelength of the X-rays, d is the lattice plane spacing, and θ_b is the Bragg angle (the angle between the incident x-ray and the normal to the reflecting lattice plane) which is dependent on the material. In this work, the D8 Discover X-ray diffractometer (HRXRD) system from Bruker was used to characterize all samples. A schematic diagram shows the setup of the HRXRD scanning system as indicated in figure 4.2.

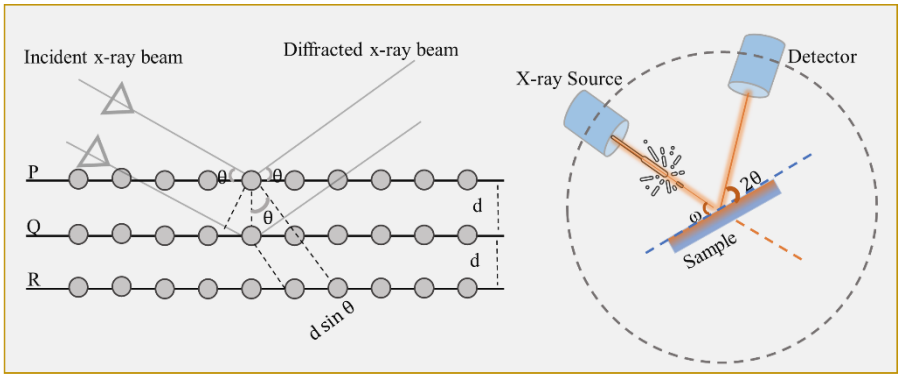

Figure 4.2 : (a) illustration of Bragg's law. (b) schematic diagram showing the setup of the HRXRD scanning system used to measure X-ray diffraction from the sample.

The sample is placed onto the vacuum stage connected to the pump and allows the sample to be held vertically. A hot filament acts as an electron source producing a high-energy beam with a wavelength of 1.54 Å. The incident x-ray beam hits the sample, which rotates at an angle of θ, and the beam is then scattered from the sample, and detected by the detector. For a symmetric scan, it is moved at an angle of 2Θ. The result movements of the sample and the detector forming ω-2Θ scan producing diffraction spectra which analysed using RADS Mercury software.

4.3 Photoluminescent (PL)

Photoluminescence is a non -destructive technique used to study the optical properties of materials such as the energy band structure. In this work, a 785 nm red laser acts as an excitation source emitted onto the sample's surface. The red laser operated at 100 mA, 1 kHz and 50 % duty cycle corresponding to an excitation power of 2.5 W/cm^{-2} at the sample surface. The sample was first placed inside the inner chamber of the Oxford instrument cryostat, which can be cooled to low temperature (4 K) using a continuous flow of liquid helium and a temperature controller unit. Priority to PL measurement, the path of the laser beam and emission of the sample should be carefully aligned to maximize the PL Signal. This could be achieved by ensuring the sample holder arm is positioned at an angle of 45 degrees to the line of the laser beam. As the laser beam hits the angled sample surface, the photoluminescence emitted from the sample along with the reflected beam exited through the CF_2 window of the cryostat as demonstrated in figure 4.3. The reflected beams pass through a concave lens placed between the cryostat

and the FITR spectrometer. The laser diode is focused with a concave lens adjustable in three dimensions (x,y,z), allowing a maximum signal received into the FTIR system. In the case of power-dependent measurements, filter wheels containing different neutral density filters are positioned in the laser beam path before it reaches the cryostat, lowering laser excitation power to 1 %. To prepare the cryostat, the outer chamber valve of the cryostat is closed while the inner chamber valve is kept open. Next, helium flow is introduced to purge the air for about 2 minutes. The sample holder arm is quickly fixed, and the chamber is sealed from the outside atmosphere. Now, a small amount of helium is travelling through the pipe to the inner chamber, and the valve is closed, then the chamber is pumped, resulting in a reduction of the pressure to 10^{-1}mbar. This process should be repeated three times until pressure reaches 10^{-2} mbar. Once this is done, a final helium flow is introduced to the inner chamber and remains inside to allow temperature exchange to low temperature. Finlay, the outer chamber valve is opened and remains under vacuum until the pressure achieves 10^{-2} mbar. The system is then ready to begin the cool-down process. This includes the use of liquid helium, which flows through a transfer pipe and is confined in the space between the chambers to allow heat exchange. The temperature control unit allows the sample to reach the desired setpoint. Then, the sample's resulting PL emission was analysed using Bruker Vertex 70 Fourier Transform Infrared (FTIR) spectrometer at a resolution of 4 cm^{-1}. The resulted PL emission was detected by either 77 K InSb or MCT photodetector. Next, the computer processed the signal via the Stanford SR830 DSP lock-in amplifier. Bruker OPUS software running on the computer converts signals from the FTIR system into a spectrum of intensity over wavenumber corresponding to the photoluminescence emitted by the sample.

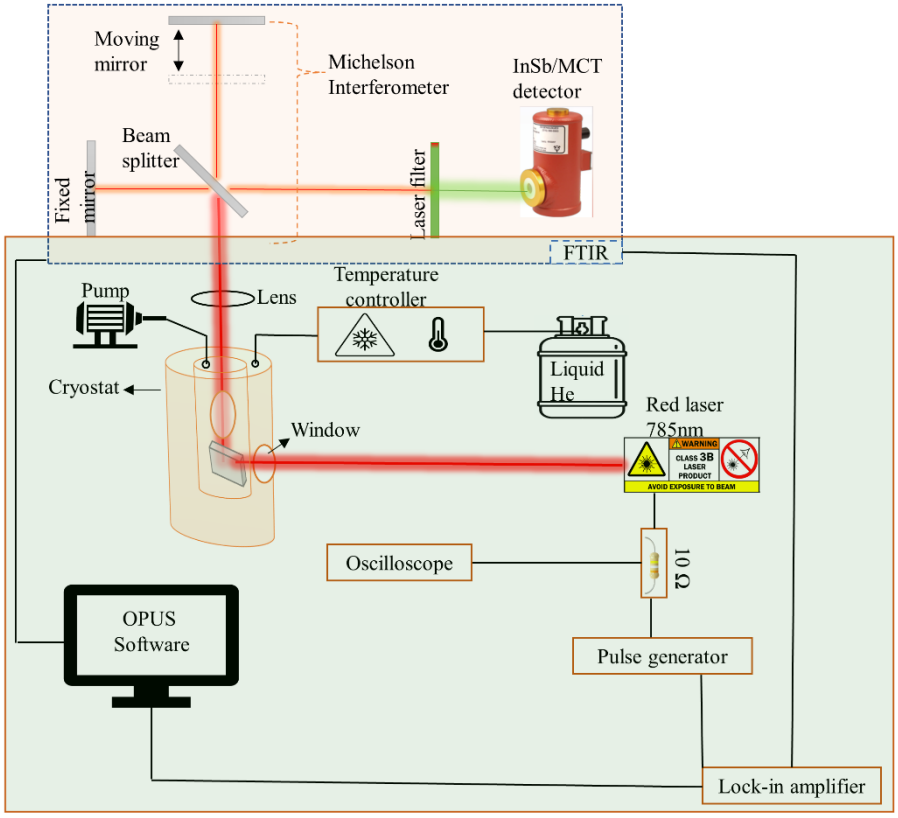

Figure 4.3: Schematic diagram of the FTIR photoluminescence system. The glowing red line represents the path of the laser beam and the green dashed line is infrared photoluminescence from the sample detected by either InSb or MCT detector.

4.4 Device processing:

1. [sample preparation] The result grown sample needs to be deep cleaned to remove any surface contamination, as indicated in figure 4.4. The sample was immersed in acetone solution and placed in the ultrasonic bath for about 4 minutes, followed by a rinse of acetone. This process was repeated with a bath of isopropyl alcohol. After that, the sample was dried with nitrogen gas to dry the sample.
2. [top p-contact] Once cleaning is done, a photoresist layer is applied to the sample surface using the spin coating method. A few drops of LOR3A lift-off

resist is applied on the sample surface and spun at 3000 rpm for 30 seconds (350 nm thick), which is then baked with a hotplate at 180 C for 5 minutes. A second photoresist layer, S1813 was deposited on the sample surface and spun at 4000 rpm for 1 minute. After that, the sample was placed on a hotplate and baked at 120 C for 2 minutes producing a 1 µm thick layer. Once the sample cooled to room temperature, a Suss Microtec MJB4 mask aligner equipped with a 260 W ultraviolet (UV) lamp and a quartz mask was used to expose the photoresist layer. The sample was exposed to UV light for about 2.5 seconds. The exposed area of the photoresist layers was removed by immersing the sample in Microposit MF-SD-26 developer for 80 seconds, followed by rinsing with deionized water and then blown dry using nitrogen gas.

3. [contact metallization] Next, a Moorfield thermal evaporate is used for metallization. The sample is placed on an aluminium plate and secured using Kapton tape. The plate was placed into the evaporating chamber. The metals (Au wire and Ti pellets) were cleaned with acetone, and IPA was then placed back into its respective coils. To prevent oxidation, the pressure inside the chamber is kept in order of 10^{-6} mbar. The Ti coil is heated by slowly increasing the currents to 50-60 A. The material deposition can be started by opening the shutter, resulting in 20 nm of Ti layer thickness. The shutter is closed, then the current decreases to 0 A and the Au heating process were begun. This involves increasing current to 27 A and using a deposition rate of 3 A/s, achieving a thickness of 150 nm. The shutter of the sample was closed and the current reached 0 A. Following this, the sample was rinsed in acetone and IPA to remove residue of the photoresist and achieve lift-off.

4. [etching preparation] Before the wet etching process, the mesa areas on the sample surface should be protected. S1813 photoresist was deposited on the sample surface and uniformly distributed on the surface using the spin coating method followed by baking the sample at 120 C for 2 minutes. The sample surface was exposed to UV light using a mask aligner and then immersed in the developer followed by rinsing with deionized water and then dried with nitrogen gas.
5. [mesa etching] To produce a *p-i-n* heterojunction device, the upper layers should be etched, through the active region, down to the lower contact area of the sample. This can be achieved by using a dilute ammonia-based etchant at a 300 nm/min rate for the GaSb layer and a mixer of citric acid and hydrogen peroxide solution for the InAsSb layer. In addition, Sulphuric acid/hydrogen peroxide/deionized water was used for etching AlInAs/InAsSb QWs at a rate of ~400 nm/min. Throughout the etching process, a surface profiler was used to ensure that each layer was etched to the correct depth. Following this, the sample was immersed in Microposit 1165 remover until the photoresist was removed, followed by rinsing with ionized water and sample cleaning with acetone/IPA and blown dry with compressed nitrogen gas.
6. [bottom n-contact] The second course of lithography was carried out, including the usage of bi-photoresist(LOR3A and S1813) and spin coating method followed by UV light exposure. The sample was then soaked in the developer to remove the exposed part of the photoresist followed by rinsing with deionized water and cleaning with acetone and IPA. The parameters for spin coating and mask aligner, such as baking temperature and the exposure time, were similar to the p-contact step (step no.2).

7. [Thermal evaporator] The process of depositing Au/Ti metallic contact on the sample surface was similar to step no 3 resulting in leaving metal only on the n-contact layer. The excess metal and photoresist coating was lift-off with remover, followed by a sample cleaning with acetone/IPA and blown dry with nitrogen gas.
8. [Wire boding]: In this step, the fabricated sample was divided into small devices, and Silver (Ag) conduction paste was placed on top of TO 64 headers. The wire bonder Accelonix TPT HB05 with 25 um thick gold was used to complete the upper top (p-type) and lower top(n-type) contacts.

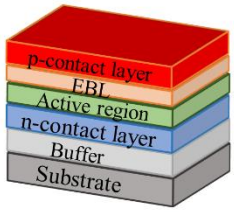

(1) Sample preparation

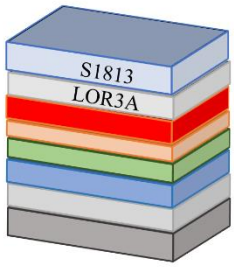

(2) Bi-layer of photoresist applied followed by spinning and baking

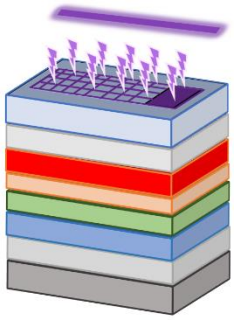

(3) UV-light exposer via desired mask pattern

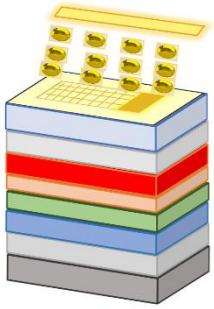

(4) Gold is thermally evaporated onto sample

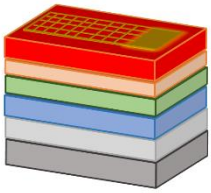

(5) Photoresist lift-off

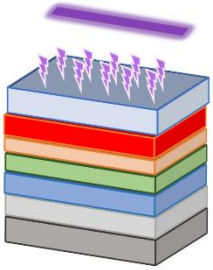

(6) S1813 applied followed by U-light exposure through mesa mask

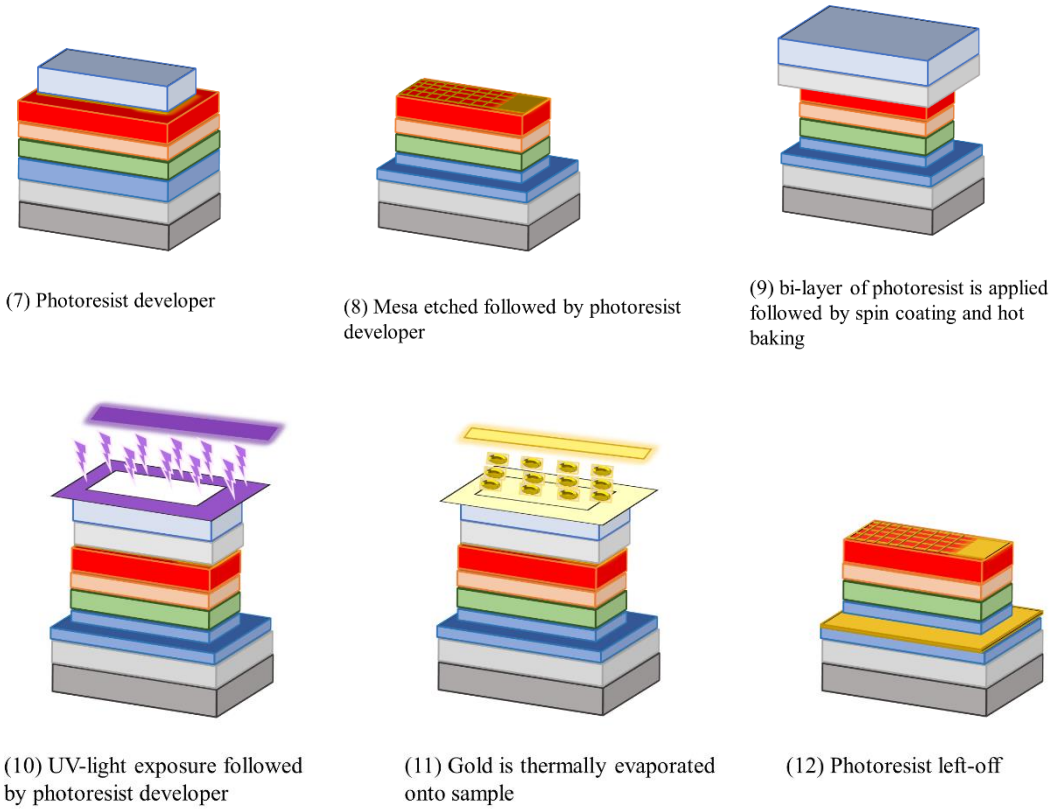

Figure 4.4: Schematic of LED fabrication process consisting of (1) sample preparation, (2) bit-layer of photoresist, (3) a first lithography step allowing to create p-type pattern (4) thermal evaporation, (5) photoresist lift-off, (6) and (7) preparing for etching, (8) etching the p-type layer through the active region and stop within n-type layer. (9) preparing for the second lithography process, (10) and (11) a second lithography process followed by n-type metallization, and (12) removing the photoresist followed by wire bonding.

4.5 Electroluminescence (EL)

Electroluminescence measurements were performed using the same FTIR system used for PL measurements, excluding the laser source. Instead, a pulse generator (Agilent B114A) and oscilloscope are connected via a series resistor (10 Ω) with the device used to monitor the current flowing through the LED. The schematic diagram showing the setup of the Electroluminescence spectroscopy measurement is shown in figure 4.5

The electroluminescence emission spectra of the LED devices were measured over the temperature range from 4 K to 300 K and at various currents and duty cycles.

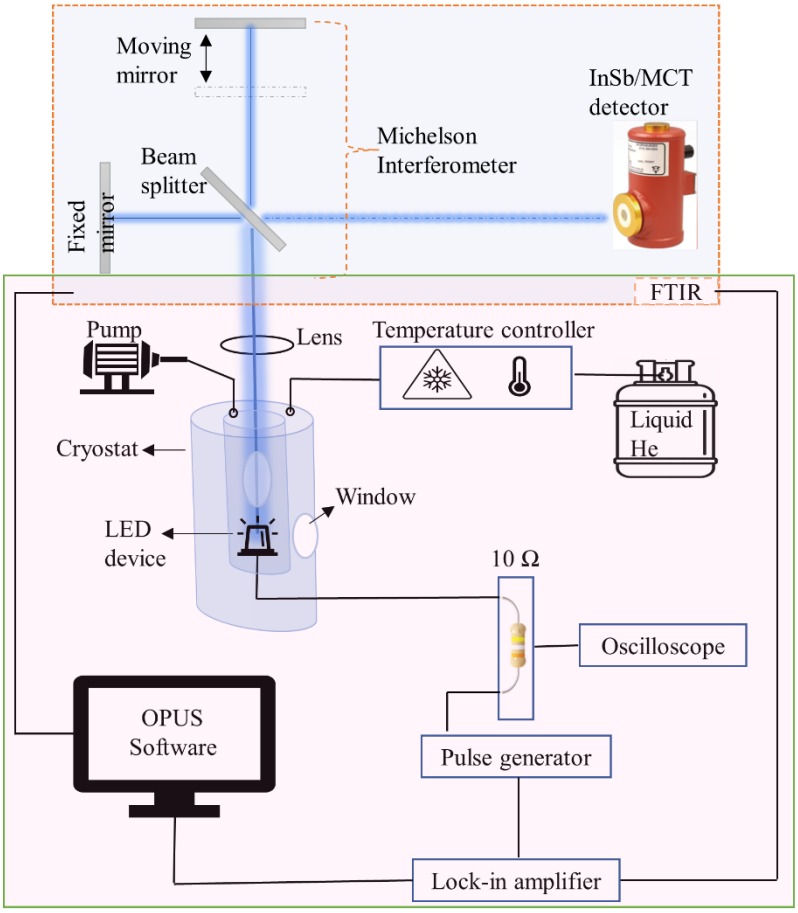

Figure 4.5: Schematic diagram of the FTIR electroluminescence system. The glow blue line represents the electroluminescence emission of the device.

4.6 Current-voltage(I-V) experimental setup

Current-voltage characterization of LED devices is collected using a Keithley 2400-LV SourceMeter, controlled by the computer, as illustrated in figure 4.6. LabView software allows LED devices to be tested in small Voltage steps and record the corresponding current. A maximum current of 100 mA was used to avoid damage to the device. In low-temperature measurements, the bonded LEDs device is placed inside the inner

chambers of the cryostat and cooled with liquid helium. A temperature controller unit was used to stabilize the corresponding I-V measured over temperature 4 – 300 K.

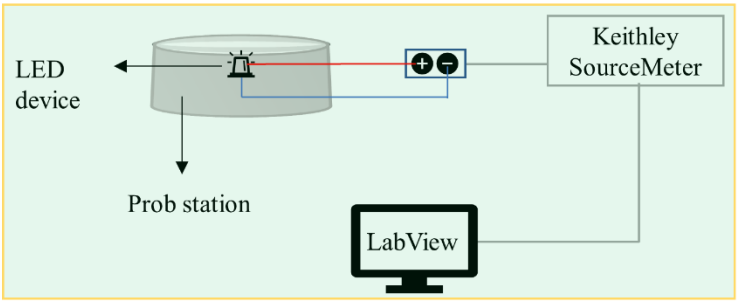

Figure 4.6: Experimental setup for I-V measurements at room temperature.

4.7 Light output power measurements

A pulse generator drove an LED device with a frequency of 1 kHz and pulse width of 1% duty cycle at variable current. The output power from the LED at room temperature was measured using a gold-coated integrating sphere (Newport instrument 819C and PdSe photodetector). The LED device was placed (see figure 4.7 (a)) at the zero-degree port of the integrated sphere, and the detector was mounted on the 90-degree port. As a current pass-through device, the light output scatters inside the sphere, which allows the detector to see a uniform constant fraction of total light output. The output power was measured on later devices using Thorlabs power meter PM100D apparatus. This includes a handheld digital power meter console and S180C MCT (HgCdTe) photodiode. The power meter spectra response differs depending on the wavelength being measured. To obtain accurate measurements, it is essential to set the PM100D to the wavelength of the device being measured. The LED devices were first calibrated then the corresponding mean value of output power is recorded as illustrated in figure 4.6 (b).

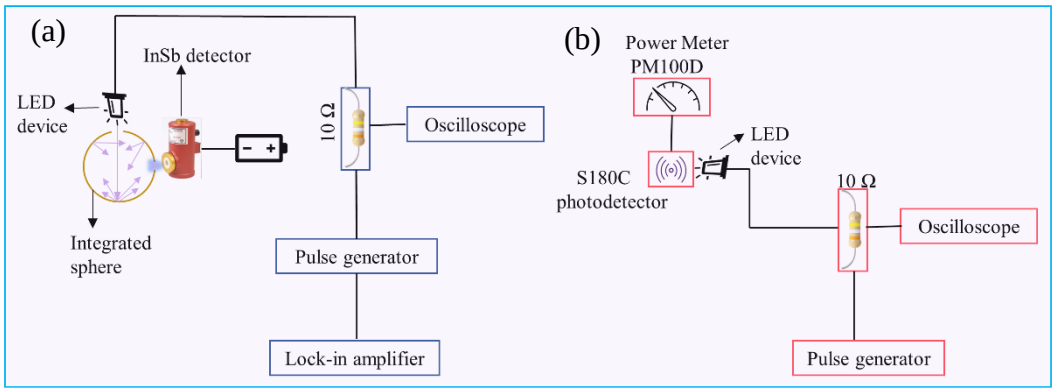

Figure 4.7: The light output measured using (a) Integrated sphere measurements at room temperature for InAsSb/AlInAs MQW LED devices and (b) power meter setup for InAs/InAsSb SLS LED devices.

4.8 FTIR and XRD spectroscopy analysis:

Deconvolution of a composite peak into induvial peaks is vital to the physical interpretation of any spectrum or diffraction pattern, including XRD and FTIR spectra. Helpful information from the data file could be extracted, such as Intensity, peak position, and linewidth, which can be used to understand the optical properties of III-V semiconductor material. OriginPro 2019b was used to analyse the data file using the peak analyser tools in this work. The Gaussian fitting function can be expressed according to :

$$y = y_o + \frac{Ae^{\frac{-4\ln(2)(x-x_c)^2}{FWHM^2}}}{FWHM\sqrt{\frac{\pi}{4ln(2)}}} \qquad (4.2)$$

The parameters y_o represent the baseline, x_c is the centre of the peak, A is the integrated area, and $FWHM$ is the full width at half maximum. Using the peak analyser tool, Gaussian deconvolution of the FTIR spectra for all samples was carried out.

Corresponding values of intensity, integrated intensity, and peak position of the PL/EL spectra were recorded, carefully understood, and compared to the literatures discussed in the result chapters.

4.9 Nextnano Simulation:

Computer modelling of semiconductor quantum structures is required to support experimental work such as electronic band structure and optical properties for analysing measured data and designing a new quantum structure. This was achieved using Nextnano simulation software® by providing a solution of the Schrodinger, Poisson and current equations. The carriers are treated within the effective mass approximation to find the quantization energies. The dependence of band offsets relies on a materials database populated mainly from the work of Vurgaftman[42]on the band parameters of III – V materials. The program consists of a coding script written by the user specifying the geometry and materials of the heterostructure. The program flows can be summarized as follows[113]. First, calculate the layers' strain because heterostructure is made of semiconductor materials with different lattice constants. Then, the calculation of the piezoelectric (electric charges building up within the materials) and pyroelectric charges (the ability of the materials to generate an electric potential due to temperature variation). Following that is the determination of the band structure and corresponding energy of the eigenstate of electron and hole using either a single-band or eight k. p envelope function approximation. Next, solve Schrödinger, Poisson, and current equations self-consistently. Subsequently, band structure, electron/hole transition, and optical matrix elements can be determined, revealing valuable information about the structure. An example of a simulation code used to model InAsSb/AlInAs MQW structure is presented in Appendix A.

Chapter 5: Mid-infrared type-I InAsSb/AlInAs multi-quantum well light-emitting diodes grown on GaAs and Si substrates.

5.1 Introduction

Development of mid-infrared III-V semiconductors LEDs on mature substrates such as GaAs and Silicon (Si) is increasingly being demonstrated, benefiting from the pre-existing manufacturing technology, the availability of large-size wafers and lower fabrication costs. The type-I InAsSb/AlInAs MQW system offer ability to engineer compressively strained QWs, which demonstrates a type-I band alignment with strong electron/hole wavefunction overlap leading to a high radiative recombination rate[27]. In this chapter, the design of light-emitting diodes operated at 3.3μm is demonstrated. Based on that, two electroluminescent samples were successfully grown on metamorphic GaAs and Si substrates using the MBE system. This follows by studying surface morphology using various methods such as x-ray and atomic force microscopy. The temperature and power dependency of photoluminescence spectra of both samples are considered. Electroluminescence characterisation and power-dependent measurements, as well as exploring the I-V behaviour in both devices, are demonstrated.

5.2 Design and growth type-I InAsSb/AlInAs MQW LEDs

5.2.1 Band structure calculation

Theoretical modelling was undertaken with Nextnano simulation software. The calculation of band structure, as well as energy levels of electron and hole states, are based on single-band effective mass approximation. The material parameters used in

analyses were those recommended by Vurgaftman[42], except for the bowing parameters for the bandgap E_g and Δ_{SO} spin-orbit splitting energy of $InAs_{1-x}Sb_x$. According to Cripps et al. [114] bowing to spin-orbit splitting, energy is neglected. Taking Vegard's Law into account equation 2.4, a non-zero bowing parameter between conduction band CB and valence band VB edge as well as a 40:60 splitting ratio between bowings that contribute to the overall bandgap is realised as suggested by Liu [115] CB and VB energies' bowing parameter was selected as CB = +0.65 and VB = -0.98, showing a good agreement with experimental work. In addition, all other parameters are interpolated linearly between those of the two binary compounds, InAs/InSb in the $InAs_{1-x}Sb_x$ and AlAs/InAs in the $Al_yIn_{1-y}As$.

Figure 5.1(a) shows the 4 K predicted emission energies of $InAs_{1-x}Sb_x$/ $Al_{0.122}In_{0.878}$ As from electron to lowest confined heavy hole state as a function of Sb composition. During simulation, the lattice parameter of the virtual substrate ($Al_yIn_{1-y}As$) was taken as a reference. To justify the alloy content in the AlInAs barrier (Al = 12.2 %), a simulation of the MQW structure indicates that reducing the Al content will lessen the confinement energy of electrons. For instant, using (Al = 5 %) results in shallow confinement (Δ_{CB} = 11meV), and thus electron needs low energy of five meV to escape from the well. Conversely, increasing the Al in barrier to ~ 30 % will significantly increase the band offset of CB (Δ_{CB} = 385 meV), and the electron would strongly localise in the well (E_{loc} =285 meV). However, a 30 % Al in the barrier is associated with a risk of sizeable compressive strain being significantly increased (i.e. the in-plane strain ($\varepsilon_{xx} \approx 2.8$ %). Therefore, desirable Al content of 12% in buffer and the barrier layers have been considered. Additionally, increasing the Sb contents in the10 nm well from 5 % to 13 % increase the transition energy by a factor of 1.17 ($\Delta E_{e\text{-}hh1}$ = 67 meV). Figure 5.1 (b) shows the confinement energy as a function of Sb and corresponding

compressive strain. For instant, at Sb = 5%, the calculated band offset of the conduction band ΔE_{CB} and the valence band edge ΔE_{VB} are 146 and 130 meV, respectively. As Sb contents increase, there is a strong reduction in the ΔE_{CB} (from 146 ± 0.1 meV at Sb = 5% to 65 ± 0.1 meV at Sb = 13%) due to the upward shift of the energy level of $InAs_{1-x}Sb_x$ CB caused by increasing the compressive strain. Conversely, ΔE_{VB} is found to be increasing with increasing Sb ($\Delta E_{VB} \sim \alpha$ Sb). Based on these results, electron confinement would substantially degrade for Sb ≥ 13%, corresponding to the emission wavelength of λ= 3.3 µm. Based on this, type-I band offsets can be realised for λ < 3.3 µm (4 K) and ensure high electron-hole spatial overlap in $InAs_{0.915}Sb_{0.085}$ /$Al_{0.125}In_{0.875}As$. Figure 5.2 shows that the sample's calculated band structure that has been considered in this work reveals a large band offset of 107 (ΔE_{CB}) and 188 meV (ΔE_{VB}). The calculated transition energy is in good agreement with PL emission observed at 4 K. The activation energies for carriers to escape are estimated to be 111 and 181 meV for electrons and holes accordingly.

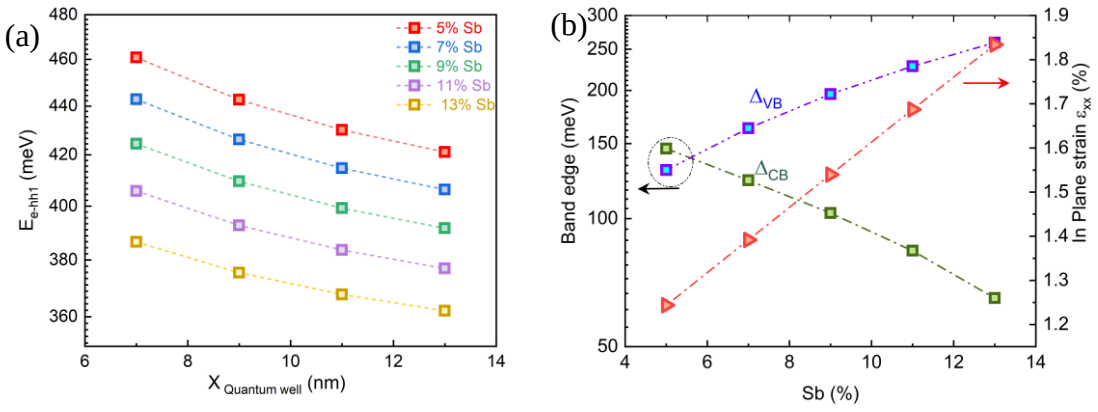

Figure 5.1: (a)Calculated ground state transition energy (e-hh1) as a function of the well thickness for various Sb compositions and (b) the band offset of conduction band ΔE_{CB} and valence band ΔE_{VB} confinement energy with corresponding in-plane strain ε_{xx} for different Sb composition.

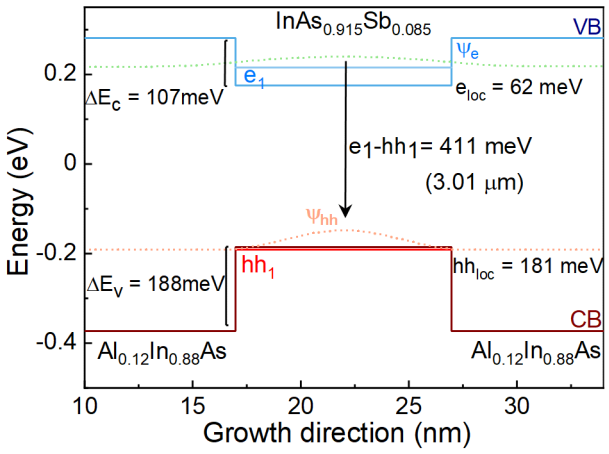

Figure 5.2: Band structure calculation of $InAs_{0.915}Sb_{0.085}$ /$Al_{0.125}In_{0.875}As$ QW showing the large electron and hole confinement energy along with predicted peak e-hh1 emission energy.

5.2.2 Growth of Type-I InAsSb/AlInAs MQW on GaAs and Si substrates

The samples were grown using a solid source Veeco GENxplor Molecular Beam Epitaxy (MBE) system. All sample studied in this chapter was grown by Dr. Laura Hanks. Valved cracker cells were used to provide arsenic (As), and antimony (Sb) fluxes and SUMO® cells are used to provide the In, Ga and Al-fluxes. During growth, the surface reconstruction was monitored using reflection high energy electron diffraction (RHEED).

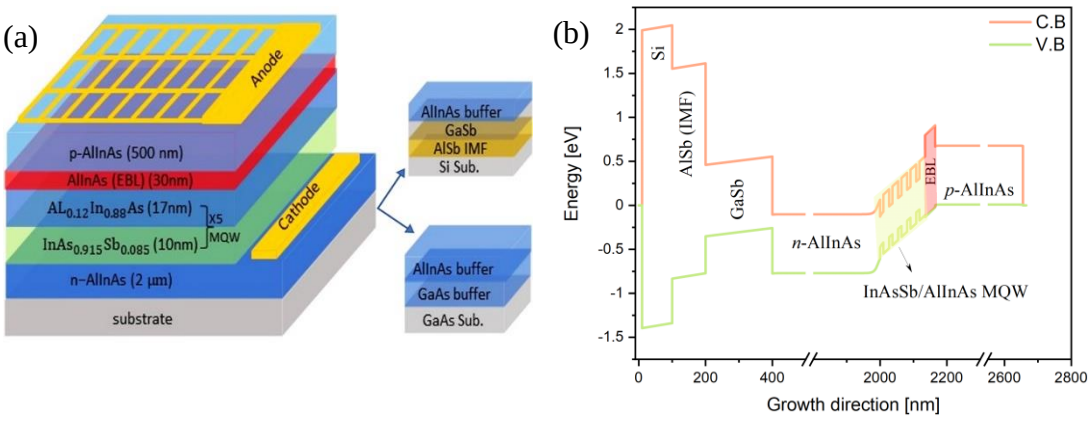

Figure 5.3: (a) A schematic diagram of the GaAs and Si-based LEDs structure showing the details of InAsSb/AlInAs MQW active region alongside (b) the energy band diagram of the EL structure obtained using Nextnano.

Two LEDs structures were grown using a 2µm-thick n-type $Al_{0.12}In_{0.88}As$ buffer layer, one on a 4 deg offcut toward [0-11] Si and one on a GaAs substrate, as shown in figure 5.3 (a). The growth of a high crystalline quality AlInAs buffer layer faces difficulties related to the large lattice mismatch to the wafers leading to the generation of misfit defects and threading dislocations. Furthermore, the significant difference between the Al and In sticking coefficients leads to segregation and intermixing. Therefore, an optimised growth technique was used to grow the AlInAs buffer layer for each sample. For the GaAs-based structure, the growth temperature was reduced to 475˚C under an As flux following the growth of the GaAs buffer layer. The AlInAs buffer was deposited using a V/III flux ratio of 9 and a growth rate of 1µm/hr. Interfacial misfit (IMF) arrays of misfit dislocations were generated at the InAlAs/GaAs interface to help release the misfit strain leading to a dislocation density of ~ $1\times10^{9}cm^{-2}$. For the Si-based structure, a GaSb intermediate buffer layer was used between the Si and AlInAs buffer. This was grown using an AlSb IMF array and a two-step growth temperature technique (490 to 545 ˚C) to provide an antiphase domain (APD) free epilayer on Si with a smooth surface. Details of the Si wafer cleaning technique, the growth of the GaSb buffer layer and the surface characterization have been described previously[74]. Next, the growth temperature was reduced to 475˚C under an Sb flux, and a monolayer of Al was deposited on the GaSb buffer. AlInAs was then grown following the procedure described previously. Even though the surface dislocation density on the GaSb/Si buffer was expected to be low (~$10^{8}cm^{-2}$), the tensile strain at the InAlAs/GaSb interface was not successfully accommodated, resulting in a high dislocation density of the order of ~ $1\times10^{10}cm^{-2}$ based on extensive study of GaSb buffer on Si. Next, the same active region was deposited on top of each buffer structure grown comprising five periods of $InAs_{1-x}Sb_x/Al_xIn_{1-x}As$ MQWs with an Sb content of 8.5% in the InAsSb layers. The

thickness of the $InAs_{0.91}Sb_{0.085}$ QWs and $Al_{0.12}In_{0.88}As$ barriers were 10 nm and 17 nm, respectively. An optimized shutter sequence consisting of 10 seconds of As flux prior and 180 seconds following the growth of the InAsSb QW were used to reduce the Sb and Al atoms segregation and improve the interface abruptness. The active region was grown using a growth temperature of 440 ˚C. The QWs were designed to exhibit a peak emission near $\lambda = 3.3\,\mu m$ at room temperature. Finally, an undoped 30nm $Al_{0.24}In_{0.76}As$ electron blocking barrier (EBL) was grown on the top of the active region and a 500nm-thick p-type $Al_{0.12}In_{0.88}As$ (Be doped = 1 $x10^{18}$ cm^{-3}) capping layer was deposited to finalise the structures. Figure 5.3 (b) shows the energy band diagram of the Si-based LED structure. As seen from this figure, EBL has been considered to improve the electron's confinements energy and enhance the optical properties.

5.3 Structural characterisation of InAsSb/AlInAs MQW LEDs

After growth, the quality of crystalline materials was investigated with High-Resolution X-ray Diffraction HRXRD and Atomic Force Microscopy AFM, which will be discussed below.

5.3.1 High-resolution x-ray diffraction

The X-ray diffraction ω-2θ rocking curves obtained for the two InAsSb/AlInAs MQW LED samples are shown in figure 5.4. RADS Mercury simulation software was used to determine the thickness of the layers and Sb content. The thickness of the InAsSb QWs and the AlInAs barriers were found equal to 10 and 17 nm, respectively. The Sb content in the wells was determined to be 8.5 %, while the Al content in the barrier layers for both samples was 12.2%.

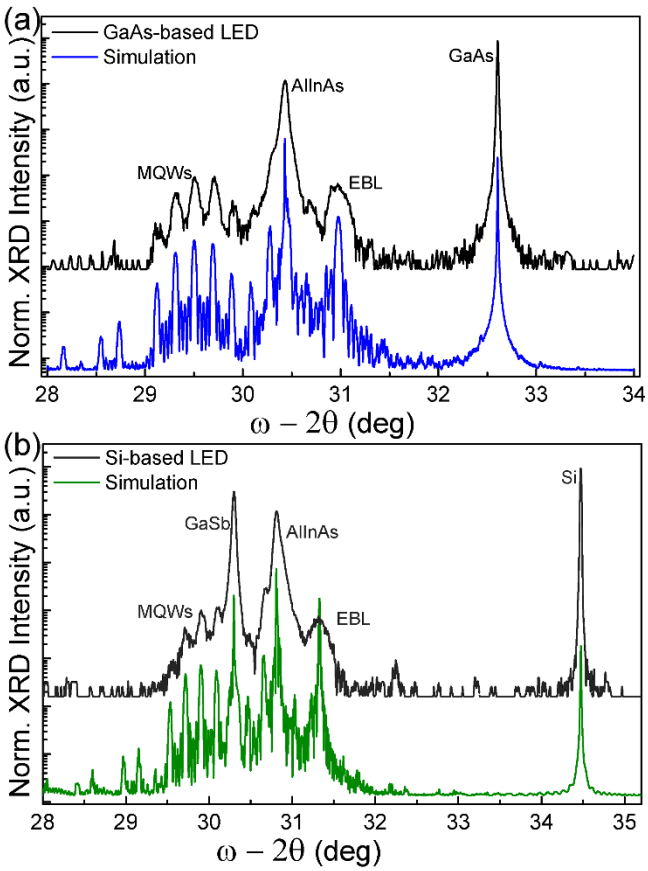

Figure 5.4:A coupled (ω-2Θ) scan of (a) GaAs and (b) Si sample along with the corresponding simulation of the structure. The strong intensity of the MQW on GaAs compared to that on Si samples indicates the grown material quality.

These results are in good agreement with the targeted QWs structure characteristics required to obtain emission at ~3.3 µm. The full width at half maximum (FWHM) acquired for the AlInAs buffer layer was similar for both samples and roughly equal to162 arcsec. However, the peak position of the AlInAs buffer was observed at 30.84 deg (GaAs) and slightly increased to 30.90 deg (Si) due to increasing the compressive strain. This shift in the buffer is more likely to shift the satellite peaks of MQWs observed in the Si sample.

5.3.2 Atomic force microscopy

Atomic force microscopy scans sample surfaces down to the nanometer scale. The feature of the surface is a good indication of material quality. A desirable smooth surface is usually $\sim 2\ A^o$. Figure 5.5 shows a 2µm x 2 µm AFM scan of MBE growth of GaAs and Silicon samples.

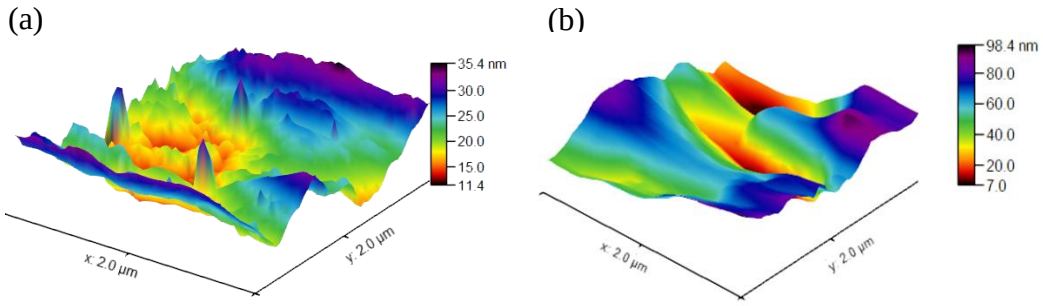

Figure 5.5: AFM image for the (a) GaAs and (b) Si sample of MBE growth.

The average root means square R_{sq} of the GaAs sample is 6.16 ± 0.40 nm which is five times lower than that of the Si sample 20.80 ± 0.60 nm. The considerable R_{sq} value of the Si sample indicates a rougher surface which may be attributed to (threading dislocations) the high strain of the epilayer.

5.4 Photoluminescence comparison of InAsSb/AlInAs MQWs on GaAs and Si

5.4.1 Excitation in 4 K PL with varying excitation power

The normalised 4 K photoluminescence of undoped $InAs_{0.915}Sb_{0.085}$ /$Al_{0.125}In_{0.875}As$ MQW grown on GaAs and Si substrates were obtained using the low-temperature setup (discussed in ch.4, section 4.3) are presented in figure 5.6. The Gaussian fit of low excitation PL spectra was applied, revealing a single peak occurred at 3.02 µm (410 meV) for the GaAs sample and slightly shifted to 3.09 µm (401 meV) for the Si sample, which attributed to the transition from electron to confine hole states (e-hh_1). In addition, the Si sample exhibited two broad side peaks which are probably due to free

carriers recombining through defect energy states. The theoretical simulation of the band structure suggests the transition energy E_t = 411 meV, which is in excellent agreement with the experimental result. The full width at half maximum of PL peaks was also similar to 18 and 23 meV for GaAs and Si samples, respectively. The intensity of the Si sample's mean peak was only 2.2 times less intense than that of GaAs. This is attributed to the much higher defect density within the active region of the Si-based LED arising from the highly strained InAlAs/GaSb interface.

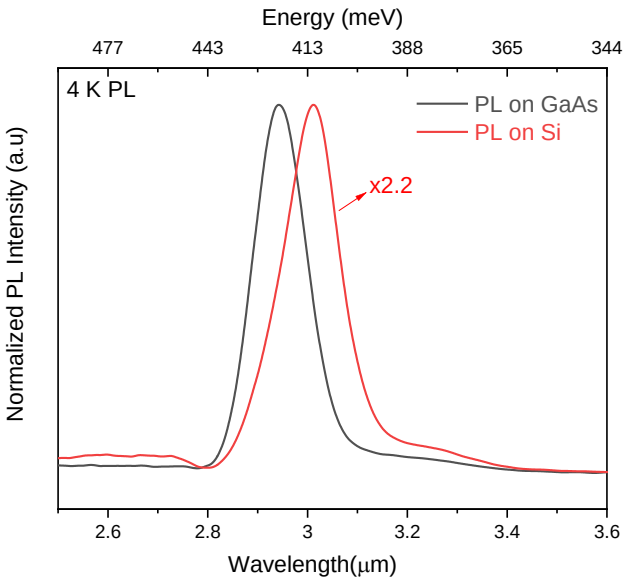

Figure 5.6:Photoluminesence spectra measured at 4 K show the substrate's effect on the peak emission.

In addition, it was remarkable to find that the sample integrated on Si exhibited a redshift in the peak position of 9 meV compared with the one grown on GaAs. This redshift was caused by residual strain in the AlInAs/GaSb/Si interface. For instant, the residual tensile strain derived using equations 2.10 and 2.11 was 0.1% in the GaSb layer, established during the cooling process after growth. In heteroepitaxial systems, strain is significantly considerable due to the differences in lattice constant and thermal expansion coefficient differences between the epilayer and substrate. It was reported

that the difference in thermal expansion coefficient between the Si substrate and III-V structure adds further strain to the epilayers, which results in lattice deformation of GaSb[116]. It has been demonstrated that the redshift in the PL peak position is due to the strain effect on Si and III-V structure as reported for bulk InAsSb[74] where a shift of 9 meV was observed which is an excellent match to the redshift behaviour illustrated in figure 5.6. A similar PL shift trend was reported on the InP layer grown on Si substrate [116].

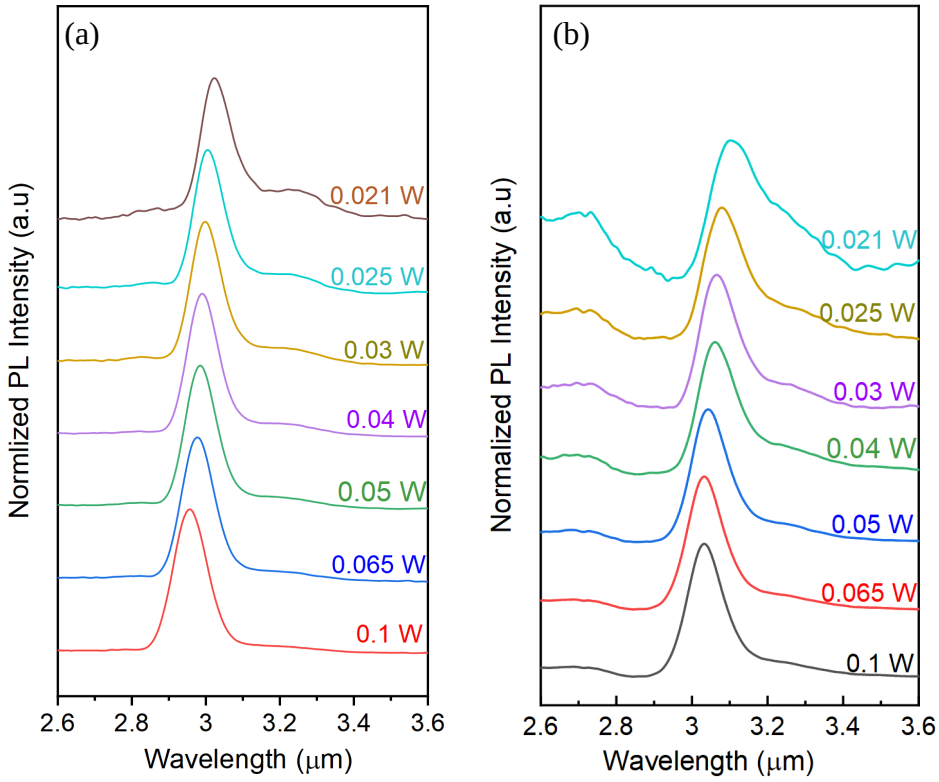

Figure 5.7: The 4 K normalised PL spectra from (a) GaAs and (b) Si samples under different laser excitation power where a single peak emission related to e-hh$_1$ is identified in all samples.

The 4 K power-dependent of photoluminescence emission spectra of two samples is shown in figure 5.7. The PL peak spectra were normalised to the same peak intensity, and all samples exhibited a single asymmetric gaussian peak indicating that the

electrons are strongly localised in the wells. The FWHM values of PL peak increase from 11 to 18 ± 2 meV (GaAs) and 15 to 24 ± 2 meV (Si) due to the increased density of states. This inhomogeneous broadening of linewidth is related to small dispersion of QW thickness or fluctuating in material compositions. At the lowest injection power (P = 0.021 W), the Integrated intensity of the Si sample was ~ 28 % lower than that of GaAs. As laser excitation increases, the peak position is slightly blueshifted by 12 meV (GaAs) and 14 meV (Si), mainly due to the band gap-filling effect. Due to the gradual filling of the energy states within the band tails caused by increasing excitation power, localised emissions are typically characterised by a blueshift of maximum position with increasing excitation density[117]. Depending on the amount of excitation density, the emission related to free carriers/excitons can be observed at the high energy tail of the PL spectra. A recent study investigates the effect of excitation density on PL spectra of thin heterointerface QWs featuring a different band alignment. It was reported that a slight blue shift of ~ 7 meV of type-I InAs/AlAs QW compared to that of ~ 35 meV of type-II AlSb/AlAs QW[118]. Notably, the spectra shape of PL emission becomes symmetric with a smooth slope on the low energy tail, which follows the relationship $l\ \alpha\ (E_t - \hbar\omega)^{1/2}$, where E_t is the threshold energy, and l is the spectra intensity at photon energy $\hbar\omega$[119].

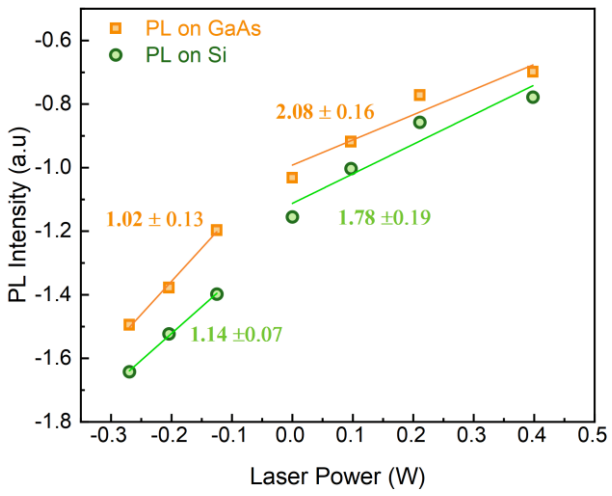

Figure 5.8:The log-log plot of Integrated peak intensity as a function of laser power for GaAs(orange) and Si(green) samples and corresponding Z values.

Further information about the nature of the low-temperature recombination mechanism in the InAsSb/AlInAs MQW active region can be determined. The integrated PL intensity from mean peak versus laser excitation power is plotted in log scale in figure 5.8. The value of Z is calculated according to $P\ \alpha\ n^Z$ and $L\ \alpha\ n^2$ where P is the incident laser power and L is the spontaneous emission intensity. A unity value of Z indicates SRH, two radiative, and three Auger processes. Inspection of figure 5.8 revealed two notable regions where the calculated Z values varied depending on the excitation level. For instant, at low excitation region, the GaAs and Si-based MQW structures show comparable Z values confirming the influence of SRH recombination on both samples. However, at high excitation power radiative process is more likely to dominate at low temperatures when injected carrier density is limited to $n = 4x10^{14}/cm^3$. The slight discrepancy in Z value between GaAs and Si samples is expected due to the high defect density arising from the highly strain AlInAs/GaSb/Si interface.

5.4.2 Excitation in temperature varied PL

Temperature-dependent PL measurements were evaluated, and corresponding spectra are shown in figure 5.9. In temperature range 4- 40 K, the peak exhibited a blue shift due to band filling toward 2.94 µm (GaAs) and 2.98 µm (Si) before decreasing significantly in intensity. At T > 40 K, the PL spectra are red-shifted with increasing temperature due to shrinking bandgap and emission is observed up to 240 K corresponding to the peak position of 3.23 µm (GaAs) and 3.33 µm (Si). The competition between the blue and redshift in the PL spectra was also demonstrated[28].

Over-temperature range 4- 240 K, the integrated intensity of GaAs sample is quenching seven times higher than that of Si Sample and its evidence found in the PL spectra. This could explain by the improvement in material quality in Si because of grown a thick GaSb buffer, which contains most of the thread dislocation. The temperature dependency trend of PL spectra may interpret as follows. As temperature increases, trapped carriers may be thermally activated into the delocalised state, where they are captured by non-radiative channels. Because the activation energy of the carriers depends on their localisation energy, a temperature increase might cause thermal quenching of the localised PL to a degree related to its localisation energy, causing a strong redshift of the localised PL maximum[117]. This evidence that the thermal behaviour of InAsSb MQW emission is described by localised carriers. In addition, the PL emission related to localized states often has a characteristics thermal behaviour[120]. The reduction in the radiative rate, as well as the non-radiative mechanism, will be explicitly discussed in the electroluminescent

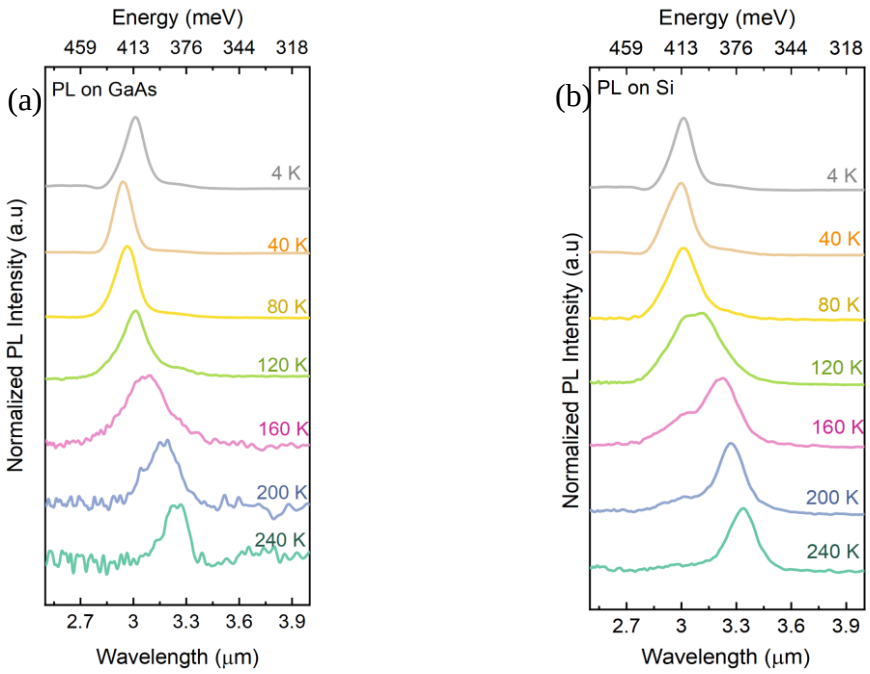

Figure 5.9: Temperature-dependent PL spectra obtained from (a)GaAs and (b) Si MQW samples.

5.5 LEDs characterisation

The MBE samples were processed into square 800µm × 800µm mesa-etch LEDs using photolithography and a wet chemical etching process. The p-type AlInAs layers and MQW layers were etched using sulfuric acid: H_2O_2: H_2O (1:8:80). A 200 nm thick top metallic Ti/Au contact was deposited on the top of the p-type AlInAs layer by thermal evaporation and metal lift-off. The second photolithography step was carried out to pattern the sample for the subsequent wet etching of the mesa requiring etching through the structure and stopping within the n-AlInAs layer. Finally, a Ti/Au metallic contact was deposited on the n-AlInAs layer to provide an Ohmic contact to the n-side of the heterostructure.

5.5.1 Light-Current characterisation (I-V)

The current-voltage characterisation for GaAs and Si-based LEDs is measured at room temperature according to the setup illustrated in ch 4, section 6. The series resistance R_s are calculated from the slope of the curve at a high voltage regime and found to be 7.7 Ω (GaAs) and 7 Ω (Si), as shown in figure 5.10. Interestingly, the GaAs-based LED show an unusual offset which could be due to black body radiation. Although the I-V test was performed in a dark room, there is might be a certain amount of blackbody radiation from the box where the sample placed inside. Therefore, this might cause residual indirect photocurrent. Despite this, the I-V characteristics indicate an expectable value of R_s, there is still a need to optimise the device performance.

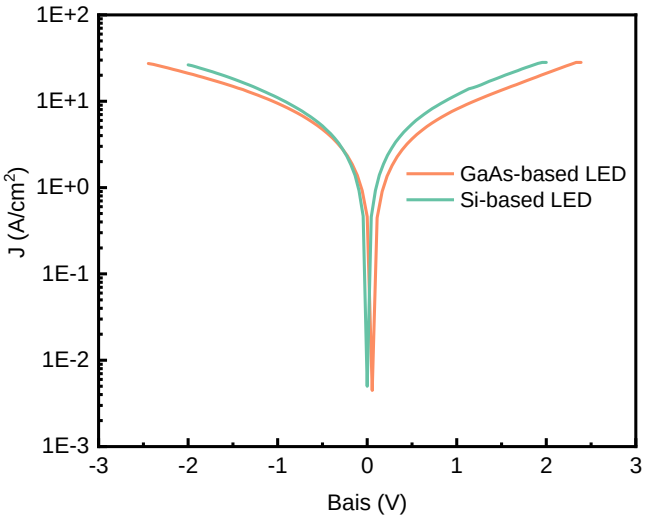

Figure 5.10: The current-voltage Curves of GaAs and Si-based LEDs measured at room temperature.

5.5.2 Comparison of LEDs electroluminescence with photoluminescence samples

The electroluminescence measurements were taken according to the procedure described in section 4.6. Spectra were obtained using a 700 mA injection current, 10% duty cycle and frequency of 1 kHz. The 77 K PL spectrum is compared with the EL spectrum obtained from unintentionally doped InAsSb/AlInAs MQW in fig 5.11. In all cases, the central peak is interpreted as recombination between the first confined electron state to the ground heavy hole state (e-hh_1). The 77 K PL peaks are identified at 2.97 µm and 3 µm, however, broader EL peaks are identified at 2.92 µm, and 2.95 µm for GaAs and Si-based LEDs, respectively. The difference in the peak energy due to different substrates could be due to composition inhomogeneity or layer thickness fluctuations. The energy shift of ~7 meV between the PL and EL may be attributed to the differences in the principle of measurements.

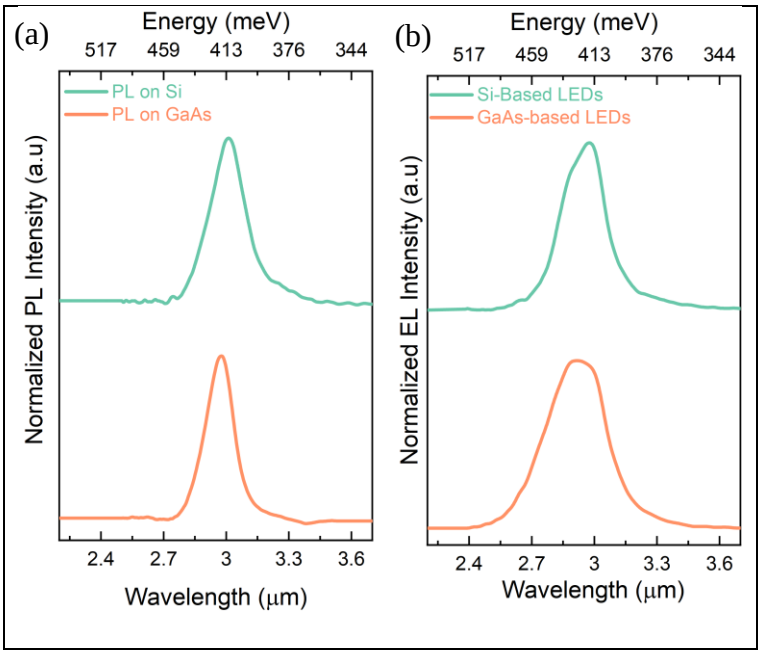

Figure 5.11: A comparison of low temperature 77 K (a) photoluminescence and (b) electroluminescence spectra for the GaAs (orange) and Si (green) samples.

5.5.3 Temperature-dependent of EL spectra

The temperature-dependent electroluminescence spectra measured from the GaAs-based and Si-based MQW LEDs are shown in Figures 5.12 (a) and (b), respectively. With increasing temperature, the EL spectra of both devices exhibited a redshift, broader linewidth, and significant quenching of intensity. Notably, the GaAs-based LED show another peak at T = 160 K observed on the high-energy tails. This may be attributed to the thermalised carrier distribution as carriers at high temperatures occupy sub-band states spreading over a large energy range compared to low temperatures [27]. The emission spectra are affected by an atmospheric water absorption feature between 2.9 and 3.1 μm. As the emission peak red shifts with increasing temperature, the impact of this absorption is primarily visible in a suppression of the high energy tail. Interestingly, the EL spectra of both diodes show strong carrier localization whereas this behaviour was not observed on the PL spectra (figure 5.9).

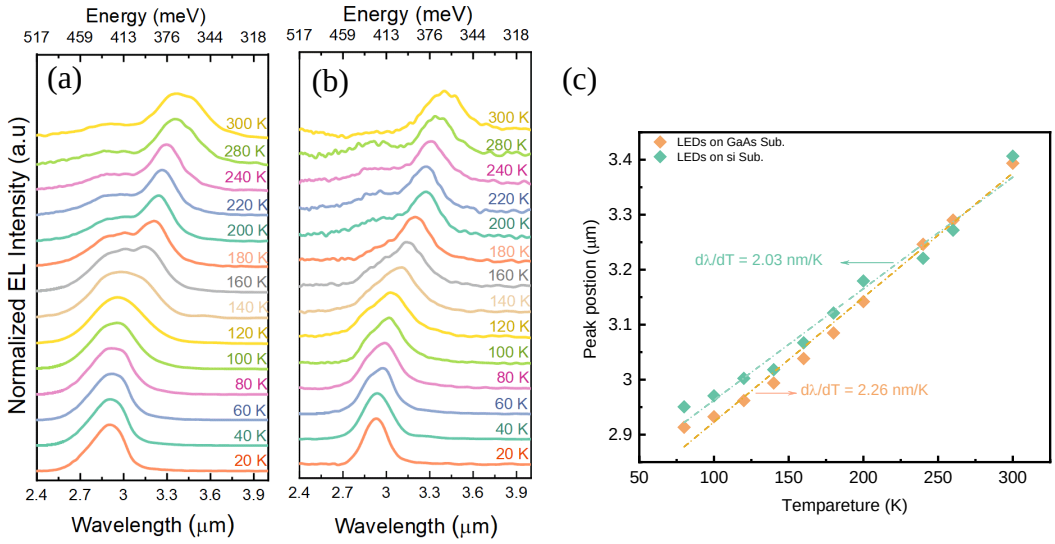

Figure 5.12: Temperature-dependent normalised EL spectra of the (a) GaAs and (b) Si-based LEDs measured using a Bruker Vertex 70 Fourier transform infrared (FTIR) spectrometer. The operating conditions are 700 mA injection current at 1KHz and a 10 % duty cycle. The rate of change of peak position with respect to temperature for GaAs (orange) and Si (green) is also indicated (c).

The temperature dependency of the peak position of GaAs and Si-based LEDs are plotted in figure 5.12 (c). There is a shift toward a longer wavelength as temperature increases from 80 – 300 K at a rate of 2.26 nm/K and 2.03 nm/K for GaAs and Si LEDs. This shift is due to the temperature dependency of the bandgap. It's interesting to note that the emission intensity of both LEDs decreases considerably with increasing temperature due to several factors such as the non-radiative process (i.e. deep levels) and carrier loss over heterostructure barriers. The temperature dependency of LED emission intensity is often described by[63]:

$$I(T) = I_o\, e^{-T_d/T_c} \qquad (5.1)$$

Where $I(T)$ is the luminescence intensity, T_d is device temperature, and T_c is characteristic temperature. A higher T_c value implying weak temperature dependence.

The calculated T_c Values are 56 ± 1.48 K and 47 ± 2 K for GaAs and Si-based LEDs. It should be noted that the characteristic temperature may strongly depend on the layer structure of the active region and hence the indication of the quality of the material.

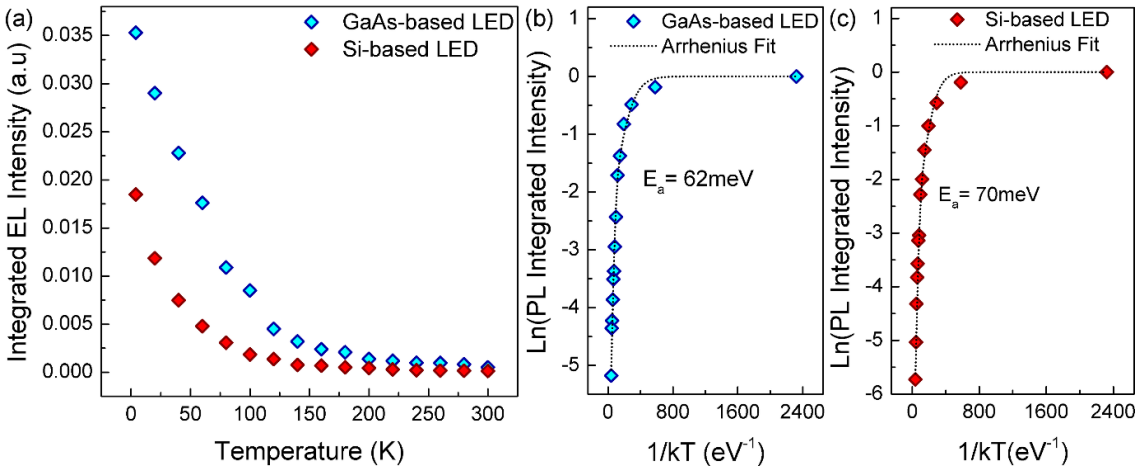

Figure 5.13 (a) Temperature dependent integrated EL intensity data obtained for both LED devices. (b) and (c) Arrhenius plots of the integrated EL intensity resulting in activation energy of 62 meV and 70 meV for the GaAs and Si-based LEDs, respectively.

Figure 5.13 (a) shows the quenching of the EL intensity over the temperature range of 20 to 300 K measured for both Si- and GaAs-based LED. With the increasing temperature up to 300 K, the integrated intensity decreases by factors of 67 and 136 for the GaAs and Si LED, respectively. Figures 13 (b) and (c) show the corresponding Arrhenius plots, which were fit using the equation:

$$I = \frac{I_o}{1+C\exp(-E_A/K_bT)} \qquad (5.2)$$

where I_o is the EL intensity at temperature T = 0 K, C is the non-radiative process coefficient and E_A is the activation energy of the mechanism responsible for the EL quenching. The dash-dot lines represent the fittings to the experimental data resulting in activation energies of 62 (GaAs) and 70 meV (Si), which are close to the first electron state localisation energy (63 meV). This result indicates that leakage of electrons from

the QWs is a major mechanism limiting the device performance in addition to the non-radiative Shockley-Read-Hall and Auger recombination.

During the recombination process, carriers must be injected into the active region and, once injected, they must confine within QW. Escaping carriers out of the well is most likely due to weak carrier confinement by the barrier. It is likely that carriers that bypass the active region will join non-radiatively either at confinement regions or at the semiconductor-metal interface. Consequently, lack of capture and escape is known as carrier leakage out of the active region. To reduce this effect, the blocking barrier shown in figure 5.3 (a) was designed to prevent carriers from escaping where the height of the barrier was 180 meV. It should be noted that carrier escaping is strongly dependent on the carrier concentration which was relatively large in the LED ($n \sim 1.3\text{x}10^{17}$ cm^{-3}). It's possible to describe the total recombination rate R in the active region according to the following:

$$R_t = An + Bn^2 + Cn^3 + f(n) \qquad (5.3)$$

where A, B, and C are the SRH, radiative and Auger coefficients. The term f(n) denotes for escape carrier out of the active region. The If free carriers n recombined by non-radiative processes, this will reduce the emission intensity from the active region. Although the radiative recombination proportion to n^2, the temperature-dependent non-radiative Auger recombination processes proportion to n^3 which results in more significant temperature quenching of the PL and EL. However, the ABC model oversimplified the physics process in the LED where the effect of carrier escaping and carrier drafting out of the active region is neglected which does not describe the actual recombination process in the real MQWs LED. In addition, the carrier concentration of electrons and holes are assumed to be equal to each other. Moreover, this model was

derived for bulk materials and to generalize on MQW structure this would be a subject of research interest in the future.

The temperature dependence analysis of the EL peak energy of both LEDs is shown in Figure 5.14. The measured data were fitted using equation 2.1

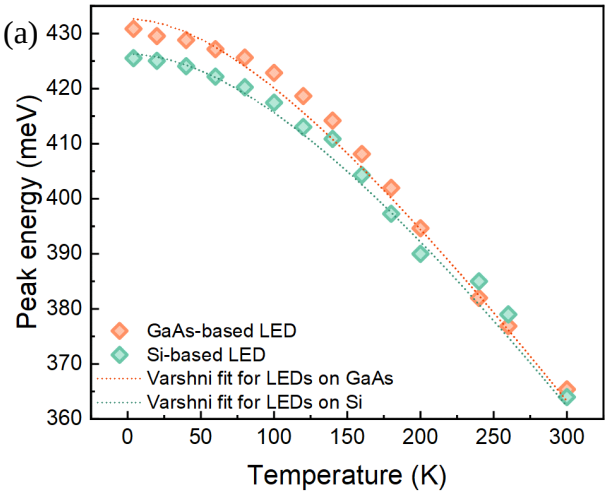

(b)

Table 5.1: A summary of temperature dependency fitting parameters obtained using the Varshni equation.

Structure	Varshni fitting parameters		
	E0 (eV)	α (meV/K)	β (K)
LED on GaAs	0.432	0.39	218
LED on Si	0.426	0.42	300

Figure 5.14: (a)Temperature dependence of the electroluminescence emission peak energy (e-hh1transition) obtained for the InAsSb/AlInAs MQW LED integrated on GaAs and Si substrates. The dash-dotted lines represent the Varshni fitting of the experimental data. (b) The Varshni fitting parameters of GaAs and Si-based LED.

where E_0 is the bandgap at 0 K, α and β are material dependent constants, and T is the temperature in Kelvin. The Varshni fitting parameters given in table 1 agree with those reported previously for bulk InAsSb LEDs grown on Si[74].

5.5.4 LED output power measurements

Figure 5.15 shows the output power performance of both LEDs measured at room temperature for different input currents. A low duty cycle of 1% at 1 kHz was used to reduce Joule heating of the devices. Maximum output powers of 63 and 80 μW were obtained at 1500 mA for the GaAs and Si-based LED, respectively. The external quantum efficiency EQE of the device can be estimated according to eq 2.56. The EQE were determined to be 0.011% (GaAs) and 0.014 % (Si). The decrease in the input currents below 1A resulted in higher output power values for the GaAs-based LED as compared to that obtained for the Si-based device in agreement with the low-temperature spectroscopy results. However, for higher currents (>1A), the Si-based LED demonstrated a significantly stronger output power despite the higher defect density. This can be attributed to the improved thermal conductivity of the Si wafer, as reported previously for an Sb-based superlattice LED grown on Si[121]. This evidence is also suggesting that Si-based LED is less sensitive to the effect of duty cycle increasing due to superior thermal management. Table 2 summarises the performance of diodes integrated into GaAs and Si substrates. The emittance of GaAs-based LED is ~ 0.87 mW/cm^2 which is nearly four times less than that reported for bulk AlInSb/InSb grown on GaAs substrate (3.4 mW/cm^2)[68]. Despite this, the Si-based LED is the first emitter operated ~ 3.4 μm integrate on Si wafer which is a remarkable achievement in this challenging wavelength.

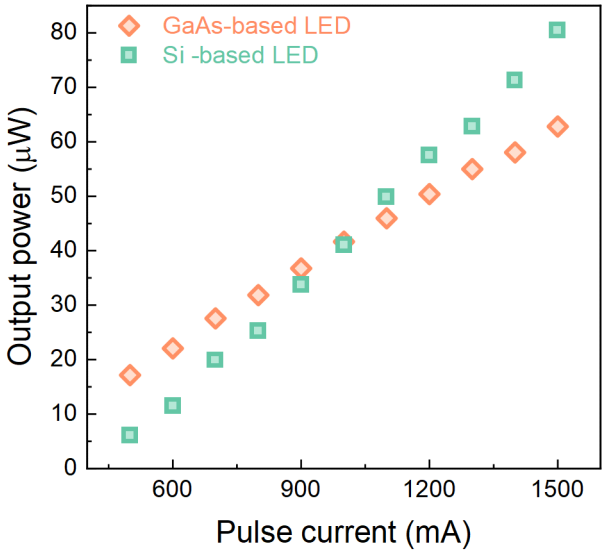

Figure 5.15: The room temperature output power-current plots obtained for the GaAs and Si-based LEDs at 1KHz using a 1% duty cycle.

Table 5.2: Summary of the optical and electrical properties of InAsSb/AlInAs MQW LED integrated on GaAs and Si measured at room temperature.

	LED on GaAs	LED on Si
Wavelength (μm)	3.39	3.38
Power (μW) (I =1.5A, DC=1%,f = 1kHz)	63	80
EQE (%)	0.011	0.014
Diode Ideality factor (a.u)	1.5	1.6
FWHM (μm)	0.373	0.286
Shift in Peak Position (nm/K)	2.26	2.03
Temperature Quenching of Integrated EL Intensity (a.u)	67	137
EL Characteristic Temperature (K)	55	47

Chapter 6: Mid-infrared Type-II InAs/InAsSb strained layer superlattice Light-Emitting Diodes (LEDs) integrated on GaAs and GaSb substrates.

6.1 Introduction

The essential feature of type-II band alignment is the partial overlap between the conduction and valance bands of different materials, as discussed in section 2.1.2.2 in the theory chapter. The spatial separation of electrons and holes leads to unique tunnelling-assisted radiative recombination transition and novel transport properties [122–124]. The type-II structure has potential advantages, including tuning the bandgap from middle to far-infrared and large band offsets of conduction and valence band for enhanced electrical confinement; therefore, it is worth studying. This chapter analyses with comparison to the simulation of the effect of changing antimony contents and varying layer thickness on the optical properties of type-II InAs/InAsSb strained layer superlattice (SLS). Based on that, two series of InAs/InAsSb superlattice structures have been grown on lattice mismatch GaAs substrates. The first set of samples has the same period's thickness, while the second set of structures has the same Sb contents. These MBE samples were examined using x-ray diffraction, followed by the investigation of the power and temperature dependency of photoluminescence spectra. In this manner, we conclude an optimal sample structure to transfer into an LED system. This involvess the successful growth of InAs/InAsSb SLS on lattice match GaSb and metamorphic GaAs wafers. The quality of the samples was also investigated with XRD. This is succeeded by exploring the optical properties of the two LEDs obtained by

electroluminescence measurements. The investigation of light-current behaviour and the determination of the output power of these LEDs is also demonstrated.

6.2 Design and growth type-II InAs/InAsSb SLS

6.2.1 Nextnano study of InAs/InAsSb SLS

Several simulations were conducted using Nextnano to predict the transition energy and the matrix elements of the envelope functions (the spatial electron and hole overlap). Considering an example of a thin superlattice structure of 3 nm InAs and 3 nm InAsSb, the calculated type-II band structure of InAs/$InAs_{0.91}Sb_{0.09}$ SLS at low temperature (4 K) along with energy levels of electron and the heavy hole is shown in figure 6.1(a). In addition, the effect of increasing Sb contents on the SLS energy gap is illustrated in figure 6.1 (b). Increasing Sb contents in the InAsSb layer from 4 % to 20 % raises the conduction band and, consequently, increases the energy of the e_1 level from 1.92 eV to 2.0 eV. Similarly, the energy of hh_1 minibands increased from 1.54 eV to 1.76 eV. The conduction band offset Δ_{CB} is smaller than the valence band offset $\Delta_{VB;}$ for an instant at (Sb = 4 %), the confinements energy of the electron is shallow ~21 meV. The varying Sb composition in the superlattice is also associated with reducing the electron and hole wavefunction overlap. For instance, increasing Sb from 4 to 20 % reduces the electron, and heavy hole (e - h) overlap by 20 percent, as illustrated in figure 6.1 (c). This trend is explained by the nature of the type-II band structure, where electron and hole wavefunctions are located on the opposite side of the InAs/InAsSb structure. Hence, the e – h transition occurs only where the probability distribution functions are cojoining. Therefore, introducing more Sb increases the type-II behaviour, resulting in significantly lower overlap probability directly related to the recombination rate of free carriers.

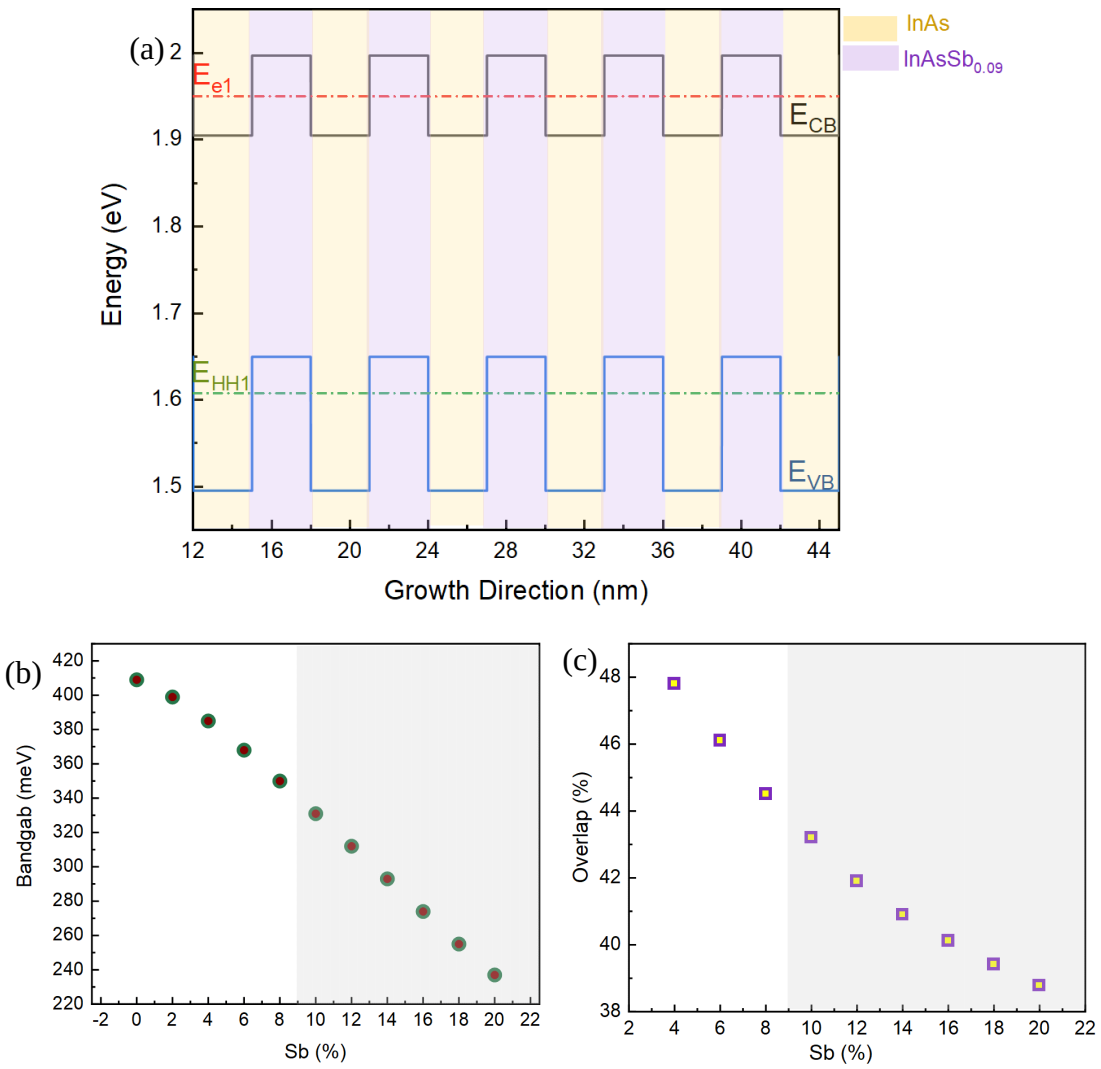

Figure 6.1: (a) The calculated band structure of the InAs/InAs$_{0.91}$Sb$_{0.09}$ SLS lattice matched to GaSb, where the first electron and heavy hole bands are highlighted. (b) Dependence of the energy gap of InAs/InAsSb on Sb contents, where a significant reduction in the bandgap with increasing Sb is observed. The shaded part of the data represents the possibility of growing strained balanced superlattice on GaSb substrate. (c)The overlap of the envelope function of electron and heavy hole as a function of Sb composition.

6.2.2 Growth of InAsSb/InAs SLS on GaAs Sub

The growth of PL samples was carried out by Dr Veronica Letka using the steps described in the 4.1 section. Before the growth of the active region, the GaAs wafer was

outgassed, and the oxide desorption step was introduced. A thin buffer layer of GaAs, the same material as the substrate, ~300 nm was grown. Gallium flux was stopped to pause the growth, followed by 10 seconds of As flux interruption to encourage a Ga terminated surface. Next, the Sb valve is opened to establish the formation of an interface misfit (IMF) array. The buffer is then completed by reintroducing Ga flux to grow a thick GaSb layer, at a growth temperature of T_g ~500^o C. Next, the substrate growth temperature is reduced under Sb flux to the desired superlattice growth temperature.

Two sets of PL samples have been considered in this study; the varying Sb fraction sample set A, and the varying layer thickness sample set B. In sample set A, the Sb changes in two steps while in sample set B, the period thickness changes in four steps. In all cases, the active region was grown at T_g ~475^o C, and the III:V growth rate ratio was kept between 1:1.6 to 1:1.8, which is desirable for high quality antimonide growth according to extensive work carried out in our research group. The details of the sample structure are shown in figure 6.2.

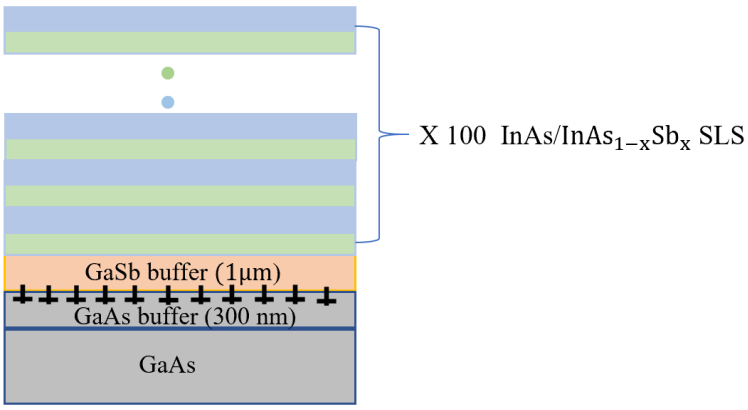

Figure 6.2: Schematic of the PL samples showing multiple periods of InAs/InAs$_{1-x}$Sb$_x$ grown on GaAs Substrate.

The critical thickness h_c of InAsSb grown on InAs was estimated according to the Mathews and Blakeslee model (equation 2.17), and the corresponding calculation is

plotted in figure 6.3. In this example, 1 ML of InAs is integrated with 1 ML of $InAs_{1x}Sb_x$ where the strained balanced condition can be achieved using ~ 18% Sb. it is interesting to note that all SLS samples exhibit thickness much lower than the critical thickness, and the quality of these samples are evidence found in the HRXRD scan, as discussed later

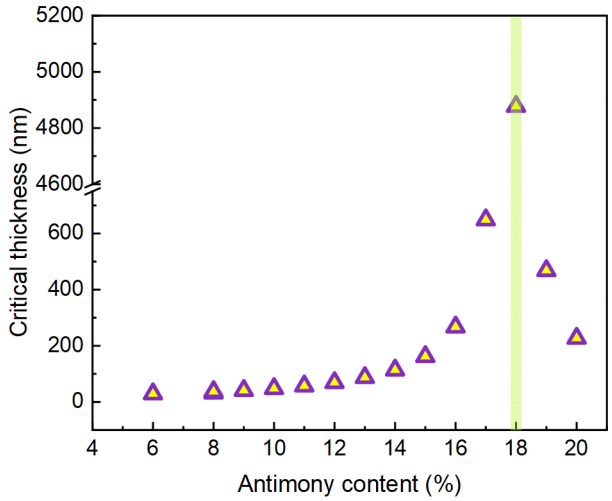

Figure 6.3: The calculated critical thickness according to Matthews Blakeslee model of InAs/InAs1-xSbx superlattice on virtual GaSb substrate. The green shaded area represents the maximum critical thickness that can be achieved.

6.3 Structural characterization of InAs/InAsSb SLS

The quality of grown MBE samples is investigated with high-resolution x-ray diffraction HRXRD using the setup described in section 4.2.

6.3.1 Comparison of SLS samples with varying Sb contents

Figure 6.4, represents the ω-2Θ scan obtained from HRXRD of period constant antimony changes (sample set A) and denoted as (a) SLS 1 and (b) SLS 2, respectively.

A summary of fitting parameters used to model InAs/InAsSb SLS on the GaSb buffer layer is presented in table 6.1. The ratio thickness of the superlattice layers kept the same with the ratio of d_{InAs} to $d_{InAs\ Sb}$ 1:1; however, the Sb contents were varied to investigate the effect of increasing Antimony in the superlattice bandgap. Inspection of Table 6.1 indicates SLS 1 has the lowest Sb (14.5 %) and the superlattice period is almost the same despite a slight variation in the thickness. The 0th order of SL peak is the highest intense satellite peak and cannot be distinguished from the GaSb peak; therefore, a comparison of full width at half maximum FWHM of the 1st order SL peak indicates that SLS 1 is slightly border than that of SLS 2 by 2.4×10^{-3} deg (8.64 arcsec). In addition, the separation angle between 0th order and 1st order SLS peaks was also similar (0.4056 deg SLS1 and 0.3975 deg). This is expected as changing Sb contents move the XRD fitting to the left or right while changing thickness control the separation between the superlattice peaks.

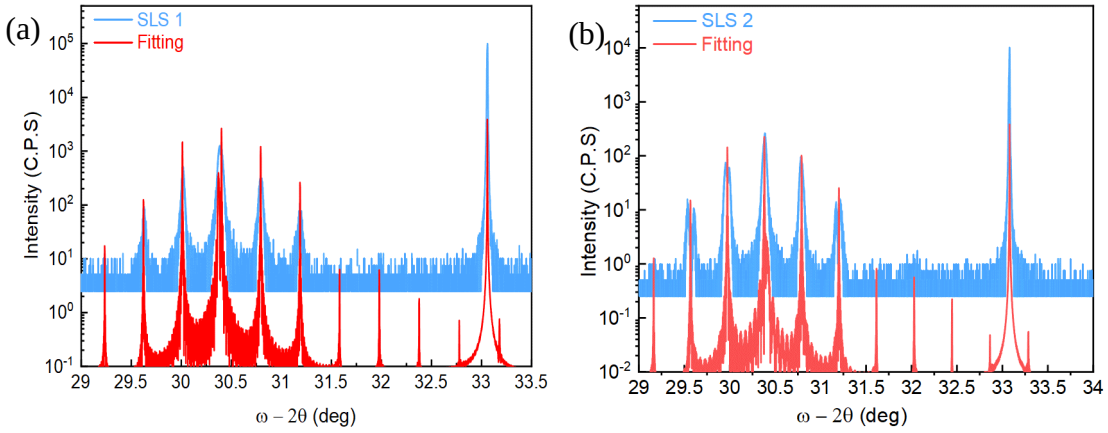

Figure 6.4: HRXRD scan of sample set A for (a) SLS 1 (Sb= 14.5 %) and (b) SLS 2 (Sb= 16.3 %) where the blue line represents the data, and the red line represents the simulated InAs/InAs$_{1-x}$Sb$_x$ superlattice structure

Table 6.1: Summary of fitting parameters obtained from Mercury RADS simulation software for sample set A showing the layer thickness, Sb composition and FWHM of the first order satellite peaks.

Sample ID	Sb (%)	Thickness (nm)		No. of SL Periods	FWHM SL_{-1} (deg)/(arcsec)
		d_{InAs}	d_{InAsSb}		
SLS 1	14.5	5.7	7.38	100	0.0421/151
SLS 2	16.3	5.49	7.03	100	0.0397/143

6.3.2 Comparison of SLS samples with varying layer thickness

The HRXRD rocking curves of thickness changing antimony constant (sample set B) are shown in figure 6.5 where a sharp satellite peak can be observed in most samples. Simulation of the XRD curves indicating the Sb contents and thickness of the superlattice structure is summarised in table 6.2. The FWHM of SLS 4 is the lowest as this sample was grown recently for consideration of LED structure design to operating at $\lambda = 5.6$ μm, as will discuss later. The small shoulder observed in the should of 1st order SLS could be due to Sb segregation resulting in compositionally graded interfaces between the InAs and InAsSb layers[34].

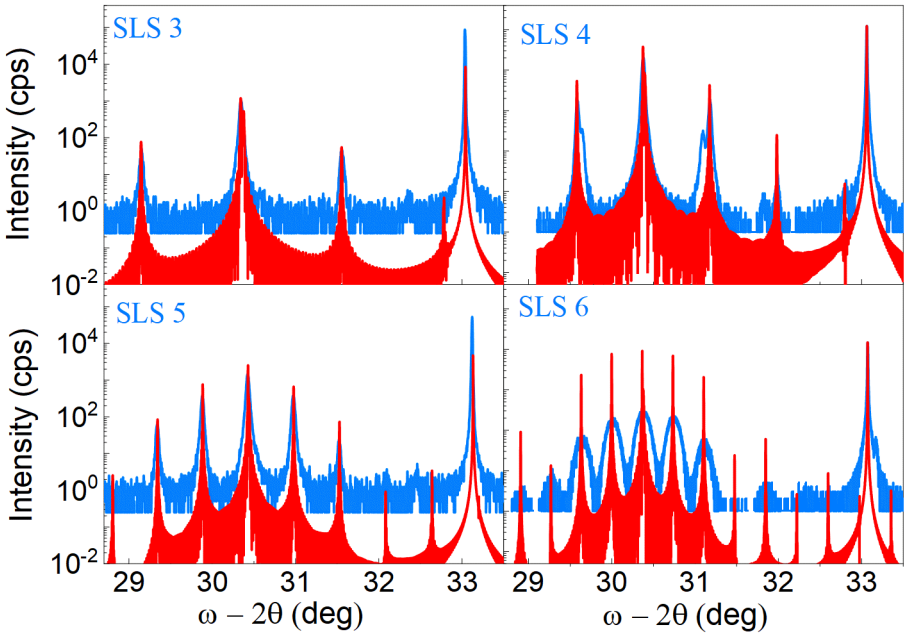

Figure 6.5: XRD scans of sample set B of various superlattice structures grown on GaAs substrate. The influence of period varied while keeping Sb composition the same is highlight effect on the separation distance between the superlattice peaks going from the lowest period (SLS 3) to the highest thickness period (SLS 6). The broad satellite peaks observed in SLS 6 are related to growth issues due to IMF failure leading to the rough surface and consequently wide peaks.

Meanwhile, the Sb contents were kept at the same Sb $\approx$ 17.5 %, although the period varied in aiming to study their influence on the SLS bandgap. The thickness was increased from $d_{InAs} \approx 2$ nm in SLS 3 to $d_{InAs} \approx 7$ nm in SLS 6, with corresponding increases in the InAsSb layer. It is interesting to note that the spacing between superlattice peaks decreases with increasing layer thickness. Narrow SLS peaks indicate high quality and smooth interface. The broad 1st SLS peaks observed in the sample (SLS 6) are attributed to a poor GaAs to GaSb interface with an imperfect misfit dislocation array. This phenomenon originates mostly at the interface between the substrate and the highly lattice-mismatched epitaxial layer and from the local stain[125]. When successful the overlying GaSb buffer is smooth with a low threading dislocation density,

however, this can be lost at times due to growth variations beyond the scope of this work.

Table 6.2: Summary of the structure details of sample set B of InAs/InAs$_{1-x}$Sb$_x$ SLS stating the changes in the period thickness and superlattice peaks. The narrowest FWHM of SLS 4 suggests excellent crystalline quality and an optimal structure to transfer into LED.

Sample ID	Sb (%)	Thickness (nm)		No. of SL Periods	FWHW SL$_{-1}$ (deg) /(arcsec)
		d_{InAs}	d_{InAsSb}		
SLS 3	17.8	1.95	2.29	100	0.0369/132
SLS 4	17.5	3.03	3.37	100	0.0298/107
SLS 5	17.5	4.62	4.74	100	0.0342/123
SLS 6	17.8	6.87	7.03	100	0.1656/596

6.4 Photoluminescence spectra of InAs/InAsSb SLS on GaAs substrates

In this section, the investigation of the impact of varying antimony contents and superlattice periods on the optical properties of InAs/InAsSb T2SL is demonstrated using the experimental setup described in section 4.3.

6.4.1 4 K PL comparison of SLS samples with varying Sb contents

Figure 6.6 exhibits the normalised PL spectra at 4 K for SLS 1 and SLS 2 samples, where an excitation density of 0.075 W/cm^2 was achieved using a 3 % optical filter. When Sb increases from 14.5 % to 16.5 %, a single Gaussian function is observed with peak photon energy decreases from 255 meV(4.86 µm) to 243 meV(5.10 µm) for SLS 1 and SLS 2, respectively.

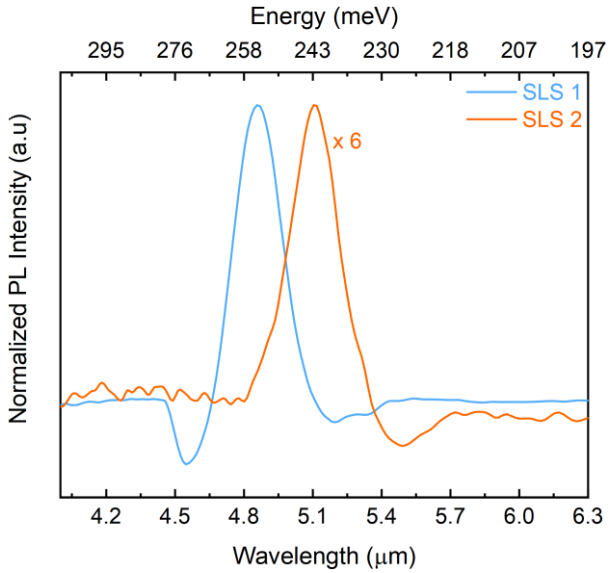

Figure 6.6: The Photoluminescence spectra measured at 4 K show the Sb effect on the peak emission of the sample set A (SLS 1 = 14.5 % Sb and SLS 2 = 16.3% Sb).

The redshift in PL spectra is associated with a decrease in the PL intensity by a factor of six and a slightly broadened peak (the FWHM of SLS 2 is 251 nm compared to 240 nm observed on SLS 2). From HRXRD measurements (section 6.4.1), SLS 2 sample has the highest Sb contents, where the calculated critical thickness h_c indicates a value of 1840 nm (SLS 1) and 1467 (SLS 2), which is larger than the total InAs/InAsSb thickness of 1252 nm in the SLS 2 sample. Hence, misfit dislocation can not be accounting for the reduction in the PL intensity in the sample with higher Sb contents. This conclusion is also supported by the high crystallinity shown in fig 6.4. Therefore, the 6x reduction in the intensity might be explained by the growth quality probably points defects or background carbon. The shift in the PL spectra and broad linewidth is consistent with the spatially indirect transition of type-II QW[126,127]. The absorption features observed in SLS 1 sample near 4.5 μm are associated with FTIR averaging setup.

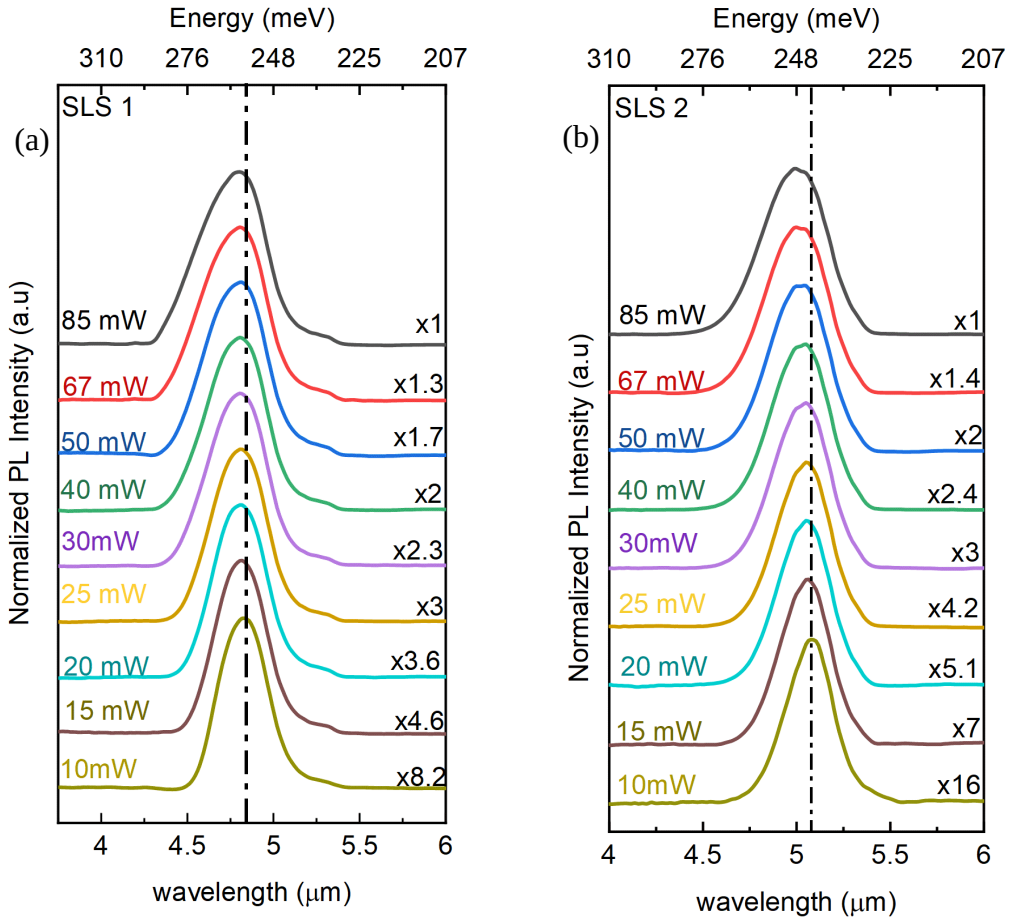

Figure 6.7: The 4 K normalised PL spectra from sample set A for (a) SLS 1 and (b) SLS 2 samples under different laser excitation power highlight the decrease in the PL intensity with increasing Sb. The black short dashed line represents the simulated e-hh1 transition energy.

The 4 K Power-dependent PL spectra for SLS 1 and SLS 2 samples were measured with different excitation density, as illustrated in figure 6.7. Band structure simulation obtained by Nextnano suggests that e-hh_1 transition energy is 255 meV for SLS 1 and 244 meV for SLS 2. These values are in excellent agreement with low excitation energy PL peaks. A blueshift of the bandgap of 9 meV (SLS 1) and 6 meV (SLS 2) is observed as the laser power is increased from 10 – 85 mW. Such blue shift in type-II structure is due to the band filling effect [28].

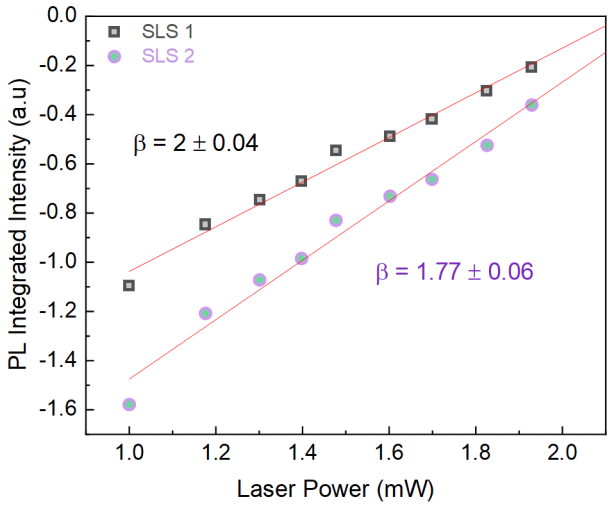

Figure 6.8: 4 K Integrated photoluminescence peak intensity of sample set A as a function of laser excitation power on a log scale.

The integrated PL intensity versus laser excitation power is plotted on a log scale in figure 6.8. The value of β is calculated according to $P\ \alpha\ n^{\beta}$ and $L\ \alpha\ n^{2}$ where P is the incident laser power and L is the spontaneous emission intensity. The calculated β values were similar to 2 ± 0.04 (SLS 1) and 1.77 ± 0.06 (SLS 2), indicating that the probability of radiative recombination occurring is most likely with a lower Sb sample. The discrepancy in β value between SLS 1 and SLS 2 samples is partially explained by the overlap of the electron and hole wavefunction, which determines the rate of radiative rate. According to equation (2.29), the e - h wavefunction overlap is estimated at 42% for SLS 1 and 40% for SLS 2 which is evidenced by the β value where the lowest Sb sample (SLS 1) is brighter than that with the highest Sb (SLS 2).

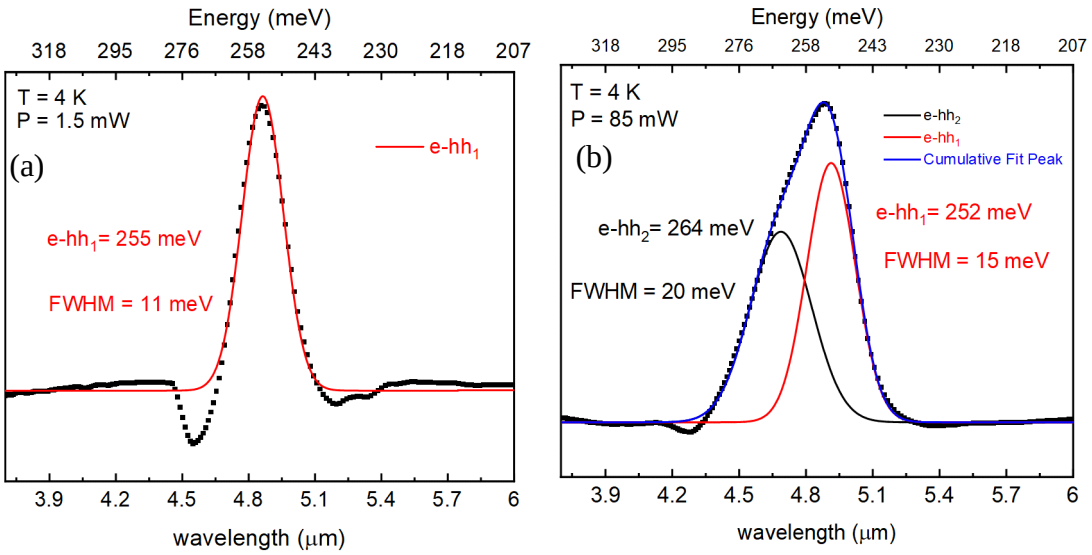

Figure 6.9: The Gaussian deconvolution of photoluminescence spectra of SLS 1 at various excitation power (a)1.5mW and (b) 85 mW.

A gaussian deconvolution of low excited PL spectra (P =1.5mW) of SLS 1 indicates a single peak originated from the transition of an electron to a heavy hole confinement state (e-hh1) associated with peak energy 255 meV and linewidth of 11 meV (see figure 6.9 (a)). At high excitation power (P = 85 mW), there is a shoulder on the high energy side of the PL spectra in figure 6.9 (b) corresponding to the transition to the second excited heavy hole state (e-hh2) with a peak energy of (264 meV) and linewidth of 20 meV. The separation between these peaks is 12 meV, which contrasts with simulation results that indicate a separation value of 38 meV. However, the experimental finding of (14nm) InAs/(14nm) InAsSb SLS suggests the energy separation should be 4 meV (Sb = 3.8 %) - 8 meV (Sb = 6.2%) [127] which is comparable to the PL results.

6.4.2 Temperature-dependence of PL with varying Sb contents

PL emission intensity spectra from the samples at various temperatures under excitation power density of 4.25 mW/cm^2 are presented in figure 6.10. Over the temperature range 4 – 220 K, the mean peak shifted by 22 meV (SLS 1) and 23 meV (SLS 2). According to band structure simulation, increasing antimony content in the InAsSb well increases type-II behaviour translating to increasing both conduction and valence band offset, resulting in more pronounced confinement of electrons in the InAs layer and holes in the holes InAsSb QWs.

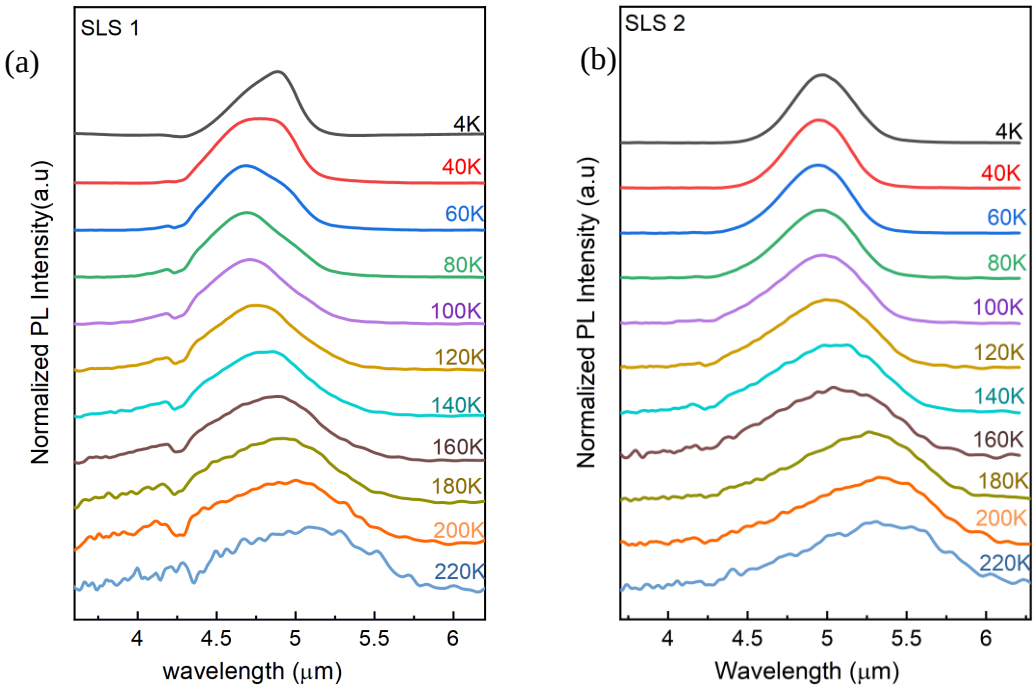

Figure 6.10: Temperature dependence of the normalised photoluminescence spectra of GaAs-based superlattice (sample set A). The effect of increasing Sb in the InAsSb layer from (a) 14.5 % to (b) 16.3 % is clear in the peak position of the PL spectra.

Therefore, it is reasonable to expect the temperature quenching of PL spectra of higher Sb contents to decrease compared to that of lower Sb. However, experimental findings indicated that the temperature quenching of PL spectra of lower Sb sample (SLS 1) is

much greater (84 compared to 36). The higher magnitude of quenching observed with SLS 1 could be due to compositional inhomogeneity or a high impurity.

The 4 K PL emission spectrum of the SLS 1 sample exhibited a shoulder in the high-energy side of the mean peak attributed to e-hh_2 transition. The intensity of this shoulder is almost equal to that of e-hh1 at 40 K, then e-hh_2 transition becomes dominated at T > 60 K. A similar behaviour was reported for InAs/InAsSb MQW, where authors attribute this to the relatively minor splitting of the heavy hole (≈27 meV), which enables thermal excitation of holes from hh1 to hh2 with increasing temperature[61].

Figure 6.11 show the blue shift trend of the InAs/InAsSb SLS bandgap with increasing temperature. . Interestingly, the lowest Sb sample (SLS 1) shows two energy peak related e-hh1 and e-hh2 where the difference between these peaks was ~ 11 meV at 4 K and increased to ~ 16 meV at 220 K. This behaviour was not observed with highest Sb sample (SLS 2) which may be attributed to composition inhomogeneity. There is a blue shift of 12 and 3 meV of SLS 1 and SLS 2 observed up ~ 80 K before both samples are redshifted following the usual trend of III-V materials with increasing temperature. The characteristic blue shift with increasing temperature will be discussed in detail in section 6.4.4. Table 6.3 shows a summary of the experimental versus simulated PL bandgap at 80 K, change in the peak position with respect to temperature, and alongside Varshni fitting parameters.

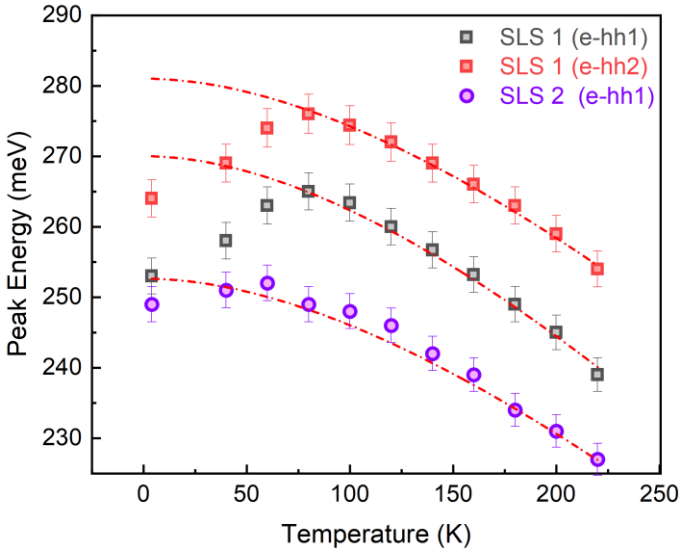

Figure 6.11: Temperature-dependent data of sample set A showing a blue shift trend of the peak energy. The red dash-dotted line represents the fitting of the empirical Varshni expression.

The blueshift was observed in both structures potentially due to several reasons which will discuss in-depth in the next section. As temperature increases above 220 K, the PL spectra become increasingly noisy, and the peak could not be reliably identified.

Table 6.3: The experimental and calculated InAs/InAsSb superlattice bandgap of the sample set A at 80 K. The blue shift trend of the PL peak spectra is indicated alongside the change in the peak position with respect to increasing temperature. The Varshni fitting parameter of the SLS bandgap was extracted from the Gaussian fitting of the PL spectra.

Sample	PL Bandgap at 80 K (meV)		PL Peak Blueshift 4 – 80 K (meV)	$\Delta\lambda/\Delta T$ 80 – 220 K (nm/K)	Varshni Fitting Parameters		
	exp.	sim.			$E_g(0)$ (meV)	α (meV/K)	β (K)
SLS 1	265	245	12	3.6	270	0.38	400
SLS 2	249	234	3	3.5	252	0.33	390

6.4.3 4 K PL comparison of SLS samples with varying period thickness

Figure 6.12 (a) shows the low temperature (4 K) PL spectra of various SLS samples under low exaction power (P = 25 mW). As SLS thickness increases, there is strong variation in the emission wavelength of PL spectra, which is the signature of the influence of period thickness in the superlattice bandgap.

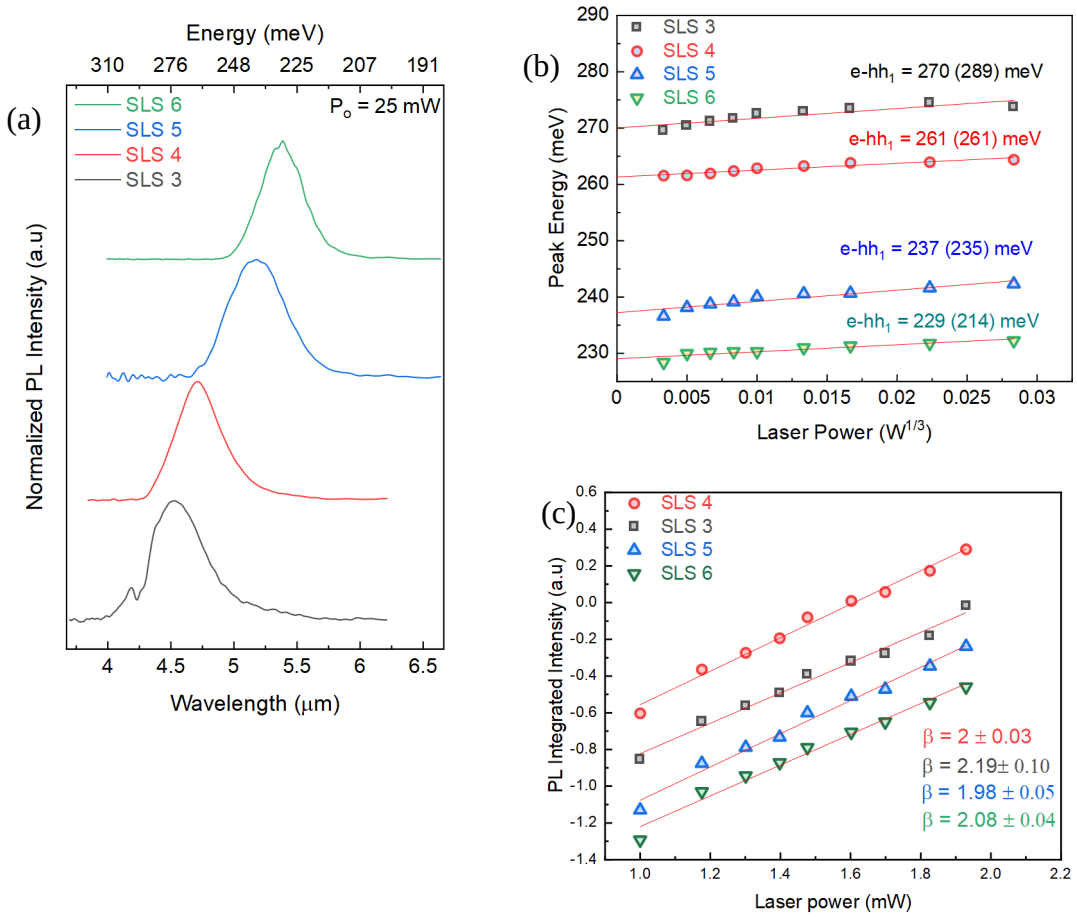

Figure 6.12: (a) 4 K PL spectra of various superlattice structures (sample set B) show the influence of increasing the period on the peak position. (b) The peak energy dependence of the cubic root of laser power and corresponding e-hh1 flat band transition energy, modelled energy is indicated in the value between parentheses for comparison. (c) The log scale of the dominant recombination mechanism is determined by the gradient of integrated PL intensity.

Increasing the InAsSb layer thickness from 2 – 7 nm leads to a shift in the peak wavelength ranging from 4.56 to 5.38 μm. The shift in the emission wavelength is also accompanied by a reduction in the e - h wavefunction overlap. Due to the direct correlation between the electron/hole wavefunction overlap and recombination rate, it is also expected that PL emission intensity decreases with long periods as wavefunction overlap decreases. In particular, the calculated e- h wavefunction overlap is 45 % (SLS 3), 40 % (SLS 4), 34.4 % (SLS 5), and 30 % (SLS 6). Interestingly, for the sample with a lower period (SLS 3), the slightly broad FWHM of PL spectra may be attributed to compositional inhomogeneity or a high density of impurity. Increasing the excitation power density is associated with a blue shift ranging from 6 meV for lower SLS thickness (SLS 3) and 11 meV for higher SLS thickness (SLS 6). The characteristic blue shift behaviour of the superlattice with the influence of power observed in sections 6.4.1 and 6.4.3 can be explicitly discussed. In the multi-quantum well structure, the electrons are strongly localised within the InAs layer and holes are strongly localised in the InAsSb layer, the separated charge leads to a dipole layer in InAs, causing electrons to form an approximately triangular quantum well at each interface with the InAsSb layer. This follows that increasing power excitation density enhances the electric field in the InAs sides and, consequently, the electron states in the squeezed potential well. However, in the superlattice structure, this effect is less pronounced due to the ability of electron wavefunction to penetrate through the SLS. The previous report on the photoluminescence properties of the InAs/InAsSb SLS (Sb = 22 – 37 %) lattice matched to GaSb attribute the blue shift is due to several factors such as band gap renormalization, band filling, band bending effect, or fluctuation in the layer thickness and alloy composition[128]. A band-gap renormalization occurs when Coulomb interactions among free carriers cause a shift in the self-energies of the band-edge

states[129]. The term 'band bending' refers to the spatial separation of electrons and holes in type-II structures [130]. Following previous reports[61,130,131], the flat band transition energies extrapolations method is used to account for band bending resulting from high exaction power. Therefore, the relation between PL peak energy as a function of cubic root of laser power of different SLS samples is plotted in figure 6.12 (b). The values between parathesis represent the theoretical calculations of InAs/InAsSb bandgap (e-hh_1), where a qualitative agreement between theoretical and experimental can be observed. The integrated PL intensity as a function of laser excitation power in log scale is plotted in figure 6.12 (c). All samples exhibit similar β values, and therefore, it is reasonable to conclude that radiative recombination is the dominant process. It should be noted that the significant increase in the integrated intensity in SLS 4 is because this sample was grown recently to fit the study of InAs/InAsSb superlattice where a slightly different growth condition has been used. Despite this, the reduction in the PL intensity across the other samples can be explained by the Nextnano study. Increasing the thickness will reduce the overlap of electron and hole wavefunction, lowering the radiative recombination rate.

6.4.4 Temperature-dependent of varied PL with varying layers thickness

Temperature dependence of photoluminescence spectra under excitation density $\sim$ (4.25 mW/cm^2) for various structures is plotted in figure 6.13. The overall trend of PL spectra is described as a usual blue shift in the low-temperature region ranging from 10 to 2 meV followed by a usual redshift with increasing temperature following the known III-V behaviour.

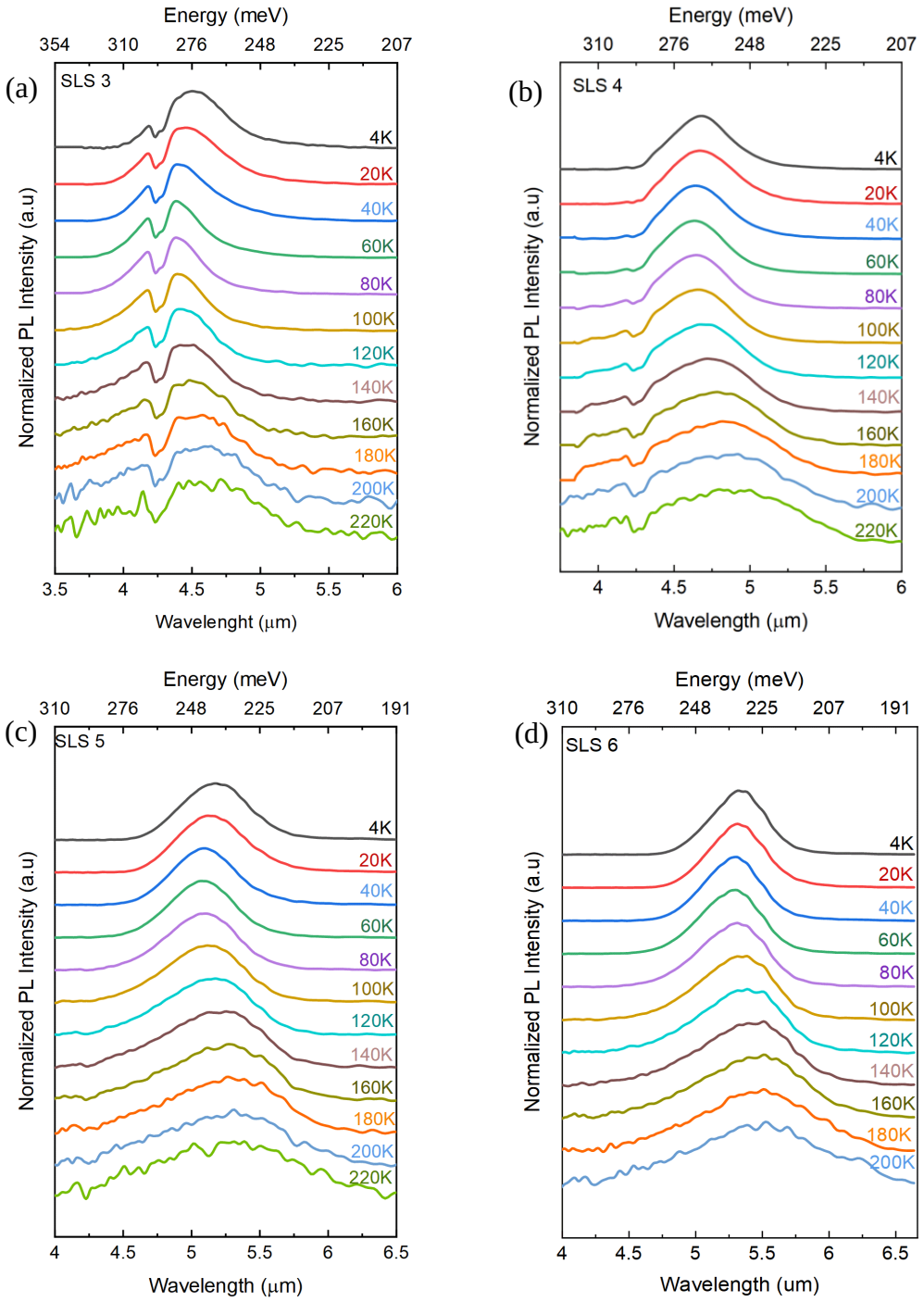

Figure 6.13: The temperature dependency of normalised PL spectra of period varied sample sets B. The effect of increasing period thickness is observed in the shifting PL spectra toward a longer wavelength.

The blue shift due to increasing the SLS temperature observed in sections 6.4.2 and 6.4.4 can be discussed in detail. Recent investigations have demonstrated the existence

of blue shift in the PL spectra in (InAs/GaSb, GaSb/GaAs) QW[131,132] and (InAs/GaSb, InAs/InAsSb) SLS[35,133]. Overall, these studies assumed the PL was due to a band to band transition and credited the blue shift in the peak position to the natural type-II QW joint density of state convolved with the thermal distribution of carriers[35,131–133]. Another proposed cause of the blue shift is carrier localisation due to compositional variation and layer width fluctuations[134–137]. This is supported by the explanation that regions, where compositions are slightly different produce spatial perturbations in the local potential. As a result, band tails in the density of state are formed, which also confine carriers to the lowest energy level in the low-temperature regions. Therefore, increasing temperature leads localised carriers to gain enough energy to escape into extended energy states resulting in a blueshift in the PL peak position. Further increases in the temperature lead the PL peak to follow the expected bandgap energy trend. Figure 6.14 shows the fit of the mean peak of the PL spectra according to Varshni law (equation 2.1). It can be seen a weak carrier localization of ~ 3 meV for SLS 4 – 6, however, the SLS 6 show a deep localization of nearly 10 meV. The carrier localization of all samples is broken at a temperature above 60 K due to increasing thermal energy and hence K_bT. If the localization is due to composition non-uniformity, that would indicate SLS 3 has substantially a bigger non-uniformity. Possibly there is a local area where Sb composition is exceeding 19 %. In addition, the effect of changing thickness is more obvious in the thinnest periods (SLS 3) since there is a short time between growing InAs and InAsSb layers. Recalling the band gap is mainly given by the offset of two materials and localization a way from band edge is very small and hence evidence on the rest of the samples (SLS 4 – 6). Table 6.4 presents the energy bandgap, PL blueshift, change in the peak position with respect to temperature, and Varshni fitting parament of various samples. It became evident that

superlattice structures demonstrate less temperature dependency than those bulk InAs and InSb materials. Despite the uncertainty associated with the SLS 3 sample due to carbon monoxide absorption affecting the PL spectra, all samples show comparable values with those previously reported for InAs/InAsSb on GaSb substrate[35].

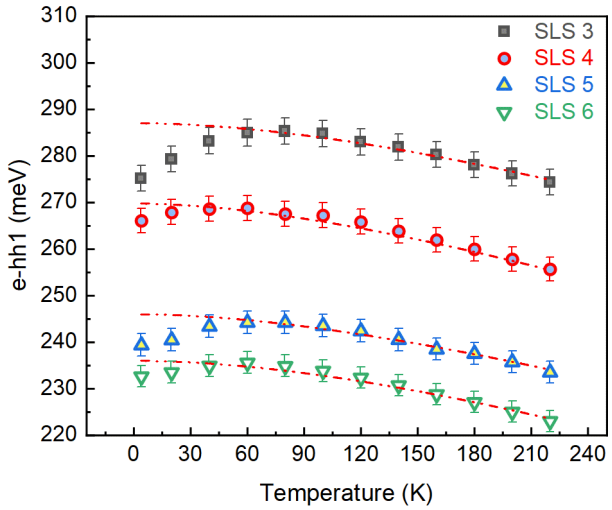

Figure 6.14: Temperature-dependent of PL spectra of sample set B obtained using excitation density of 4.25 mW/cm^2. The Varshni fitting is highlighted in dotted dash redline for various superlattice structures (sample set B).

Table 6.4 The calculated InAs/InAsSb superlattice bandgap of sample set B and measured PL peak position at 80 K. The blue shift of the superlattice is highlighted, and the change in the peak position with respect to increasing temperature. The Varshni fitting parameter is taken from the Gaussian fitting of the superlattice bandgap.

Sample	PL Bandgap at 80 K (meV)		PL Peak Blueshift 4 – 80 K (meV)	$\Delta\lambda/\Delta T$ 80 - 220 K (nm/K)	Varshni Fitting Parameters		
	exp.	sim.			$E_g(0)$ (meV)	α (meV/K)	β (K)
SLS 3	285	276	10	1.28	288	0.16	350
SLS 4	268	248	2	1.60	270	0.15	290
SLS 5	243	223	3	1.68	246	0.135	330
SLS 6	234	200	2	2.3	236	0.159	400

One major issue in the InAs/InAsSb material system grown on GaAs concerned the effect of strain on the quality of the grown epi-layer. Even though these samples are strained balanced on GaSb, non-avoidable strain-related issues arise from the GaAs/GaSb interface, which does not achieve perfect 100% strain relaxation. The SLS is designed for strain balance on the GaSb lattice constant, however, the GaSb to GaAs IMF interface is not perfect relaxing to the GaSb lattice constant. Reyner et al[138] demonstrate the characterization of GaSb/GaAs IMF interfaces using the XRD technique. It was concluded that the relaxation of the residual strain from IMF formation is only ~99.7 %. This result is comparable with these SLS samples where the relaxation is in the range of ~ 98.4 -99.7 %. Another issue is the lack of PL data above T > 220 K, which is a vital factor in comparing the Varshni fitting parameter with the literature[26,35,126]. In addition, the different growth techniques, and experimental conditions such as PL excitation density are important factors to consider.

The quenching of PL emission with increasing temperature is attributed to the reduction of radiative recombination associated with an increasing rate of non-radiative recombination, mainly the Auger process, which is strongly temperature-dependent, as will discuss in section 6.8.3.

6.5 Mid-infrared InAs/InAsSb SLS LEDs

To reach 5.7 µm wavelength for NH_3 application, SLS 4 sample was transferred into EL structure; in this section, the outline of band structure calculation, growth, optical and electrical characterisation is demonstrated.

6.5.1 Design and growth

The structure of SLS LEDs is illustrated in Figure 6.15(a). Two samples were grown by solid source MBE equipped with SUMO group III cells and valved cracker As_2 and Sb_2 sources on either n-type GaAs or GaSb substrates. Wafer preparation was introduced, including thermal cleaning in the outgas at 200 – 300^o C and oxide desorption steps. A thin buffer layer of the same binary as the substrate is deposited at a low growth rate of 1ML/s, isolating any surface contaminations on the substrate from the following epi-layers.

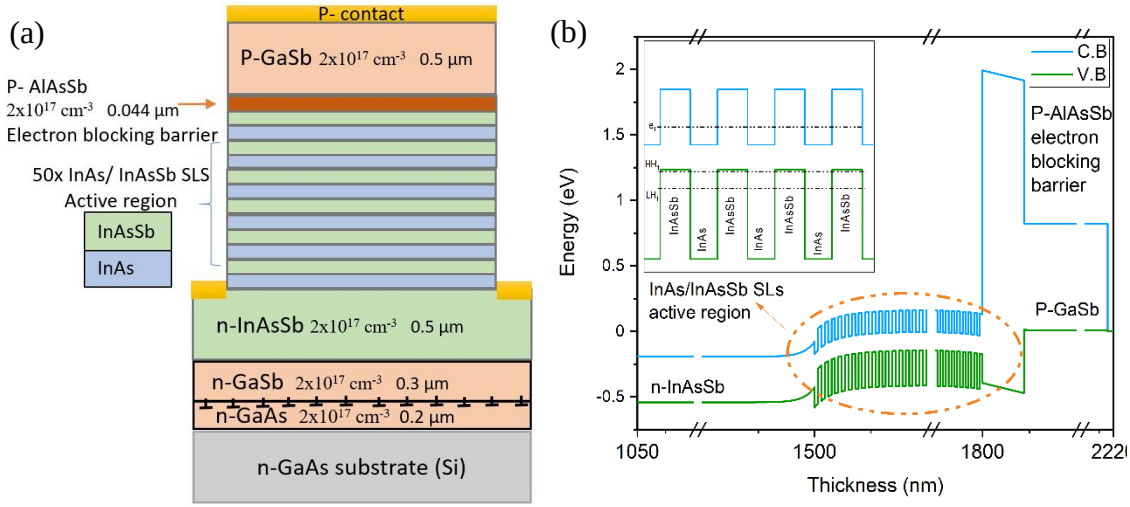

Figure 6.15: (a) A schematic of the LED structure continuing the InAs/InAsSb SLS active region grown on GaAs using an IMF array. For the sample grown on GaSb, the uppermost five layers were grown directly onto the substrate. (b) The energy band diagram of the structure was calculated using Nextnano.

To access III-Sb materials necessary for MWIR emission on the 5.65 Å GaAs substrate, a GaSb Interfacial Misfit array (IMF) was used to transition the lattice constant to 6.1 Å. A thin layer of n-doped GaSb was sandwiched between the substrates and a lattice-matched 0.5 µm n-type $InAs_{0.91}Sb_{0.09}$ contact layer. The dopant density was kept at $2 \times 10^{17}/cm^3$. The buffer layer was grown at 505°C, and the growth rate was ~1 ML/s. A 50 period (320 nm) of an InAs/InAsSb SLS not intentionally doped active region was

grown at 425 °C, while the growth rate was kept at 1.0 ML/s for both structures. For the active region, a 3 second Sb pre-deposition was used priority to growth InAsSb layer, followed by 10 seconds of As exposure in preparation for the InAs layer to reduce Sb segregation and obtain abrupt SLS interfaces for efficient SLS interfaces e-h recombination[93,139]. During the growth of InAs, the surface reconstruction was monitored using reflection high energy electron diffraction (RHEED). The RHEED pattern showed clear 1 x 3 indicating an efficient As-Sb exchange reaction which removes the excess Sb on the surface. The thicknesses of the strain balanced $InAs_{0.835}Sb_{0.165}$ SLS, and the InAs barrier was 3.0 and 3.4 nm, respectively. The electron blocking layer (EBL) was grown at substrate temperature approaching GaSb growth values 505°C consisting of 44 nm of a p-$AlAs_{0.08}Sb_{0.92}$ (Be doped = $2 \times 10^{17}/cm^3$) EBL was then grown above the active region. Finally, a 0.5 µm p-GaSb (Be = $2 \times 10^{17}/cm^3$) top contact layer was grown at 505°C. The structure was processed using standard photolithography methods, wet etching and evaporation deposition of Ti/Au contacts into 800µm square, mesa-etched LEDs, then mounted onto To-49 headers. Figure 6.15 (b) shows the calculated band structure and quantum-confined levels inside the InAsSb SLS. The bowing parameters used for the non-linear interpolation of the conduction and valence band energies were C_{CB} = +0.65eV and C_{VB} = -0.98eV as previously reported in our publication[140]. The energy band diagram of the SLS structure shows that the band alignment is type-II, as illustrated in the inset of Figure 6.15 (b), where the (e1-hh1) ground state transition occurs between the bottom of the InAs conduction band and the top of the InAsSb valence band.

6.5.2 Structural characterisation of InAs/InAsSb SLS LEDs

An ω - 2Θ scans were preform on GaAs and GaSb-based LED, as seen in figures 6.16 (a) and (b), respectively. Although finite levels of threading dislocations are expected

at GaAs/InAsSb interface, sharp satellite peaks and Pendellosung fringes seen in the HRXRD rocking curves in both LEDs samples indicate excellent growth quality.

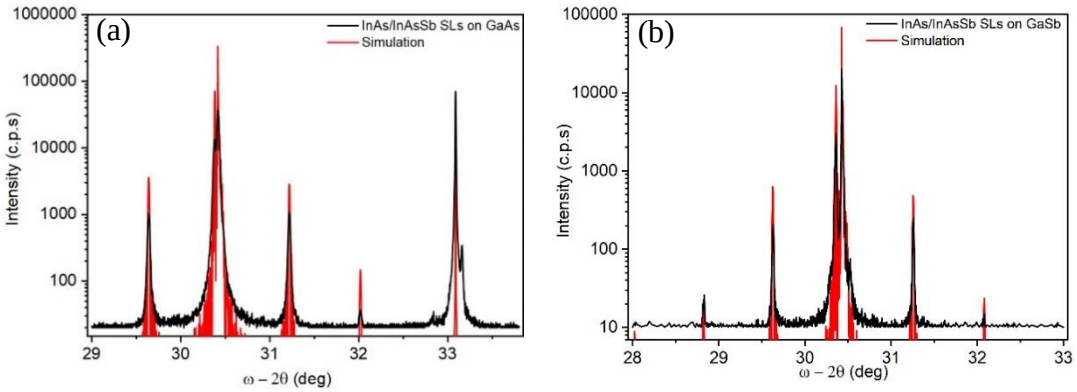

Figure 6.16: High-Resolution x-ray diffraction spectra obtained from the InAs/InAsSb SLs LED and corresponding simulation to determine the structure and composition of the two SLS samples grown on (a) GaAs and (b) GaSb substrates.

The FWHM of the zero-order SLS peaks is 91.08 arcsec (GaAs) and narrower 52 arcsec (GaSb). In comparison with similar structures grown on GaSb substrate, Steenbergen et al. [34] report that an increasing number of periods of SLS Influence the linewidth of SLS for high Sb contents. In addition, these results are less than those previously reported on InAs [20]. The narrowed FWHM of the satellite peaks of SLS indicting high-quality crystal materials confirmed by bright electroluminescence spectra at room temperature. The values of the InAs/InAsSb SLS thickness and structure period were calculated by simulation of the XRD rocking curves using Bede software. As indicated in figures 6.16 (a) and (b), the best fitting of the experimental curve was ~3/3.4 nm of epi-layer thickness, while the Sb composition remained the same at 16.5 % for both SLs LED.

6.5.3 Light-Current characterisation (I-V)

The I-V behaviour of GaSb and GaAs-based superlattice LEDs are investigated at room temperature. Number of testing were operated to determine which mesa-processed

device has a lower resistance. The LED device that features residual post-process chemicals has a higher resistance than those with a clean process, as seen in figure 6.17. Therefore, a flavour set of the LED device was selected for the I-V study. At 77 K, the series resistance of GaAs-based LED was almost five orders of magnitude higher than that on GaSb (227 Ω GaAs compared to 41 Ω GaSb). As these diodes reached room temperature, the resistance was significantly lower and both diodes are similar in resistance ~ 11 Ω (see figure 6.18). Temperature increases cause electrons in the valence band to gain enough thermal energy to move to the conduction band resulting in a significant increase in the number of free carriers. Therefore, conductivity increases and resistivity decreases. Notably, the GaSb diode shows unusual behaviour on the reverse bias due to the high leakage current found on this device. This shows device optimization is necessary and would be the subject of future research work. The diode ideality factor η was fitting according to equation 2.55 and yielded values of $\eta_{GaAs} = 1 \pm 0.36$ and $\eta_{GaSb} = 1.01 \pm 0.27$ at room temperature.

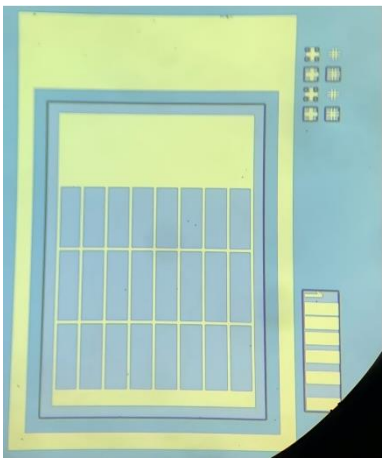

Figure 6.17: Top view of the processed rectangular ~ 0.8 x 0.8 mm mesa etched GaAs-based LED. The total emitting area is estimated $\sim 0.71\ mm^2$.

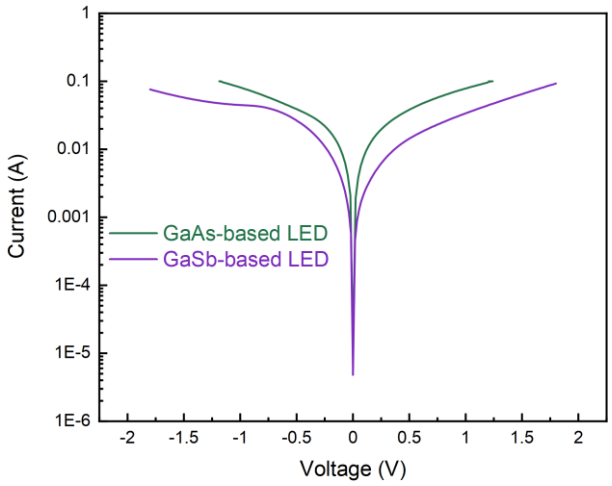

Figure 6.18: The I-V curves of GaAs and GaSb-based superlattice LED on a semi-logarithmic scale measured at room temperature.

6.5.3.1 Transfer length measurements (TLM)

To assist the limitation of electron transport in the InAs/InAsSb active region, the transmission line measurements (TLM) method was carryout according to early demonstration[141]. In general, A metal-to-semiconductor Ohmic contact demonstrates a linear I–V characteristic with low contact resistance. There are two types of ohmic contacts, vertical current flow (VCF) and Lateral current flow contacts (LCF). Figure 6.19 illustrates the TLM method. In the VCF method, the current spreads perpendicular to the contact plane and hence resistance is measured between the contact and the top layer (p-type). However, in LCF measurement, the current flows parallel to the contact plane (trough the n-type layer).

It is possible to account for current flows across the entire contact area R_c according to[142,143]:

$$R_{Total} = 2R_c + R_{semi} = 2R_c + \frac{R_{sheet}S}{W_c} \qquad (6.1)$$

Where R_c is the contact resistance (meta-semiconductor interface), R_{semi} is the resistance of the semiconductor, R_{sheet} is the sheet resistance, S is the separation length between the contacts and W_c is the width of the current path.

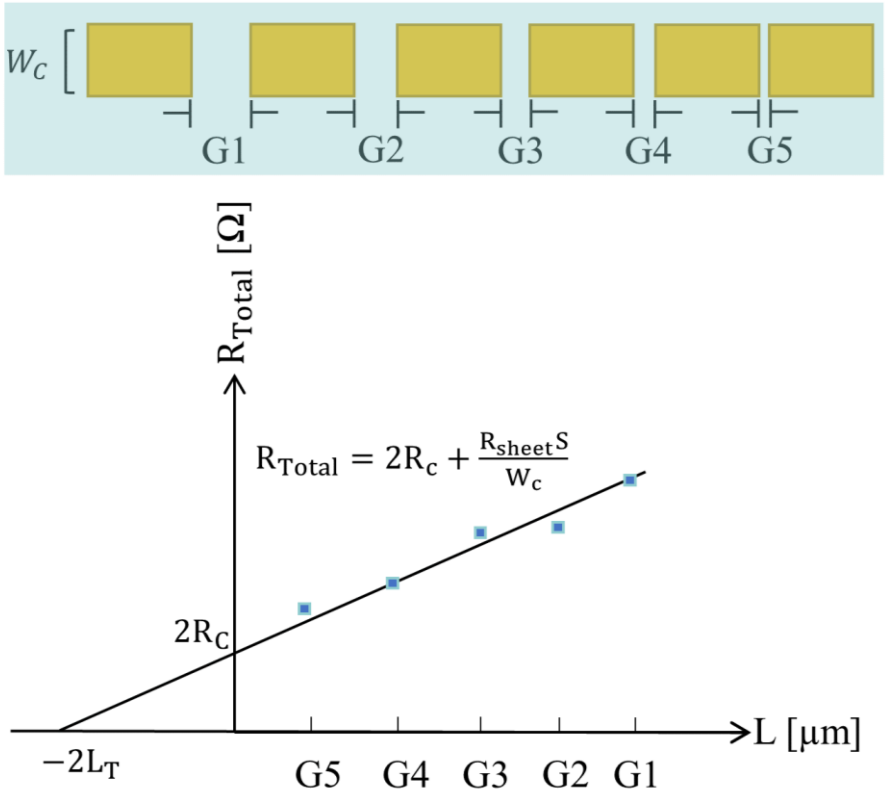

Figure 6.19: A diagram demonstrates the transmission line method and numerical calculation used.

In the used square mesa mask, the TLM pads are of equal size in this case (50 wide and 130 long), which are separated from each other at varying separation distances (G_1 = 5 µm, G_2 = 10 µm, G_3 = 20 µm, G_4 = 30 µm, and G_5 = 50 µm). Probes were placed in each TLM pad and the corresponding I-V curve is obtained at room temperature, as shown in figures 6.20 (a) and (c). The resistance was determined for each TLM pad pair (VCF) from the higher voltage range. In figures, 6.20 (b) and (d), the specific contact resistance can be estimated by extrapolating to the y-intercept which equals ($2R_c$). The

contact resistance is higher than expected at 22 Ω (GaSb-LED) and 28 Ω (GaAs-LED) which could be due to the doping of the p-type layer being high. However, these results indicate that the resistance between the p-type (p-GaSb) and contacts are similar indicating that transferring the active region into a different substrate has a slight effect on the contact resistance. In addition, the specific contact resistance ρ_c can be estimated by multiplying the width of the current path W_c and transfer length (L_T) according to[141]:

$$\rho_c = R_c W_c L_T \qquad (6.2)$$

Therefore, the specific contact resistance is 1.43×10^{-3} Ω.cm^2 (GaSb-LED) and similarly $1..82 \times 10^{-3}$ Ω.cm^2 (GaAs-LED). These values are two orders of magnitude higher than typical ρ_c value for III-V arsenides/antimonides materials system. Therefore, it is possible to conclude that some of the limitations of these diodes are observed by contact resistance.

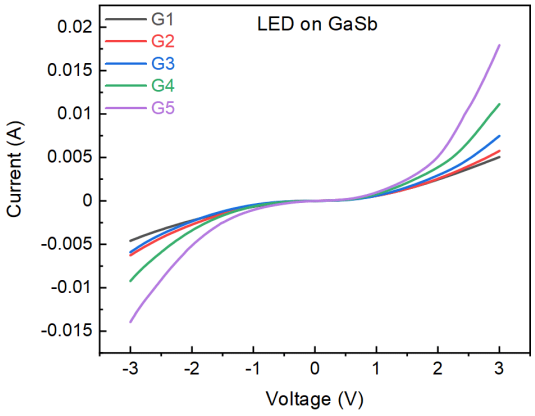

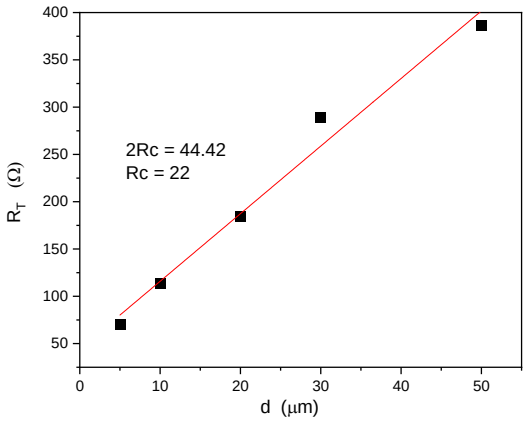

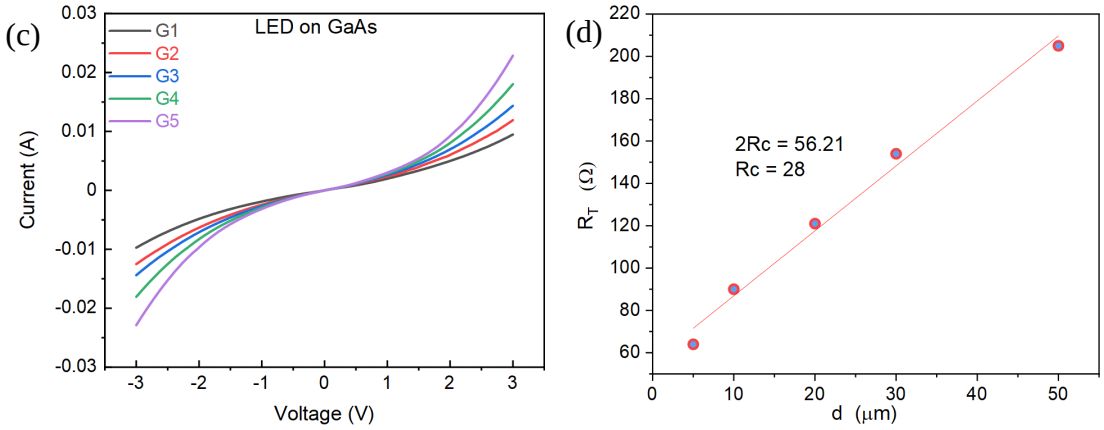

Figure 6.20:The I-V curves of TLM-VCF of (a) GaSb and (c) GaAs based superlattice LED. The corresponding determination of contact resistance is shown in black dot lines in (b) and (d) where the redline represents straight line fitting.

6.5.4 Electroluminescence comparison of InAs/InAsSb SLS LEDs grown GaAs and GaSb substrates

Electroluminescence spectra were taken according to the setup described in section 4.5. In this section, investigates of varying substrate implications on the optical properties of T2SL InAs/InAsSb LEDs.

6.5.4.1 Temperature-dependent of the electroluminescence spectra

Figure 6.21 shows the 4 K electroluminescence emission spectra of GaSb-based SLS LED obtained at I = 40 – 150 mA, 30 % duty cycle, and 1 kHz. A Gaussian deconvolution shows a single symmetric peak observed at 253 meV~ 4.89 μm (GaAs) and slightly at higher energy 259 meV~ 4.78 μm (GaSb) at low currents injection (I = 40mA). As the current increased to (I = 150mA), the mean peak blue shifted to 260 meV~ 4.76 μm (GaAs) 266 meV~ 4.65 μm (GaSb). The blue shift of both diodes at 4 K was similar ~8 meV which is also comparable to the 5 meV shift observed in the PL sample (SLS 4).

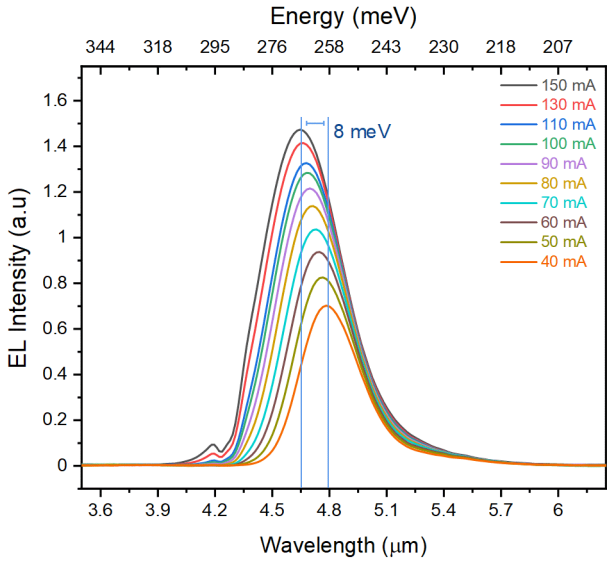

Figure 6.21: The 4 K EL spectra of GaSb-based SLS LEDs at variable Injection current demonstrating the blue shift trend of 8 meV.

EL emission spectra from GaAs and GaSb-based SLL LEDs at various temperatures are shown in figures 6.22 (a) and (b). Over the temperature range 4-300K, both devices show similar trends including wavelength shifting toward long wavelength and broader linewidth with increasing temperature as expected

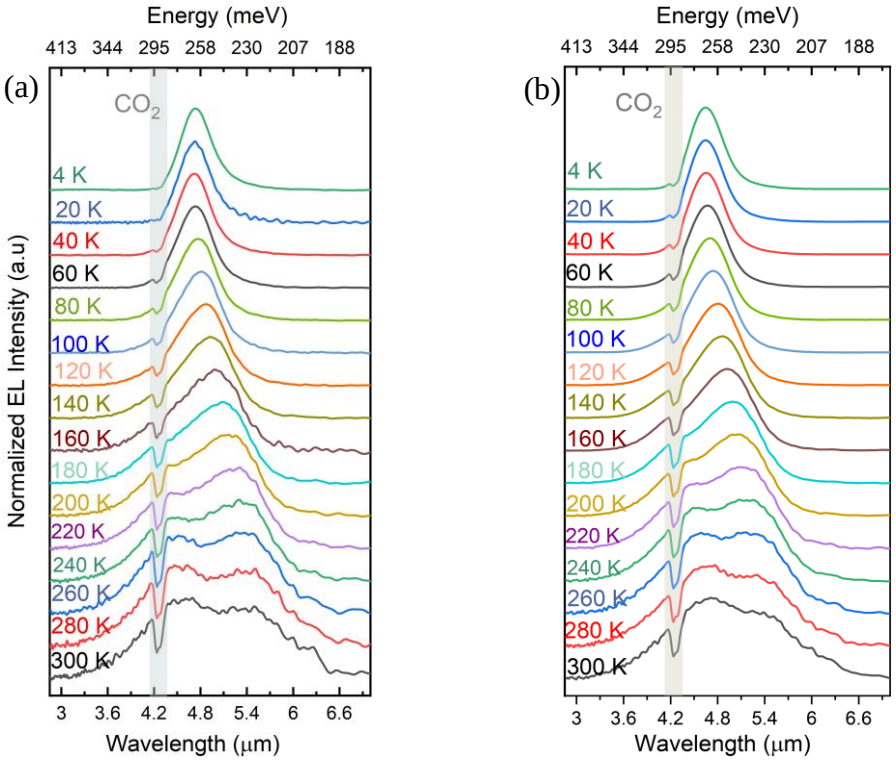

Figure 6.22 Temperature-dependent of normalised electroluminescence spectra of the (a)GaAs and (b) GaSb-based superlattice LED. The operation condition were 140 mA, 30 % duty cycle, and 1 kHz.

A possible explanation for this behaviour is the characteristic of type II QWs and is explained by localised holes in the InAsSb quantum well-attracting electrons from the adjacent InAs barrier due to Coulomb interaction [94]. This results in an approximately triangular potential well for electrons close to the QW interfaces which improves the electron-hole wavefunction overlap[144]. An increase in the EL intensity L will raise the confining potential and consequently the electron quantisation energy *E*, with a typical $\Delta E \sim L^{1/3}$ behaviour[131]. The EL spectra may be interpreted as transitions originating from the InAs conduction band to the heavy hole and light hole states in the InAsSb layer e-hh_1. The experimental value of 259 ± 2 meV corresponds to the intercepts for the respective e-hh_1 transition which is in good agreement with the theoretical value of 267 meV obtained from single band effective mass using Nextnano software. As the temperature increase, the peak from e-hh_1 become less pronounced and at about ~ T = 180K, a low energy peak from originated from e-hh_2 transition appeared in the shoulder of both devices and become dominant in the room temperature. The energy separation between these peaks ranges from 40 – 47 meV. The temperature quenching of the mean peak intensity for both LEDs are similar, with a slightly high rate on the GaSb-based LED (x50 GaAs compared to x81 GaSb) due to the higher Auger rate found on this device. Besides, the FWHM of the peak was also similar in both LEDs and slightly narrow in GaSb-based LED ~14 nm different in width.

Over the measured temperature range (4 – 300 K), it was found that the intensity of the mean peak e-hh_1 decreased steadily as thermal energy increased as indicated in figure 6.23(a). The peak intensity of GaAs-based LED quenched by only factor of ~ 30 as a

(a)

result of the carrier confinements compared to much higher quenching factor found on the GaSb-based SLS LED (~ 162).

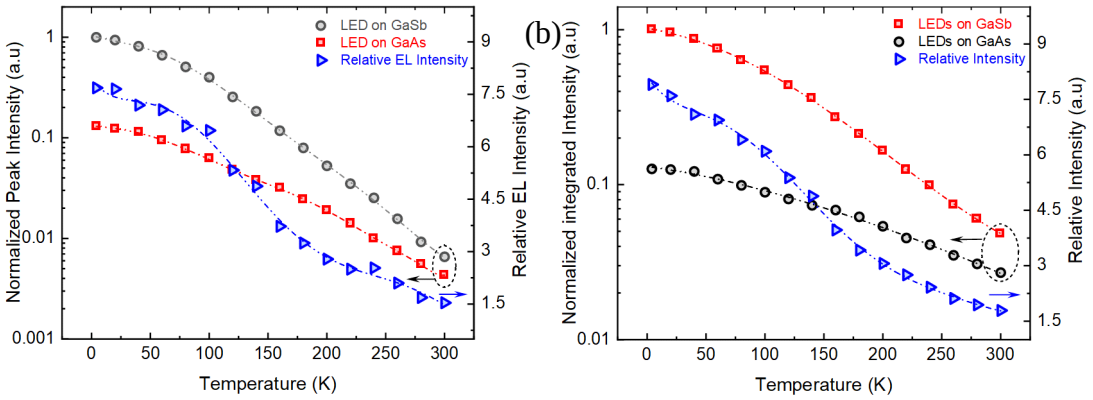

Figure 6.23: (a) The mean peak intensity (e-hh1) normalized as function of temperature for GaAs (red) and GaSb (dark grey) LEDs. (b) The integrated intensity of these LEDs and the relative intensity is illustrated.

Comparing the two EL spectra, there is a slight decrease in the relative intensity between GaAs and GaSb-based LEDs of 7x at 4 K and reduced to 1.5 times at room temperature, as indicated in the blue dash-dotted line in figure 6.23(a). Similar behaviour was also observed in the integrated intensity, as shown in figure 6.23 (b). Interestingly, the integrated intensity and hence the output power of GaAs-based LED only drop by a factor of 4 compared to 20 found on the GaSb-based LED as a result of increasing temperature from 4 to 300 K. In general, the reduction in the intensity with increasing temperature is potentially due to thermal loss of carrier out of the active region. The type-II band offset reduces the electron-hole wave function overlap and the matrix element for radiative recombination, which is an advantage in reducing unwanted processes, as will discuss later.

To determine the dominated quenching process in each device, the integrated intensity of EL emission was plotted against $1/k_bT$ where k_b is Boltzmann constant, and T is temperature. It is possible to determine the activation energy using (equation 5.2), and

the result is shown in Figure 6.24(a). The activation energy for GaAs-based LED is 20 meV and 14 meV for GaSb-based LED.

Using linear interpolation for the bulk effective carrier masses, the activation energy of the CHCC and CHSH processes in $InAs_{0-835}Sb_{0.165}$ were calculated to be 12 meV and 239 meV respectively, to provide a starting point for comparison. This probably indicates the CHCC remain to dominant process in the superlattice however, a calculation for the CHCC activation energy in the SLS is a significate challenge and could be considered in future research work. The electron effective mass of SLS is increasing more substantial compared to the bulk and could be the reason for the 2 meV difference between the calculated and experimental Auger activation energy.

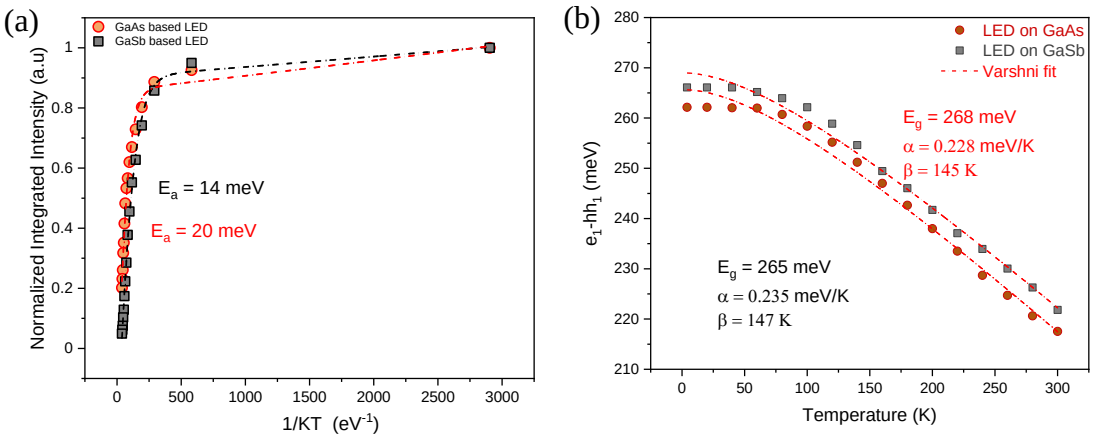

Figure 6.24: (a) The normalised integrated intensity against 1/KT where the dash-dotted lines represent Arrhenius fitting function intensity resulting in activation energy of 20 meV and 14 meV for the GaAs, and GaSb-based SLS LED, respectively. (b) Temperature dependence of the electroluminescence emission peak energy obtained for the InAs/InAsSb SLS LED integrated on GaAs and GaSb substrates. The dash-dotted lines represent the Varshni fitting of the experimental data, and corresponding fitting parameters are highlighted in black colour (GaSb- based LED) and red colour.

The redshift trend observed in EL spectra with increasing temperature is expected for III-V materials. The temperature dependency of the superlattice bandgap is taken from

the preliminary analysis of EL spectra and fitted according to equation 5.2. The result of the correlational study can be compared in Figure 6.24 (b), where an excellent quantitative fit is observed for both diodes. There was a significant positive correlation between Varshni fitting paraments and those reported on similar structures

6.5.4.2 Duty cycle dependent on the electroluminescence spectra

The effect of the duty cycle on the EL emission spectra of the GaAs-based SLS LED is demonstrated using a 140 mA injunction current and repetition rate of 1 kHz as illustrated in figures 6.25 (a) and (c) measured at 4 K and 300 K respectively. As the duty cycle increases from 10% to 50%, the peak position is blue-shifted from 4.81 µm to 4.74 µm (4 K) and then red-shifted from 5.60 µm to 5.68 µm (300 K). The blue shift associated with low temperature may attribute to the increasing rate of non-radiative recombination such as SRH. In contrast to this trend, a red shift observed at high temperatures is suggesting Auger recombination is becoming important. The influence of duty cycle changes on the Integrated intensity at 4 K is also indicated in figure 6.25 (b) where GaAs-based SLS LED was reported to increase by a factor of ∼3.8 and similarly, ∼ 3.2 for the GaSb-based SLS LED. As the temperature increased to 300 K (see figure 6.25 (d)) both diodes are influenced by joule heating where the integrated intensity increased by a factor of ∼ 3.7 (GaAs) and ∼ 2.9 (GaSb). Inspection of figures 6.25 (b) and (c) reveals that the EL spectra of both SLS devices started to saturate at duty cycle > ∼ 30% which suggests a unique optimal operation condition in all temperature ranges (4 – 300 K).

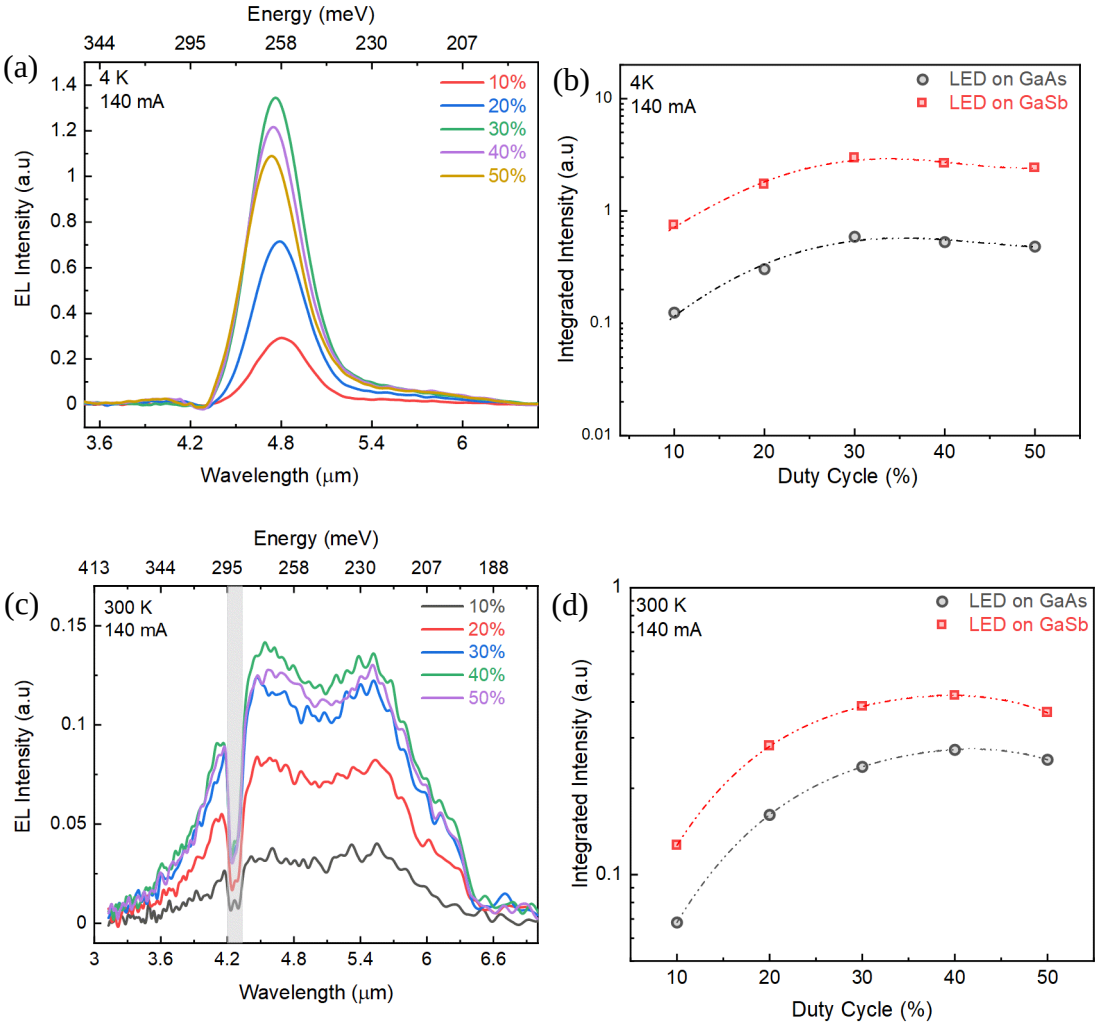

Figure 6.25: Duty cycle dependence of the electroluminescence emission spectra of the GaAs-based SLS LED at (a) 4 K and (c) 300 K. The comparison of the integrated intensity as a function of the duty cycle of the GaSb-based SLS LED (red square) and GaAs based SLS LED (black circle) measured at (b) 4 K and (d) 300 K.

6.5.4.3 Light-current dependent at 4 and 300 K

To evaluate the device performance and suitability for room-temperature operation, the current dependence of the EL for InAsSb/InAs SLS active region LED based on GaAs, and GaSb substrate was investigated. The integrated intensity was normalised, and relative intensity was recorded in figure 6.26 (a). In general, the integrated intensity increases on increasing current across all devices, although the details of the trend over

the entire current range significantly between devices. For example, the GaSb-based device shows a sharp rise in the integrated intensity at approximately 40 mA, becoming less pronounced at high current and completely absent in the GaAs-based device. At high current (I => 90 mA), the emission from both devices has a sublinear dependence on current, suggesting that the Auger process is important.

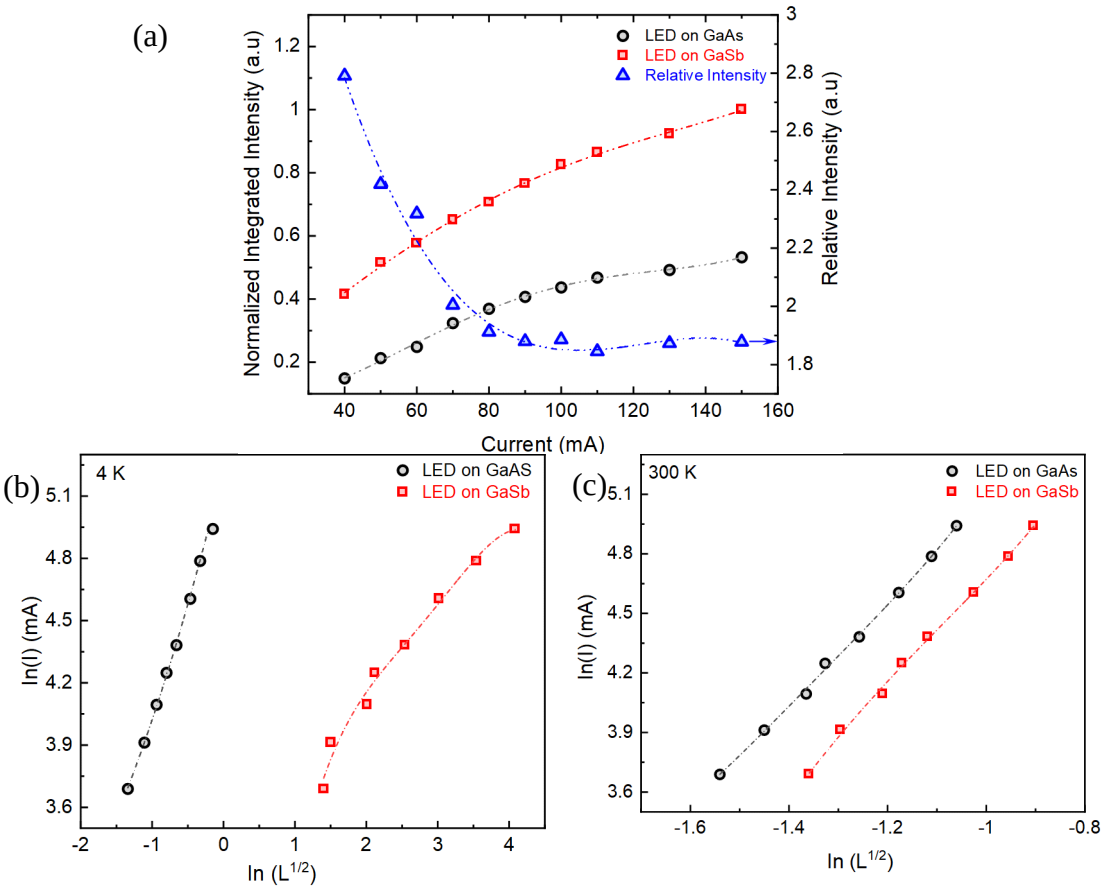

Figure 6.26: (a) Room temperature electroluminescence emission spectra observed from the InAs/InAsSb SLS LED using different injection currents. The In (I) vs In ($L^{1/2}$) at (b)4 K and (c) 300 K over the entire current range (40 – 140 mA, 30 % duty cycle) for GaAs and GaSb-based SLS LEDs, respectively

Interestingly, at low current (I = 40mA), the difference in the output power (integrated intensity) between these LEDs was only ~2.8, and this slightly decreased to ~1.9 as injection current approached the highest value of (I = 150mA). In addition, the change

in the wavelength with respect to increasing the injection current is small ~ 30nm and was found to be similar in both devices. In the absence of a leakage path $I_{leakage}$ and adopt the analysis given by Sweeney et al. [145], the current flow through device assuming Boltzmann statistic may writing as :

$$I = eV(An + Bn^2 + Cn^3) \qquad (6.3)$$

Where e is the electronic charge, V is the volume of the active region, and n is the carrier density. A, B and C are the coefficients refereeing to SRH, radiative and Auger recombination, respectively. SRH recombination occurs when electron and hole recombination via deep levels within bandgap through defects or impurities states which is directly proportional to the carrier concentration. In the radiative recombination, the electron from the conduction band recombination with the hole from the valence band, releasing photons leading to n^2 dependency. The injected carrier concentration in the active region can be estimated from:

$$n = \frac{J\,\tau}{e\,d} \qquad (6.4)$$

Where J is the current density, τ is the carrier lifetime and was approximated to InAs value of $\sim 3\text{x}10^{-6}\ sec$, e is the electron charge, and d is the diffusion length equal to the size of the active region $\approx$ 0.325 µm. At an injection current of 150 mA, the carrier concentration was estimated to be $\sim 1.2\text{x}10^{19}\text{cm}^{-3}$. Auger processes are dependent on carrier concentration and occur when the energy released by the recombination of an electron and hole is not used to generate a photon but to excite another carrier; hence the n^3 dependency. The measured integrated spontaneous emission L is proportional to the radiative current, and thus$\propto \text{Bn}^2$. Hence if B is independent of $\text{n} \propto \text{L}^{1/2}$ which follows that $\text{I} \propto (\text{L}^{1/2^{\text{Z}}})$. Taking the natural logarithm of both sides yields ln(I) =

$Z \ln(L^{1/2})$, the value of Z may be obtained from the gradient of the plot of ln (I) versus $\ln(L^{1/2})$. The z value of unity if the dominated recombination is SRH, two if radiative recombination, and three if Auger is the dominant mechanism. Intermediate values indicate a mix of recombination. Figure 6.26 (b) and (c), show plot of ln(I) versus $\ln(L^{1/2})$ at low (4 K) and high temperature (300 K). The gradient and, hence Z changes considerably over the entire current range. At the low currents region (40- 60 mA), the Z value for room temperature obtained from GaAs-based LED was 2.36, indicating nearly radiative recombination. In contrast, the Z value falls monotonically with decreasing temperature to 4 K to 1.02, suggesting that SRH becomes increasingly essential. Z value less than one means trapping minority carriers at defects [69,146] However, this trend was not observed in GaSb-based devices, where the Z value was obtained to be 2.3 at 300 K and slightly decreased at 4 K to 1.87, suggesting that the radiative process dominated under these conditions. At the intermediate currents region (70 – 100mA), both devices show similar Z values of 2.58 (GaAs) and (2.43) GaSb at 300 K, suggesting that both radiative and Auger processes are important in this current's region. However, at T = 4 K, the GaSb device shows pure radiative recombination while the GaAs device show value of 1.16, Indicating SRH is a significant process. At the high current region (110-140 mA), both devices are influenced by the Auger process and hence Z values of 2.77 (GaAs) and 2.66 (GaSb), which agrees with the result presented in Figure 6.26(a) showing relative integrated intensity as low as 1.8 times.

Interestingly, at 4 K, the Z value of 2.17 (GaSb) suggests radiative recombination is still dominated at the high currents regime, while 1.42 (GaAs) shows the influence of SRH and radiative recombination. These results agree with the integrated intensity of EL spectra quenching with the temperature shown in Figure 6.23 (b). The temperature dependence of Auger coefficients C in equation 6.3 is given by:

$$C = C_0 e^{-E_a/KT} \qquad (6.5)$$

Where is C_0 constant and E_a is the activation energy. Hence, due to the nature of Type-II transitions and since the electron and hole are localised in a different place in the heterojunction thus, the Auger recombination is suppressed, and the coefficients C is also minimised.

6.5.5 LED output power measurements

The output power of SLS-LED was measured using Thorlabs power meter PM100D instrument at room temperature. Under quasi-continuous drive conditions (100mA, 50% duty cycle, and 1kHz), the resulted output power from GaSb and GaAs SLS-LED was determined as 175.22 and 129.3 µW, respectively, corresponding to external quantum efficiencies (EQE) of 0.08 % for GaSb SLS LED and 0.05% for GaAs LED which are x 3 higher than reported EQE on InSb/AlInSb MQW on similar wavelength[71] and x 8 higher than bulk InAsSb[74]. In addition, the internal quantum efficiency IQE can be estimated to be 5.7 % and-3.5 % for GaSb and GaAs-based SLS LED respectively. These values are 3x higher than previous InAs/InAsSb SLS LED reported in our laboratory[98]. As indicated in figure 6.27, the emittances are plotted as a function of forwarding bias current. The output of GaAs SLS LED turnover at currents above ~80 mA, whereas the output of GaSb SLS LED shows a superliner dependency on current. According to figure 6.26(c), the dominated recombination mechanism at high currents is the Auger process, namely CHCC, which also influences the output power and hence limiting factor in these SLS LED. Nevertheless, the emittance value is slightly higher than reported on InSb/AlInSb material system [65,71,73,147]. However, direct comparison on InAs/InAsSb is challenging due to the lack of LEDs

operated at $\lambda \geq 5.5$ µm. Table 6.5 highlight the key differences in the device performance of InAs/InAsSb SLS on GaAs and GaSb substrates.

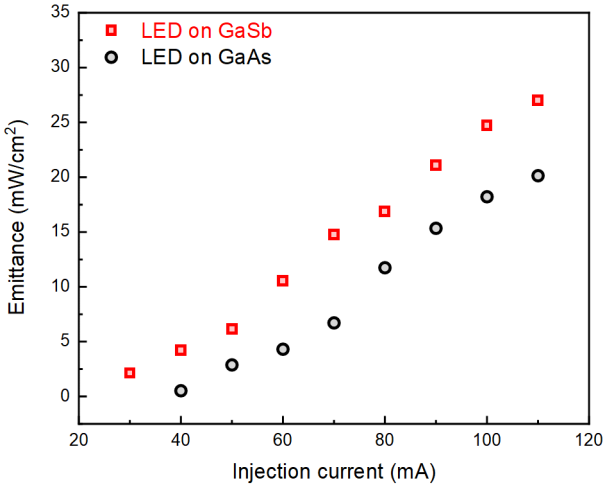

Figure 6.27: The measured emittance as a function of injunction current at room temperature for GaSb (black colour) and GaAs (red colour) based SLS LED.

Table 6.5: Optical and electrical properties of InAs/InAsSb SLS LED integrated on GaAs and GaSb

	LED on GaAs	LED on GaSb
Wavelength (µm)	5.68 ± 0.02	5.61± 0.03
Power (µW) (I =100mA, DC=30%,f = 1kHz)	129	175
EQE (%)	0.05	0.08
Diode Ideality factor (a.u)	1 ± 0.36	1.01 ± 0.27
FWHM (µm)	~ 1.8	
The shift in Peak Position (nm/K)	4	3
Temperature Quenching of Integrated EL Intensity (a.u)	4	20
EL Characteristic Temperature (K)	107	84

Chapter 7: Conclusion and Future work

7.1 Conclusion

This thesis has reported theoretical and experimental study of InAsSb-based mid-infrared semiconductor components for two various applications. Firstly, exploiting type-I InAsSb/AlInAs multi quantum wells (MQWs) heterostructures integrated on GaAs and Si substrates for methane application. Secondly, the novel use of InAs/InAsSb strained layer superlattice (SLS) grown on GaAs and GaSb substrates for ammonia applications.

The comparison of type I MQWs and type II SLS emitters is interesting because it considers varying electron-hole wavefunction overlaps and allows the potential benefit of the type II structure to be considered. A reduction in Auger recombination was expected in the type II SLS, but with the possible side effect of reduced radiative recombination rate. SLS system with matched versus mismatched substrates showed similar optical properties at room temperature indicating smooth transitions in the active region.

7.1.1 Type-I InAsSb/AlInAs multi-quantum well LEDs

Type-I InAsSb/AlInAs multi-quantum wells have been carefully studied and shown to be a promising candidate for mid-infrared applications such as methane detection. Prior to this work, photoluminescence of InAsSb/AlInAs quantum wells was reported emitting up to 3.3 μm at room temperature. This thesis demonstrates the successful design, growth, fabrication, and characterisation of LED structures integrated on GaAs

and Si wafers. The use of virtual substrate (AlInAs) allows the use of Al in the barrier and keeps it within the strain limit, enabling access to a short wavelength range while increasing the confinement energy and therefore higher radiative rate. The principal achievements of this work are highlighted as follows:

- Bright room-temperature mid-infrared electroluminescence was achieved from InAsSb/AlInAs multi-quantum wells light-emitting diodes on GaAs and Si substrates, at $\lambda \approx 3.3\mu m$.
- Higher external quantum efficiency was achieved at high currents from the Si-based LED due to the superior thermal conductivity of the wafer.
- Analysis of temperature-dependent electroluminescence spectra to reveal activation energies and Varshni parameters.

A theoretical study using Nextnano software was carried out to examine band structure, transition energy and wavefunction overlap. The theoretical results suggest that a deep well corresponding to a large band offset can achieve $\lambda = 3.04\ \mu m$ (4 K). This also supports the main advantage of type-I band alignment, where the calculated wave function overlap of electron and heavy hole states is $\approx 80\ \%$.

Samples grown by MBE were examined using x-ray diffraction (HRXRD) and atomic force microscopy (AFM). The HRXRD study indicated a strong, intense multi-quantum well satellite peak for the GaAs sample, compared to that for Si. A simulation of XRD data showed that the alloy contents in both well and barrier were the same, indicating a good translation of the active region to the Si wafer. The quality of the growth of the Si sample is good and strain shift is comparable with other recent work on bulk InAsSb (Sb = 9 %) on Si. The AFM study showed that the GaAs sample has a smoother surface, which indicates quality material.

4 K photoluminescence spectra were recognised as originating from recombination between the first confined electron and heavy hole states in the InAsSb QW, which agrees with the theoretical study. The 9 meV shift in the peak position for the Si substrate sample, compared to that on the GaAs substrate, is interpreted as a strain-induced band shift which is consisting of early work on bulk material.

LEDs containing five $InAs_{0.915}Sb_{0.085}/Al_{0.122}In_{0.878}As$ multi-quantum wells and a 30 nm $Al_{0.24}In_{0.76}As$ electron blocking barrier were successfully fabricated on GaAs and Si wafers using standard photolithography and wet chemical etching. Electroluminescence emissions from the two LEDs devices were demonstrated at various temperatures using 700 mA quasi-cw excitation at 1kHz and 10 % duty cycle.

The EL emission spectra of both LEDs confirm the same e-hh1 transition energy found in PL measurements. Analysing the temperature dependency indicates that CHCC Auger recombination is the limitation of these devices as expected for Mid-IR type-I LEDs.

The light output power was determined, and to eliminate the effect of Joule heating, the devices were tested using a 1% duty cycle at a frequency of 1 kHz and injection currents up to 1.5 A. Even though the Si-based LED has a higher defect density, the output power measured at room temperature is significantly stronger than that obtained for the GaAs-based LED when the injected current is higher than 1A, due to the improved thermal conductivity of the substrate. These results suggest that further reduction of the defect density present in the InAsSb/InAlAs MQWs LED integrated onto Si could enable the development of the next-generation, cost-effective sensing and monitoring systems light sources.

7.1.2 Type-II InAs/InAsSb strained layer superlattice LEDs

InAs/InAsSb T2SLs have been carefully designed, fabricated, and investigated, demonstrating a promising material system for mid-infrared light-emitting diodes. This work was done following the previous photodetector-focused work at Lancaster University and developed the InAs/InAsSb superlattice active region including integrating it into LEDs using GaAs and GaSb wafers.

The band structure simulation predicts the emission wavelength while highlighting the effects of tailoring the antimony content and period thickness in the superlattice to optimise the overlap of electron and hole wavefunction and ensure a high rate of radiative recombination.

Two sets of samples containing 100 periods of InAs/InAsSb were grown on a lattice mismatched GaAs substrate by molecular beam epitaxy. The growth of the strained-balanced superlattice structure was achieved using a thick GaSb buffer layer. The material quality was investigated using HRXRD revealing excellent crystalline quality despite broad linewidth observed in one structure containing a thick period. This specific sample was assumed to be compromised by a poor IMF interface.

The first set of PL samples (sample set A) demonstrated the effect of increasing the antimony content from 14.5 to 16.3 %: the peak energy redshifted from 255 meV to 243 meV and the peak intensity decreased by approximately six times. This was primarily due to a reduction in the electron and hole wavefunction overlap consistent with the theoretical calculation. The second set (sample set B) exhibits the effect of increasing superlattice periods from 4.24 nm to 13.9 nm, whereas antimony content remained at

~ 17.5 %. Interestingly, as period thickness increased, the energy peak also shifted from 271 meV to 230 meV, due to a reduction in the miniband confinement energy modelled correctly by Nextnano. However, simulations predict an associated reduction in the e - h overlap from 45% to 30%. This was attributed to reduced optical matrix elements due to spatially indirect transition between electron and hole which is expected to reduce both Auger (desirable) and the radiative rate (undesirable). At low temperature (T = 4 K), a blue shift of the InAs/InAsSb active region was observed with increasing laser excitation power attributed to the band filling effect. It was observed that the blue shift increased with increasing superlattice thickness from 6 to 11 meV which is comparable with that observed in the MQWs (12 meV). Analysis of temperature-dependent PL emission spectra shows a carrier localisation behaviour below 80 K, resulting in a blue shift of ~10 meV before the usual redshift behaviour with increasing temperature.

Following the PL study, two *p-n* diodes containing type-II strained-layer superlattice $InAs_{(1-x)}Sb_{(x)}$ / InAs active region were grown on native GaSb and cost-effective GaAs substrates and fabricated into LEDs. HRXRD examination demonstrated excellent growth quality as the InAsSb/InAs SLS peaks are sharp and narrow. Mid-infrared electroluminescence was obtained at various temperatures using a 140 mA quasi-cw excitation, 30 % duty cycle at 1 kHz. Simulation results indicated the main peak of EL spectra is due to an e-hh_1 transition of 267 meV, which is in excellent agreement with the experimental value of 266 meV. Both LEDs exhibited bright EL emission over the 4 – 300 K temperature range, and the emission wavelength was extended to ~5.7 μm. Although significant thermal quenching was observed, counterintuitively the GaSb-based LED was influenced by a greater reduction of radiative rate (20 times compared

to 4 times for the GaAs-based LED). The temperature dependent EL emission spectra show that the thermal holes escaping from the minibands are the limiting process in these prototype LEDs. Despite this, these LEDs demonstrated output power of ~175 and 129 μW correspond to IQE of 0.08 and 0.05% (on the GaSb and GaAs substrates respectively). The effect of the duty cycle on the EL spectra was observed to blueshifted the peak position at 4 K due to the presence of SRH centres. A contrast behaviour was observed at 300 K where the peak redshift to longer wavelength due to joule heating effect which agrees with the previous report on the MQWs RCLED structure. An investigation of the dominating recombination mechanism at room temperature reveals that radiative recombination is most likely to dominate in the low current region. However, at the high current region where LEDs operated, the dominated recombination is a mixture between Auger and radiative recombination.

Optical properties of InAsSb based quantum structure have been investigated both theoretically and experimentally demonstrating a significant step toward realizing novel optoelectronic devices. Type-I MQWs structure shows great potential for the development of mid-infrared LEDs operating at 3.3 μm. In particular, Si-based LEDs report bright room temperature electroluminescence spectra, narrow linewidth (x 1.2), better temperature stability (x1.1) and enhancements in the device efficiency (x1.3) when compared to GaAs-based LEDs. Despite the great energy confinement and strong electron/hole wavefunction overlap, the major limitation of a type-I material system is the strong non-radiative recombination presented on these quantum structures as discussed in the literature review chapter (Ch.3). Therefore Type-II SLS design benefits of quantum confinement and spatial localization of the carriers to suppress Auger,

resulting in enhanced luminescence properties, achieving technologically essential room temperature operation in the long wavelength range. Utilizing type-II SLS report the successful reduction in the quenching of integrated intensity with increasing temperature by a factor of 3 and higher output power when compared to Type-I MQWs. The development of novel quantum structures will enable utilizing next-generation, cost-effective nanophotonic structures for the technologically important mid-infrared spectra range.

7.2 Suggestions for future work

The novel InAsSb-based quantum structures operated in the mid-infrared spectra range have been developed and investigated in this thesis achieving some of the main challenges such as control emission wavelength and reduction in the Auger rate; however, some points should be addressed to improve the efficiency of the MQWs and SLS LED structures:

- To improve the material quality of Si-based MQWs LED, dislocation filters containing GaSb/AlSb SLS should relieve some of the strain associated with the difference in the lattice content between GaSb and Si. This has been demonstrated by other researchers, achieving an approximately 33 times reduction in dislocation density.
- The SLS LEDs suffer from hh_1 states becoming populated, which contributes to changing emission wavelength; one solution for this issue is to increase the energy separation between hh1 and hh2 states by adopting a thinner periods structure. Alternatively, increasing antimony contents in the InAsSb layer to get the right emission wavelength with hh2 transition.

- The large linewidth observed in the EL spectra of SLS LEDs can be efficiently reduced by employing the resonant cavity structures RCLEDs. By doing so, the optical properties would be significantly improved. Temperature dependence of emission peak will also be reduced quite substantially by a factor of 7, linewidth will reduce by a factor of 16, and peak power significantly enhanced, but as much as x 13 from previous RCLED work at Lancaster University.

Further investigation to improve the material quality (i.e. reduce the defect density) could be realised by refining the growth technique benefiting all structures considered in this work. MBE growth was not directly undertaken during this project. Although growth was carried out by experienced colleagues, iteration and development of growth to optimise the LED structures was minimal, so there is likely good potential for improvement. Development should concentrate on reduction of unwanted recombination, such as SRH recombination. Another area which was not specifically refined during this project was device fabrication. Improvement in the electrical properties (i.e. series resistance, turn-on voltage, etc) are to be expected if the fabrication process is optimised, especially contact metallisation and etching chemistry.

Appendix A

A.1 Simulation of the $InAs_{1-x}Sb_x/Al_yIn_{1-y}As$ MQWs structure

```
#Begin Nextnano simulation of InAsSb/AlInAs MQW
#---------------------------------------------------------------------
#begin simulation parameter section


$TEMP = 4                       # Temperature (K)
$ALLOY1 = 0.875                  #As   content in well
$ALLOY2 = 0.122                  #Al   content in barrier
$ALLOY3 = 0.24                   #Al   content in EBL
$ALLOY4 = 0.122                  #Al  in wafer/buffer
$KP8 = 0                              # use either 8-band k.p model for
electrons and holes (1) or single-band effective mass model (0)
$STRAIN = 1                     # include (1) or ignore (0) strain
$QW1a_min=100     #QW thickness  10nm Qwell thickness
$QW1a_max=110
$QW1b_min=110     #QW barrier    17nm Qbarrier thickness
$QW1b_max=127
$QW2a_min=127
$QW2a_max=137
$QW2b_min=137
$QW2b_max=154
$QW3a_min=154
$QW3a_max=164
$QW3b_min=164
$QW3b_max=181
$QW4a_min=181
$QW4a_max=191
$QW4b_min=191
$QW4b_max=208
$QW5a_min=208
$QW5a_max=218
$QW5b_min=218
$QW5b_max=235
$QWbarrier_min=235
$QWbarrier_max=265

$SINGLE = 1-$KP8

#---------------------------------------------------------------------

global{
   simulate1D{}

   temperature = $TEMP

   substrate{ name = "GaAs" }                          # unstrained
material
```

```
   crystal_zb{  x_hkl  =  [1,  0,  0]  y_hkl  =  [0,  1,  0]  }  #  defines
orientation of simulation domain (x = growth direction)
}<>

 #being bowing of InAs(x)Sb(1-x)

database{
     ternary_zb{
                  name = "InAs(x)Sb(1-x)"
                  conduction_bands{
                  Gamma {bandgap  = 0.69 }}   #CB bowing vlaue

                     valence_bands{
                                  bandoffset  =  -0.85    #VB  bowing
vlaue
                                     delta_SO = 0} }}<>

#-------------------------------------------------------------------------
#set geomatry of InAsSb/InAnAs MQW

grid{
   xgrid{
      line{ pos = 0           spacing = 0.25 }
      line{ pos = $QW1a_min    spacing = 0.25 }
      line{ pos = $QW1a_max    spacing = 0.25 }
      line{ pos = $QW1b_min    spacing = 0.25 }
      line{ pos = $QW1b_max    spacing = 0.25 }
      line{ pos = $QW2a_min    spacing = 0.25 }
      line{ pos = $QW2a_max    spacing = 0.25 }
      line{ pos = $QW2b_min    spacing = 0.25 }
      line{ pos = $QW2b_max    spacing = 0.25 }
      line{ pos = $QW3a_min    spacing = 0.25 }
      line{ pos = $QW3a_max    spacing = 0.25 }
      line{ pos = $QW3b_min    spacing = 0.25 }
      line{ pos = $QW3b_max    spacing = 0.25 }

      line{ pos = $QW4a_min    spacing = 0.25 }
      line{ pos = $QW4a_max    spacing = 0.25 }
      line{ pos = $QW4b_min    spacing = 0.25 }
      line{ pos = $QW4b_max    spacing = 0.25 }

      line{ pos = $QW5a_min    spacing = 0.25 }
      line{ pos = $QW5a_max    spacing = 0.25 }
      line{ pos = $QW5b_min    spacing = 0.25 }
      line{ pos = $QW5b_max    spacing = 0.25 }

      line{ pos = $QWbarrier_min    spacing = 0.25 }
      line{ pos = $QWbarrier_max    spacing = 0.25 }
      line{ pos = 365 spacing = 0.25 }

   }

}<>


structure{
   output_region_index{boxes=no}
   output_material_index{boxes=no}
   output_alloy_composition{boxes=no}
```

```
   region{
      everywhere{}
     contact{ name = dummy}
     ternary_constant{ name = "Al(x)In(1-x)As" alloy_x = $ALLOY4 }


   }

     region{
      line{ x = [0 ,365]}
      ternary_constant{
             name = "Al(x)In(1-x)As" alloy_x = $ALLOY4
    }
}

region{
      line{ x = [$QW1a_min ,$QW1a_max] }
      ternary_constant{ name = "InAs(x)Sb(1-x)" alloy_x = $ALLOY1 }
   }

region{
      line{ x = [$QW1b_min ,$QW1b_max] }

      ternary_constant{ name = "Al(x)In(1-x)As" alloy_x = $ALLOY2 }
   }
region{
      line{ x = [$QW2a_min ,$QW2a_max] }
      ternary_constant{ name = "InAs(x)Sb(1-x)" alloy_x = $ALLOY1 }
   }
region{
      line{ x = [$QW2b_min ,$QW2b_max] }
      ternary_constant{ name ="Al(x)In(1-x)As" alloy_x = $ALLOY2 }
   }
region{
      line{ x = [$QW3a_min ,$QW3a_max] }
      ternary_constant{ name = "InAs(x)Sb(1-x)" alloy_x = $ALLOY1 }
   }
region{
      line{ x = [$QW3b_min ,$QW3b_max] }
      ternary_constant{ name = "Al(x)In(1-x)As" alloy_x = $ALLOY2 }
   }

region{
      line{ x = [$QW4a_min ,$QW4a_max] }
      ternary_constant{ name = "InAs(x)Sb(1-x)" alloy_x = $ALLOY1 }
   }
region{
      line{ x = [$QW4b_min ,$QW4b_max] }
      ternary_constant{ name = "Al(x)In(1-x)As" alloy_x = $ALLOY2 }
   }
region{
      line{ x = [$QW5a_min ,$QW5a_max] }
      ternary_constant{ name = "InAs(x)Sb(1-x)" alloy_x = $ALLOY1 }
   }
region{
      line{ x = [$QW5b_min ,$QW5b_max] }
      ternary_constant{ name = "Al(x)In(1-x)As" alloy_x = $ALLOY2 }
   }

region{
```

```
      line{ x = [$QWbarrier_min ,$QWbarrier_max] }
      ternary_constant{ name = "Al(x)In(1-x)As" alloy_x = $ALLOY3 }
   }
}<>

#-----------------------------------------------------------------------
contacts{
   fermi{ name = "dummy" bias = 0}
  }<>

classical{
   Gamma{}
   HH{}
   LH{}
   SO{}

   output_bandedges{ averaged = no }
}<>


quantum {
   region{
      name = "quantum_region"
      x = [0, 365]
      no_density = yes
      boundary{ x = dirichlet }

     Gamma{
        num_ev = 100
        }
      HH{
      num_ev = 100
       }
      LH{
num_ev = 100
}
     output_wavefunctions{  amplitudes = yes
                              probabilities = yes
                                          max_num = 10
                                                  all_k_points = no }
   }
}<>


strain{                                 #Include strain
   pseudomorphic_strain{}
   output_strain_tensor{}
}<>


run{
            solve_strain{}
            solve_quantum{}
}<>
#-----------------------------------------------------------------------
#End of Nextnano simulation of InAsSb/AlInAs MQW
```

Figure A.1: Nextnano code used to simulate InAsSb/AlInAs MQW structure.

References:

[1] Popa, Daniel, and Florin Udrea. "Towards integrated mid-infrared gas sensors." *Sensors* 19, no. 9 (2019): 2076.

[2] Gordon, Iouli E., Laurence S. Rothman, Christian Hill, Roman V. Kochanov, Y. Tan, Peter F. Bernath, Manfred Birk et al. "The HITRAN2016 molecular spectroscopic database." *Journal of Quantitative Spectroscopy and Radiative Transfer* 203 (2017): 3-69.

[3] Parry M K and Krier A 1994 Efficient 3.3 mu m light emitting diodes for detecting methane gas at room temperature *Electron. Lett.* **30** 1968–9

[4] Popov A A, Sherstnev V V, Yakovlev Y P, Baranov A N and Alibert C 1997 Powerful mid-infrared light emitting diodes for pollution monitoring *Electron. Lett.* **33** 86–8

[5] Krier A and Sherstnev V V 2000 Powerful interface light emitting diodes for methane gas detection *J. Phys. Appl. Phys.* **33** 101–6

[6] Koerperick E J, Olesberg J T, Boggess T F, Hicks J L, Wassink L S, Murray L M and Prineas J P 2008 InAs⁄GaSb cascaded active region superlattice light emitting diodes for operation at 3.8μm *Appl. Phys. Lett.* **92** 121106

[7] Grasse C, Wiecha P, Gruendl T, Sprengel S, Meyer R and Amann M-C 2012 InP-based 2.8–3.5 μm resonant-cavity light emitting diodes based on type-II transitions in GaInAs/GaAsSb heterostructures *Appl Phys Lett* 5

[8] Underwood K J, Briggs A F, Sifferman S D, Verma V B, Sirica N S, Prasankumar R P, Nam S W, Silverman K L, Bank S R and Gopinath J T 2020 Strain dependence of Auger recombination in 3 μ m GaInAsSb/GaSb type-I active regions *Appl. Phys. Lett.* **116** 262103

[9] Roithner Laser Technik LED34

[10] Gibson D and MacGregor C 2013 A Novel Solid State Non-Dispersive Infrared CO2 Gas Sensor Compatible with Wireless and Portable Deployment *Sensors* **13** 7079–103

[11] Ocko I B, Sun T, Shindell D, Oppenheimer M, Hristov A N, Pacala S W, Mauzerall D L, Xu Y and Hamburg S P 2021 Acting rapidly to deploy readily available methane mitigation measures by sector can immediately slow global warming *Environ. Res. Lett.* **16** 054042

[12] d, n., 2022. *Importance of Methane | US EPA*. [online] US EPA. Available at: <https://www.epa.gov/gmi/importance-methane> [Accessed 20 April 2022].

[13] Liang R, Kipshidze G, Hosoda T, Shterengas L and Belenky G 2014 3.3–3.4-μm Diode Lasers Based on Triple-Layer GaInAsSb Quantum Wells *IEEE Photonics Technol. Lett.* **26** 664–6

[14] Bagyanarayana D G CHENNAI, 2011 BImpact of anthrapogenic activities on Biodiversity and Climate Change, 98th Indian Science Congress PART II 465

[15] Zhao Y, Xin H, Shepherd T, Hayes M, Stinn J and Li H 2013 Thermal environment, ammonia concentrations, and ammonia emissions of aviary houses with white laying hens *Trans. ASABE* **56** 1145–56

[16] d, n., 2022. *Air Pollution Information System | Air Pollution Information System*. [online] Apis.ac.uk. Available at: <http://www.apis.ac.uk> [Accessed 18 April 2022].

[17] Sutton M A, Dragosits U, Tang Y S and Fowler D 2000 Ammonia emissions from non-agricultural sources in the UK *Atmos. Environ.* **34** 855–69

[18] Jung S, Suchalkin S, Kipshidze G, Westerfeld D, Golden E, Snyder D and Belenky G 2010 Dual wavelength GaSb based type I quantum well mid-infrared light emitting diodes *Appl. Phys. Lett.* **96** 191102

[19] Rejeb S B, Debbichi M, Said M, Gassenq A, Tournié E and Christol P 2010 Modelling of an InAs/GaSb/InSb short-period superlattice laser diode for mid-infrared emission by the k.p method *J. Phys. Appl. Phys.* **43** 325102

[20] Keen J A, Lane D, Kesaria M, Marshall A R J and Krier A 2018 InAs/InAsSb type-II strained-layer superlattices for mid-infrared LEDs *J. Phys. Appl. Phys.* **51** 075103

[21] Kurka M, Dyksik M, Suomalainen S, Koivusalo E, Guina M and Motyka M 2019 GaInAsSb/AlGa(In)AsSb type I quantum wells emitting in 3 μm range for application in superluminescent diodes *Opt. Mater.* **91** 274–8

[22] Carrington P J, Solov'ev V A, Zhuang Q, Krier A and Ivanov S V 2008 Room temperature midinfrared electroluminescence from InSb/InAs quantum dot light emitting diodes *Appl. Phys. Lett.* **93** 091101

[23] Muhowski A J, Muellerleile A M, Olesberg J T and Prineas J P 2020 Internal quantum efficiency in 6.1 Å superlattices of 77% for mid-wave infrared emitters *Appl. Phys. Lett.* **117** 061101

[24] Abell J, Kim C S, Bewley W, Merritt C D, Canedy C L, Vurgaftman I, Meyer J R and Kim M 2014 Mid-infrared interband cascade light emitting devices with milliwatt output powers at room temperature *Appl. Phys. Lett.* **104** 261103

[25] Meyer J R, Bewley W, Canedy C L, Kim C S, Kim M, Merritt C D and Vurgaftman I 2020 The Interband Cascade Laser *Photonics* **7** 75

[26] Delli E, Hodgson P D, Bentley M, Repiso E, Craig A P, Lu Q, Beanland R, Marshall A R J, Krier A and Carrington P J 2020 Mid-infrared type-II InAs/InAsSb quantum wells integrated on silicon *Appl. Phys. Lett.* **117** 131103

[27] Repiso E, Broderick C A, de la Mata M, Arkani R, Lu Q, Marshall A R J, Molina S I, O'Reilly E P, Carrington P J and Krier A 2019 Optical properties of

metamorphic type-I InAs $_{1-x}$ Sb $_{x}$ /Al $_{y}$ In $_{1-y}$ As quantum wells grown on GaAs for the mid-infrared spectral range *J. Phys. Appl. Phys.* **52** 465102

[28] Krier A, Stone M and Krier S E 2007 Characterization of InAs $_{0.91}$ Sb $_{0.09}$ for use in mid-infrared light-emitting diodes grown by liquid phase epitaxy from Sb-rich solution *Semicond. Sci. Technol.* **22** 624–8

[29] Aytac Y, Olson B V, Kim J K, Shaner E A, Hawkins S D, Klem J F, Flatté M E and Boggess T F 2014 Effects of layer thickness and alloy composition on carrier lifetimes in mid-wave infrared InAs/InAsSb superlattices *Appl. Phys. Lett.* **105** 022107

[30] Biefeld, R. M., A. A. Allerman, and S. R. Kurtz. "Recent advances in mid-infrared (3–6 μm) emitters." *Materials Science and Engineering: B* 51, no. 1-3 (1998): 1-8.

[31] Ting D Z, Rafol S B, Khoshakhlagh A, Soibel A, Keo S A, Fisher A M, Pepper B J, Hill C J and Gunapala S D 2020 InAs/InAsSb Type-II Strained-Layer Superlattice Infrared Photodetectors *Micromachines* **11** 958

[32] Steenbergen, Elizabeth H., Kalyan Nunna, Lu Ouyang, Bruno Ullrich, Diana L. Huffaker, David J. Smith, and Yong-Hang Zhang. "Strain-balanced InAs/InAs1−xSbx type-II superlattices grown by molecular beam epitaxy on GaSb substrates." *Journal of Vacuum Science & Technology B, Nanotechnology and Microelectronics: Materials, Processing, Measurement, and Phenomena* 30, no. 2 (2012): 02B107.

[33] Steenbergen, E. H., Connelly, B. C., Metcalfe, G. D., Shen, H., Wraback, M., Lubyshev, D., ... & Zhang, Y. H. (2011). Significantly improved minority carrier lifetime observed in a long-wavelength infrared III-V type-II superlattice comprised of InAs/InAsSb. *Applied Physics Letters*, *99*(25), 251110.

[34] Steenbergen E H, Nunna K, Ouyang L, Ullrich B, Huffaker D L, Smith D J and Zhang Y-H 2012 Strain-balanced InAs/InAs $_{1-x}$ Sb $_{x}$ type-II superlattices grown by molecular beam epitaxy on GaSb substrates *J. Vac. Sci. Technol. B Nanotechnol. Microelectron. Mater. Process. Meas. Phenom.* **30** 02B107

[35] Steenbergen E H, Massengale J A, Ariyawansa G and Zhang Y-H 2016 Evidence of carrier localization in photoluminescence spectroscopy studies of mid-wavelength infrared InAs/InAs1−Sb type-II superlattices *J. Lumin.* **178** 451–6

[36] Capasso, Federico. "High-performance midinfrared quantum cascade lasers." *Optical Engineering* 49, no. 11 (2010): 111102.

[37] Mynbaev K D, Bazhenov N L, Semakova A, Chernyaev A V, Kizhaev S, Stoyanov N D, Bougrov V E, Lipsanen H and Salikhov Kh M 2017 Spontaneous and stimulated emission in InAsSb-based LED heterostructures *Infrared Phys. Technol.* **85** 246–50

[38] Dobbelaere, W and De Boeck, J and Bruynserede, C and Mertens, R and Borghs and Gustaaf}, 1993 InAsSb light emitting diodes and their applications to infra-red gas sensors *Electron. Lett.* **29** 890–1

[39] Tang P, Pullin M J, Chung S J, Phillips C, Stradling R A, Norman A G, Li Y B and Hart L 1995 4-11 mu m infrared emission and 300 K light emitting diodes from arsenic-rich InAs $_{1-x}$ Sb $_{x}$ strained layer superlattices *Semicond. Sci. Technol.* **10** 1177–80

[40] Krier, Anthony, ed. *Mid-infrared semiconductor optoelectronics*. Vol. 118. Springer, 2007.

[41] Smith S D, Hardaway H R and Crowder J G 2002 Recent developments in the applications of mid-infrared lasers, LEDs, and other solid state sources to gas detection *Novel In-Plane Semiconductor Lasers* Novel In-Plane Semiconductor Lasers vol 4651 (SPIE) pp 157–72

[42] Vurgaftman I, Meyer J R and Ram-Mohan L R 2001 Band parameters for III–V compound semiconductors and their alloys *J. Appl. Phys.* **89** 5815–75

[43] Sze S M, Li Y and Ng K 2021 *Physics of Semiconductor Devices* (John Wiley & Sons)

[44] Selcuk E 2009 *Guided and deterministic self organization of quantum dots* (Technische Universiteit Eindhoven)

[45] Krijn M P C M 1991 Heterojunction band offsets and effective masses in III-V quaternary alloys *Semicond. Sci. Technol.* **6** 27–31

[46] Kuo C P, Vong S K, Cohen R M and Stringfellow G B 1985 Effect of mismatch strain on band gap in III-V semiconductors *J. Appl. Phys.* **57** 5428–32

[47] Van de Walle C G 1989 Band lineups and deformation potentials in the model-solid theory *Phys. Rev. B* **39** 1871–83

[48] O'Reilly E P 1989 Valence band engineering in strained-layer structures *Semicond. Sci. Technol.* **4** 121–37

[49] Jain S, Willander M and Van Overstraeten R 2000 Band structure and optical properties *Compound Semiconductors Strained Layers and Devices* Electronic Materials Series ed S Jain, M Willander and R Van Overstraeten (Boston, MA: Springer US) pp 115–57

[50] Yu P Y and Cardona M 2005 *Fundamentals of semiconductors: physics and materials properties ; with 52 tables and 116 problems* (Berlin Heidelberg: Springer)

[51] Petroff P M, Logan R A and Savage A 1980 Nonradiative Recombination at Dislocations in III-V Compound Semiconductors *Phys. Rev. Lett.* **44** 287–91

[52] Passchier C W and Trouw R A J 2005 *Microtectonics* (Springer Science & Business Media)

[53] J.H D 1998 *The physics of low-dimensional semiconductors : an introduction.* (Cambridge University Press,)

[54] Matthews J W and Blakeslee A E 1974 Defects in epitaxial multilayers: I. Misfit dislocations *J. Cryst. Growth* **27** 118–25

[55] People R and Bean J C 1985 Calculation of critical layer thickness versus lattice mismatch for $Ge_x Si_{1-x}$/Si strained-layer heterostructures *Appl. Phys. Lett.* **47** 322–4

[56] Edvinsson T 2018 Optical quantum confinement and photocatalytic properties in two-, one- and zero-dimensional nanostructures *R. Soc. Open Sci.* **5** 180387

[57] Schubert, E. Fred. *Light-emitting diodes*. E. Fred Schubert, 2018.

[58] Kressel H and Butler J K 1979 Chapter 2 Heterojunction Laser Diodes *Semiconductors and Semimetals* Lasers, Junctions, Transport vol 14, ed R K Willardson and A C Beer (Elsevier) pp 65–194

[59] Rogalski, A., and Z. Orman. "Band-to-band recombination in InAs1−xSbx." *Infrared physics* 25, no. 3 (1985): 551-560

[60] Smith C, Abram R A and Burt M G 1983 Auger recombination in a quantum well heterostructure *J. Phys. C Solid State Phys.* **16** L171–5

[61] Peter Carrington 2009 *Quantum Nanostructures grown by Molecular Beam Epitaxy for Mid-Infrared Applications*

[62] Gao, H. H., A. Krier, and V. V. Sherstnev. "Room-temperature InAs 0.89 Sb 0.11 photodetectors for CO detection at 4.6 μm." *Applied Physics Letters* 77, no. 6 (2000): 872-874. [57] Schubert E F 2018 *Light-Emitting Diodes (3rd Edition)* (E. Fred Schubert)

[63] Schubert E F 2018 *Light-Emitting Diodes (3rd Edition)* (E. Fred Schubert)

[64] Melngailis I and Rediker R H 1966 Properties of InAs Lasers *J. Appl. Phys.* **37** 899–911

[65] Ashley T, Elliott C T, Gordon N T, Hall R S, Johnson A D and Pryce G J 1994 Uncooled InSb/$In_{1-x} Al_x$ Sb mid-infrared emitter *Appl. Phys. Lett.* **64** 2433–5

[66] Krier, A., H. H. Gao, V. V. Sherstnev, and Yu Yakovlev. "High power 4.6 μm light emitting diodes for CO detection." *Journal of Physics D: Applied Physics* 32, no. 24 (1999): 3117

[67] Harvey R. Hardaway, Tim Ashley, Louise Buckle, Martin T. Emeny, Graeme Masterton, and Graham Pryce 2004 Optimizing indium aluminum antimonide LEDs and photodiodes for gas sensing applications Proc.SPIE vol 5564

[68] Haigh M K, Nash G R, Smith S J, Buckle L, Emeny M T and Ashley T 2007 Mid-infrared AlxIn1−xSb light-emitting diodes *Appl. Phys. Lett.* **90** 231116

[69] Mirza B I, Nash G R, Smith S J, Buckle L, Coomber S D, Emeny M T and Ashley T 2008 Recombination processes in midinfrared AlxIn1−xSb light-emitting diodes *J. Appl. Phys.* **104** 063113

[70] Nash G R, Forman H L, Smith S J, Robinson P B, Buckle L, Coomber S D, Emeny M T, Gordon N T and Ashley T 2009 Mid-Infrared ${\rm Al}_{x}{\rm In}_{1-x}{\rm Sb}$ Light-Emitting Diodes and Photodiodes for Hydrocarbon Sensing *IEEE Sens. J.* **9** 1240–3

[71] Nash G R, Haigh M K, Hardaway H R, Buckle L, Andreev A D, Gordon N T, Smith S J, Emeny M T and Ashley T 2006 InSb⁄AlInSb quantum-well light-emitting diodes *Appl. Phys. Lett.* **88** 051107

[72] Meriggi L, Steer M J, Ding Y, Thayne I G, MacGregor C, Ironside C N and Sorel M 2015 Enhanced emission from mid-infrared AlInSb light-emitting diodes with p-type contact grid geometry *J. Appl. Phys.* **117** 063101

[73] Fujita H, Ueno K, Morohara O, Camargo E, Geka H, Shibata Y and Kuze N 2018 AlInSb Mid-Infrared LEDs of High Luminous Efficiency for Gas Sensors *Phys. Status Solidi A* **215** 1700449

[74] Delli E, Hodgson P D, Repiso E, Craig A P, Hayton J P, Lu Q, Marshall A R J, Krier A and Carrington P J 2019 Heteroepitaxial Integration of Mid-Infrared InAsSb Light Emitting Diodes on Silicon *IEEE Photonics J.* **11** 1–8

[75] Tang P J P, Hardaway H, Heber J, Phillips C, Pullin M J, Stradling R A, Yuen W T and Hart L 1998 Efficient 300 K light-emitting diodes at λ∼5 and ∼8 μm from InAs/In(As1−xSbx) single quantum wells *Appl. Phys. Lett.* **72** 3473–5

[76] Heber J D, Gevaux D, Li X and Phillips C 2000 Room temperature InAs/InAs1−xSbxsingle quantum well light emitting diodes with barriers for improved carrier confinement *IEE Proc. - Optoelectron.* **147** 407–11

[77] Choi H K and Eglash S J 1992 High-power multiple-quantum-well GaInAsSb/AlGaAsSb diode lasers emitting at 2.1 μm with low threshold current density *Appl. Phys. Lett.* **61** 1154–6

[78] Garbuzov D Z, Martinelli R U, Lee H, York P K, Menna R J, Connolly J C and Narayan S Y 1996 Ultralow-loss broadened-waveguide high-power 2 μm AlGaAsSb/InGaAsSb/GaSb separate-confinement quantum-well lasers *Appl. Phys. Lett.* **69** 2006–8

[79] Shterengas L, Belenky G L, Kim J G and Martinelli R U 2004 Design of high-power room-temperature continuous-wave GaSb-based type-I quantum-well lasers with > 2.5 μm *Semicond. Sci. Technol.* **19** 655–8

[80] Shterengas L, Belenky G, Kipshidze G and Hosoda T Room temperature operated 3.1 μm type-I GaSb-based diode lasers with 80 mW continuous-wave output power *Appl Phys Lett* 4

[81] Turner G W, Choi H K and Manfra M J 1998 Ultralow-threshold (50 A/cm2) strained single-quantum-well GaInAsSb/AlGaAsSb lasers emitting at 2.05 μm *Appl. Phys. Lett.* **72** 876–8

[82] Jung S, Suchalkin S, Kipshidze G, Westerfeld D, Snyder D, Johnson M and Belenky G 2009 GaSb-Based Type I Quantum-Well Light-Emitting Diode Addressable Array Operated at Wavelengths Up to 3.66 μm *IEEE Photonics Technol. Lett.* **21** 1087–9

[83] Jung S, Suchalkin S, Westerfeld D, Kipshidze G, Golden E, Snyder D and Belenky G 2011 High dimensional addressable LED arrays based on type I GaInAsSb quantum wells with quinternary AlGaInAsSb barriers *Semicond. Sci. Technol.* **26** 085022

[84] Borghs G, Németh Š, Grietens B, Van Daele P and Van Hoof C 1997 Growth and characterisation of mid-IR InAs0.9Sb0.1/InAs strained multiple quantum well light emitting diodes grown on InAs substrates *IEE Proc. - Optoelectron.* **144** 295–8

[85] Carrington P J, de la Mare M, Cheetham K J, Zhuang Q and Krier A 2011 Midinfrared InAsSbN/InAs Multiquantum Well Light-Emitting Diodes *Adv. Optoelectron.* **2011** 1–8

[86] Aziz M, Xie C, Pusino V, Khalid A, Steer M, Thayne I G and Cumming D R S 2017 Multispectral mid-infrared light emitting diodes on a GaAs substrate *Appl. Phys. Lett.* **111** 102102

[87] Gu Y, Zhang Y G, Chen X Y, Cao Y, Fang X, Ding G Q and Zhou L 2013 InAs/In $_{0.83}$ Al $_{0.17}$ As quantum wells on GaAs substrate with type-I emission at 2.9 μ m *Appl. Phys. Lett.* **102** 121110

[88] Chertouk, M., H. Heiss, D. Xu, S. Kraus, W. Klein, G. Bohm, G. Trankle, and G. Weimann. "Metamorphic InAlAs/InGaAs HEMTs on GaAs substrates with a novel composite channels design." *IEEE Electron Device Letters* 17, no. 6 (1996): 273-275.

[89] Cao Y, Zhang Y G, Gu Y, Chen X Y, Zhou L and Li H 2013 2.7 μ m InAs quantum well lasers on InP-based InAlAs metamorphic buffer layers *Appl. Phys. Lett.* **102** 201111

[90] Zegrya G and Andreev A D 1995 Mechanism of suppression of Auger recombination processes in type-II heterostructures *Appl. Phys. Lett.* **67** 2681–3

[91] Zegrya G 1999 Suppression of Auger recombination in diode lasers utilizing InAsSb/InAsSbP and InAs/GaInAsSb type-II heterojunctions *Semiconductors* **33** 350

[92] Pullin M J, Hardaway H R, Heber J D, Phillips C, Yuen W T, Stradling R A and Moeck P 1999 Room-temperature InAsSb strained-layer superlattice light-emitting diodes at λ=4.2 μm with AlSb barriers for improved carrier confinement *Appl. Phys. Lett.* **74** 2384–6

[93] Krier A, Stone M, Zhuang Q D, Liu P-W, Tsai G and Lin H 2006 Mid-infrared electroluminescence at room temperature from InAsSb multi-quantum-well light-emitting diodes *Appl. Phys. Lett.* **89** 091110

[94] Carrington P J, Zhuang Q, Yin M and Krier A 2009 Temperature dependence of mid-infrared electroluminescence in type II InAsSb/InAs multi-quantum well light-emitting diodes *Semicond. Sci. Technol.* **24** 075001

[95] Olson B V, Shaner E A, Kim J K, Klem J F, Hawkins S D, Murray L M, Prineas J P, Flatté M E and Boggess T F 2012 Time-resolved optical measurements of minority carrier recombination in a mid-wave infrared InAsSb alloy and InAs/InAsSb superlattice *Appl. Phys. Lett.* **101** 092109

[96] Steenbergen E H, Connelly B C, Metcalfe G D, Shen H, Wraback M, Lubyshev D, Qiu Y, Fastenau J M, Liu A W K, Elhamri S, Cellek O and Zhang Y-H 2011 Significantly improved minority carrier lifetime observed in a long-wavelength infrared III-V type-II superlattice comprised of InAs/InAsSb *Appl. Phys. Lett.* **99** 251110

[97] Li S 1995 *Proceedings of the Third International Symposium on Long Wavelength Infrared Detectors and Arrays: Physics and Applications III* (The Electrochemical Society)

[98] Keen J A, Repiso E, Lu Q, Kesaria M, Marshall A R J and Krier A 2018 Electroluminescence and photoluminescence of type-II InAs/InAsSb strained-layer superlattices in the mid-infrared *Infrared Phys. Technol.* **93** 375–80

[99] Yang R Q, Lin C-H, Murry S J, Pei S, Liu H C, Buchanan M and Dupont E 1997 Interband cascade light emitting diodes in the 5–8 μm spectrum region *Appl. Phys. Lett.* **70** 2013–5

[100] Das N C, Olver K, Towner F, Simonis G and Shen H 2005 Infrared (3.8μm) interband cascade light-emitting diode array with record high efficiency *Appl. Phys. Lett.* **87** 041105

[101] Provence S R, Ricker R, Aytac Y, Boggess T F and Prineas J P 2015 High power cascaded mid-infrared InAs/GaSb light emitting diodes on mismatched GaAs *J. Appl. Phys.* **118** 123108

[102] Ricker R J, Provence S R, Norton D T, Boggess T F and Prineas J P 2017 Broadband mid-infrared superlattice light-emitting diodes *J. Appl. Phys.* **121** 185701

[103] Muhowski A J, Ricker R J, Boggess T F and Prineas J P 2017 n-type anode layer, high-power MWIR superlattice LED *Appl. Phys. Lett.* **111** 243509

[104] Ermolaev M, Lin Y, Shterengas L, Hosoda T, Kipshidze G, Suchalkin S and Belenky G 2018 GaSb-Based Type-I Quantum Well 3–3.5- μ m Cascade Light Emitting Diodes *IEEE Photonics Technol. Lett.* **30** 869–72

[105] Kim C S, Bewley W, Merritt C D, Canedy C L, Warren M V, Vurgaftman I, Meyer J R and Kim M 2017 Improved mid-infrared interband cascade light-emitting devices *Opt. Eng.* **57** 1

[106] Muhowski A J, Bogh C L, Heise R L, Boggess T F and Prineas J P 2019 Improved performance of mid-infrared superlattice light emitting diodes grown epitaxially on silicon *J. Cryst. Growth* **507** 46–9

[107] Hadji, E., J. Bleuse, N. Magnea, and J. L. Pautrat. "3.2 μm infrared resonant cavity light emitting diode." *Applied Physics Letters* 67, no. 18 (1995): 2591-2593.

[108] Green, Alex M., David G. Gevaux, Christine Roberts, and Chris C. Phillips. "Resonant-cavity-enhanced photodetectors and LEDs in the mid-infrared." *Physica E: Low-dimensional Systems and Nanostructures* 20, no. 3-4 (2004): 531-535.

[109] Al-Saymari F A M and Krier A Design, Growth and Characterisation of Resonant Cavity Light Emitting Diodes (RCLEDs) for Mid-infrared Applications 181

[110] Ducanchez A, Cerutti L, Gassenq A, Grech P and Genty F 2008 Fabrication and Characterization of GaSb-Based Monolithic Resonant-Cavity Light-Emitting Diodes Emitting Around 2.3 μm and Including a Tunnel Junction *IEEE J. Sel. Top. QUANTUM Electron.* **14** 8

[111] Al-Saymari F A, Craig A P, Lu Q, Marshall A R J, Carrington P J and Krier A 2020 Mid-infrared resonant cavity light emitting diodes operating at 45 μm *Opt. Express* **28** 23338

[112] Hayton J P Development of Mid-Infrared Light Emitting Diodes to Replace Incandescent Airfield Lighting 196

[113] Birner S, Zibold T, Andlauer T, Kubis T, Sabathil M, Trellakis A and Vogl P 2007 nextnano: General Purpose 3-D Simulations *IEEE Trans. Electron Devices* **54** 2137–42

[114] Cripps S A, Hosea T J C, Krier A, Smirnov V, Batty P J, Zhuang Q D, Lin H, Liu P-W and Tsai G 2007 Midinfrared photoreflectance study of InAs-rich InAsSb and GaInAsPSb indicating negligible bowing for the spin orbit splitting energy *Appl. Phys. Lett.* **90** 172106

[115] Liu P-W, Tsai G, Lin H, Krier A, Zhuang Q D and Stone M Photoluminescence and bowing parameters of InAsSb⁄InAs multiple quantum wells grown by molecular beam epitaxy *Appl Phys Lett* 4

[116] Sugo M, Uchida N, Yamamoto A, Nishioka T and Yamaguchi M 1989 Residual strains in heteroepitaxial III-V semiconductor films on Si(100) substrates *J. Appl. Phys.* **65** 591–5

[117] Buyanova I A, Chen W M, Pozina G, Bergman J P, Monemar B, Xin H P and Tu C W 1999 Mechanism for low-temperature photoluminescence in GaNAs/GaAs structures grown by molecular-beam epitaxy *Appl. Phys. Lett.* **75** 501–3

[118] Abramkin D S, Gutakovskii A K and Shamirzaev T S 2018 Heterostructures with diffused interfaces: Luminescent technique for ascertainment of band alignment type *J. Appl. Phys.* **123** 115701

[119] Yoon I T, Ji T S, Oh S J, Choi J C and Park H L 1997 Concentration dependent photoluminescence of Te-doped In0.5Ga0.5P layers grown by liquid phase epitaxy *J. Appl. Phys.* **82** 4024–7

[120] Oueslati M, Zouaghi M, Pistol M E, Samuelson L, Grimmeiss H G and Balkanski M 1985 Photoluminescence study of localization effects induced by the fluctuating random alloy potential in indirect band-gap GaAs 1 − x P x *Phys. Rev. B* **32** 8220–7

[121] Muhowski A J, Bogh C L, Heise R L, Boggess T F and Prineas J P 2019 Improved performance of mid-infrared superlattice light emitting diodes grown epitaxially on silicon *J. Cryst. Growth* **507** 46–9

[122] Kroemer H 2004 The family (InAs, GaSb, AlSb) and its heterostructures: a selective review *Phys. E Low-Dimens. Syst. Nanostructures* **20** 196–203

[123] Mikhailova M P, Andreev I A, Moiseev K D, Ivanov E V, Stoyanov N D, Yakovlev Yu P, Hulicius E, Hospodková A, Pangrác J, Melichar K and Simecek T 2008 Photovoltaic detector based on type II p-InAs/AlSb/InAsSb/AlSb/p-GaSb heterostructures with a single quantum well for mid-infrared spectral range Photonics, Devices, and Systems IV ed P Tománek, D Senderáková and M Hrabovský (Prague, Czech Republic) p 713813

[124] Moiseev K 2009 TYPE II HETEROSTRUCTURES IN OPTOELECTRONIC DEVICES OPERATING IN MID-INFARED SPECTRAL RANGE 5

[125] Ayers J E, Kujofsa T, Rago P and Raphael J 2016 *Heteroepitaxy of Semiconductors: Theory, Growth, and Characterization, Second Edition* (Boca Raton: CRC Press)

[126] Lackner D, Steger M, Thewalt M L W, Pitts O J, Cherng Y T, Watkins S P, Plis E and Krishna S 2012 InAs/InAsSb strain balanced superlattices for optical detectors: Material properties and energy band simulations *J. Appl. Phys.* **111** 034507

[127] Keen J A Characterisation and simulation of InAs/InAsSb structures for mid – infrared LEDs 149

[128] Steenbergen E H Strain-balanced InAs-InAsSb Type-II Superlattices on GaSb Substrates for Infrared Photodetector Applications 201

[129] Ryan J C and Reinecke T L 1993 Band-gap renormalization of optically excited semiconductor quantum wells *Phys. Rev. B* **47** 9615–20

[130] Lin H-H, Liu P-W and Chen J-R 2003 GaAsSb/GaAs type-II quantum well and its application on /spl sim/1.3 /spl mu/m laser *Proceedings of the Sixth Chinese Optoelectronics Symposium (IEEE Cat. No.03EX701)* Proceedings of the Sixth Chinese Optoelectronics Symposium (IEEE Cat. No.03EX701) pp 112–5

[131] Ledentsov N, Böhrer J, Beer M, Heinrichsdorff F, Grundmann M, Bimberg D, Ivanov S V, Meltser B Ya, Shaposhnikov S V, Yassievich I N, Faleev N, Kop'ev P S and Alferov Zh I 1995 Radiative states in type-II GaSb/GaAs quantum wells *Phys. Rev. B* **52** 14058–66

[132] Bertru N, Baranov A N, Cuminal Y, Boissier G, Alibert C, Joullie A and Lambert B 1999 Spontaneous emission from InAs/GaSb quantum wells grown by molecular beam epitaxy *J. Appl. Phys.* **85** 1989–91

[133] Haugan H J, Szmulowicz F, Brown G J, Ullrich B, Munshi S R, Wickett J C and Stokes D W 2007 Short-period InAs/GaSb superlattices for mid-infrared photodetectors *Phys. Status Solidi C* **4** 1702–6

[134] Kryzhanovskaya N V, Gladyshev A G, Sizov D S, Kovsh A R, Tsatsul'nikov A F, Chi J Y, Wang J S, Wei L and Ustinov V M 2003 The carriers localization influence on the optical properties of GaAsN/ GaAs heterostructures grown by molecular-beam epitaxy Proceedings of SPIE - The International Society for Optical Engineering vol 5023 pp 38–41

[135] Lourenço S A, Dias I F L, Duarte J L, Laureto E, Aquino V M and Harmand J C 2007 Temperature-dependent photoluminescence spectra of GaAsSb/AlGaAs and GaAsSbN/GaAs single quantum wells under different excitation intensities *Braz. J. Phys.* **37** 1212–9

[136] Dumont H, Auvray L, Monteil Y, Saidi F, Hassen F and Maaref H 2003 Radiative N-localized recombination and confinement in GaAsN/GaAs epilayers and quantum well structures *Opt. Mater.* **24** 303–8

[137] Noh Y-K, Seo J-H, Choi H-S, Kim M-D and Oh J-E 2012 Thickness dependence of temperature-induced emission mechanism in InGaN/AlGaN short-period superlattices *J. Appl. Phys.* **112** 043102

[138] Reyner C J, Wang J, Nunna K, Lin A, Liang B, Goorsky M S and Huffaker D L 2011 Characterization of GaSb/GaAs interfacial misfit arrays using x-ray diffraction *Appl. Phys. Lett.* **99** 231906

[139] Carrington, P. J., Zhuang, Q., Yin, M., & Krier, A. (2009). Temperature dependence of mid-infrared electroluminescence in type II InAsSb/InAs multi-quantum well light-emitting diodes. Semiconductor Science and Technology, 24(7), 075001.

[140] Altayar A R, Al-Saymari F A, Repiso E, Hanks L, Craig A P, Bentley M, Delli E, Carrington P J, Krier A and Marshall A R J 2022 Electroluminescence

characterization of mid-infrared InAsSb/AlInAs multi-quantum well light emitting diodes heteroepitaxially integrated on GaAs and silicon wafers *J. Cryst. Growth* **586** 126627

[141] Schubert E F 2006 *Light-Emitting Diodes (Second Edition, 2006)* (E. Fred Schubert)

[142] Schroder D K 2015 *Semiconductor Material and Device Characterization* (John Wiley & Sons)

[143] Baranovski S 2006 *Charge Transport in Disordered Solids with Applications in Electronics* (John Wiley & Sons)

[144] Joullié A and Christol P 2003 GaSb-based mid-infrared 2–5 μm laser diodes *Comptes Rendus Phys.* **4** 621–37

[145] Sweeney S J, Phillips A F, Adams A R, O'Reilly E P and Thijs P J A 1998 The effect of temperature dependent processes on the performance of 1.5-μm compressively strained InGaAs(P) MQW semiconductor diode lasers *IEEE Photonics Technol. Lett.* **10** 1076–8

[146] Lax M 1960 Cascade Capture of Electrons in Solids *Phys. Rev.* **119** 1502–23

[147] Nash G R and Mirza B I 2013 Efficiency droop in InSb/AlInSb quantum-well light-emitting diodes *Appl. Phys. Lett.* **102** 011127